The Dissertation Committee for Donghwan Kim
certifies that this is the approved version of the following dissertation:

Design of an Optical Microelectromechanical-System Microphone with Sub 15-dBA Noise Floor

Committee:

Neal A. Hall, Supervisor

Mark F. Hamilton

Paul S. Ho

Preston S. Wilson

Edward T. Yu

Design of an Optical Microelectromechanical-System Microphone with Sub 15-dBA Noise Floor

by

Donghwan Kim

DISSERTATION
Presented to the Faculty of the Graduate School of
The University of Texas at Austin
in Partial Fulfillment
of the Requirements
for the Degree of

DOCTOR OF PHILOSOPHY

THE UNIVERSITY OF TEXAS AT AUSTIN
May 2018

I dedicate this dissertation to my parents, siblings, and friends who have supported me throughout the duration of this work.

Acknowledgments

First and foremost, I would like to thank my advisor, Neal A. Hall. I feel privileged to have studied under his guidance past six years. Throughout my study, he provided me many research opportunities, insights, and unlimited supports.

I also would like to thank my former and current colleagues, including Karen Kirk, Nishshanka Hewa-Kasakarage, Michael L. Kuntzman, Randy Williams, Bradley Avenson, and Caesar Garcia. They shared their invaluable knowledges with me from the beginning, which become the solid foundation for my research work.

I would like to thank all the staff members at Microelectronics Research Center at The University of Texas at Austin, especially James Hitzfelder, William James, William Ostler, and Kenneth Ziegler for managing the cleanroom facilities impeccably and Christine Wood and Jo Ann Smith for their dedicated administrative supports. Without their strong supports, I would not be able to finish my study successfully.

I also want to thank all my friends. In particular, I would like to thank Jonathan LeSage, Alexander Bleakie, Milo Holt, Emily Walker, Hema Chandra Prakash Movva, and Seungyong Jung. During the toughest moments, they believed in me and gave me cheerful words.

Lastly, I am indebted to my parents, Bangsi Kim and Sookhee Kim for their love and continual support and my sisters, Minjeong Kim and Minseon Kim, for their consistent moral support. Without my family, it would not have been possible for me to even undertake this research work.

Design of an Optical Microelectromechanical-System Microphone with Sub 15-dBA Noise Floor

Donghwan Kim, Ph.D.
The University of Texas at Austin, 2018

Supervisor: Neal A. Hall

This research work presents the modeling, fabrication, and characterization of the optical microphone. The optical microphone detects diaphragm displacement due to input sound pressure, using an interferometric-based displacement detection scheme instead of using capacitive readout technique, which is extensively used in commercial microelectromechanical-system microphones. The optical-based transduction mechanism enables a backplate design with an extremely high perforation density, which in-turn drastically reduces the backplate flow resistance, which is a dominant noise source in miniaturized microphones. Therefore, an accurate estimation of the backplate-induced flow resistance is a critical step to predict signal-to-noise ratio precisely. A flow resistance modeling technique via computational fluid dynamics is presented in this work. A prototype backplate is fabricated for a verification of the flow-resistance modeling technique. A 22.0-dBA noise floor is demonstrated using the prototype backplate, which is 6-dB better than state-of-the-art commercial capacitive MEMS microphones. Design of experiments were performed with the verified microphone model to illustrate design implications toward sub 15-dBA optical microphone. The design-of-experiments study focused on various microphone components including diaphragm compliance, acoustical low cut-off frequency, back-cavity volume, inlet port and vent to show how each parameter affect to the microphone signal-to-noise ratio and acoustic overload point. Finally, a force-feedback optical microphone concept is presented to achieve a higher acoustic overload pressure, which is defined by 10% total harmonic distortion, using a Si membrane with piezoelectric thin-film actuators. A feasibility study was performed to explore the concept of a force-feedback optical microphone, including a fabrication of the minimalistic backplate with high aspect-ratio spokes and Si membrane with piezoelectric-film actuators at Microelectronics Research Center at The University of Texas at Austin.

Table of Contents

List of Tables

List of Figures

Chapter 1

Introduction

1.1 Background / Motivation

In the early 1990s, a miniaturized silicon condenser microphone was introduced [1] [2]. Although various materials have been also introduced to fabricate a capacitive microelectromechanical-system (MEMS) microphone, the fundamental structure has not been changed [3] [4] [5] [6]. The majority of commercial MEMS microphones still utilizes capacitive readout [7] [8]. Figure 1.1 illustrates the capacitive readout technique. A pair of a conductive thin/compliant diaphragm and fixed backplate forms a variable parallel-plate capacitor. A DC-bias voltage is applied across the variable capacitor via a large resistor R_{bias}, which value is from several hundred GΩ up to several TΩ. The large time constant ($\tau = R_{bias}C_0$) makes the microphone operating in the constant-charge mode.

Under $Q = const.$, a gap change due to the diaphragm deformation leads to capacitance change ΔC. As a consequence, the AC output voltage is generated as the gap height is changed due to input sound pressure, as shown in (1.1).

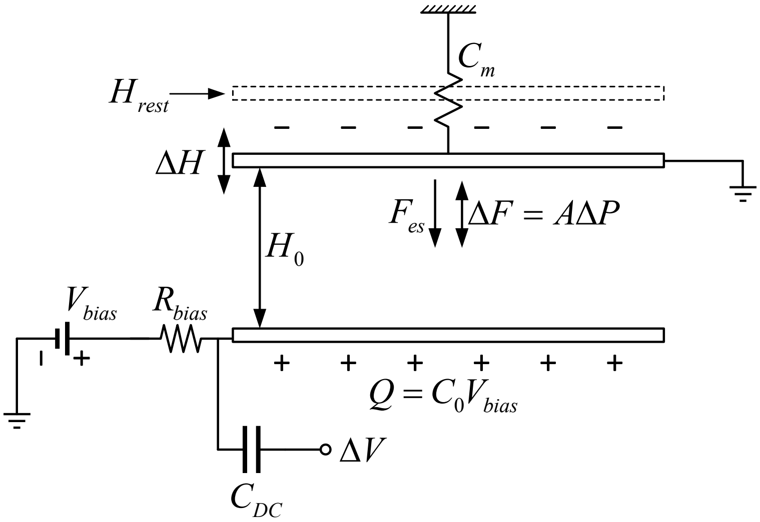

Figure 1.1: A parallel-plate model of a capacitive MEMS microphone.

$$\Delta V = \frac{Q}{\Delta C} = \frac{Q\Delta H}{\varepsilon_0 A} = \left(\frac{V_{bias}}{H_0}\right)\Delta H \tag{1.1}$$

In (1.1), the microphone sensitivity would increase with either higher V_{bias} or smaller H_0. Since the biased gap height H_0 is a function of V^2, a higher bias voltage for a higher sensitivity would also decrease the gap height, assuming the mechanical compliances of the membrane and backplate remain the same.

The noise performance of modern capacitive MEMS microphones is determined by the thermal-mechanical noise induced by thin-film squeeze air damping [9]. The damping effect is induced by the viscous losses associated with the air flow at the gap between the membrane and backplate. A smaller gap height increases the damping effect, and therefore the thermal-mechanical noise increases. A perforated backplate design is the industry standard and reduces the damping considerably [9] [10]. However, the high perforation density results in a smaller active capacitance, which causes a signal-to-noise ratio (SNR) degradation [8]. To compensate a lower capacitance due to the active area loss, the gap height must be reduced, but again the smaller gap height in-turn increases the flow resistance. As a consequence, a design compromise is inevitable in order to maximize both perforation density and active capacitance so that a best-possible SNR can be achieved [4].

The first commercialized micromachined microphone was introduced in 2002 [7], and MEMS microphones are widely adapted for consumer electronics over electret microphones. MEMS microphones offer a compact package size and a superior performance with competitive price compared to electret microphones. At a glance, commercial MEMS microphones offer a signal-to-noise ratio (SNR) from 61 67-dB, i.e., 27 33-dBA equivalent input-referred noise (EIN). For example, Analog Devices, Inc. ADMP801 microphone has the lowest EIN at present with 27-dBA EIN [11]. The higher SNR is desirable for far-field acoustic sensing applications, e.g., teleconference with a smartphone or voice recognition-based consumer electronics.

Industries put significant effort into designing MEMS microphones not only to improve microphone performance but also to reduce the size of a microphone package. A demand for smaller microphones is originated from the fact that a smaller sensor footprint is beneficial in a densely-packed consumer electronics. Due to the inevitable design compromise, designing a small-size, high-SNR, capacitive MEMS microphone is a challenging task. Although the capacitive readout technique is still one of the most attractive transduction solutions for MEMS sensors due to the fabrication simplicity, the readout scheme now becomes the limiting factor in order to realize a MEMS microphone with a drastically improved SNR over the state-of-the-arts.

To design a MEMS microphone providing a significant SNR improvement, a new readout technique is required. Optical MEMS microphone was proposed previously to eliminate the capacitive-readout scheme on MEMS microphones to achieve a higher SNR than capacitive MEMS microphones [10]. Figure 1.2 shows the schematics of both a conventional microphone and an optical microphone. The fundamental construction of the microphones is the same. Each microphone consists of a pressure sensitive and rigid backplate. However, the major difference between a capacitive microphone and optical microphone is the transduction mechanism. Instead of the capacitive-readout technique, the optical microphone utilizes a Michelson-type grating to form a phase-sensitive interferometer for sensing the diaphragm motion. A vertical-cavity surface-emitting laser (VCSEL) and photodiodes are located underneath the grating as shown in Figure 1.2(b).

The transduction change enables a low-noise backplate design without a concern of the device output impedance. A 28-dBA MEMS microphone was demonstrated with the prototype optical microphone in 2011 [12]. In this research, one of the primary goals focuses on establishing a method to predict the thermal-mechanical noise of the optical microphone accurately and

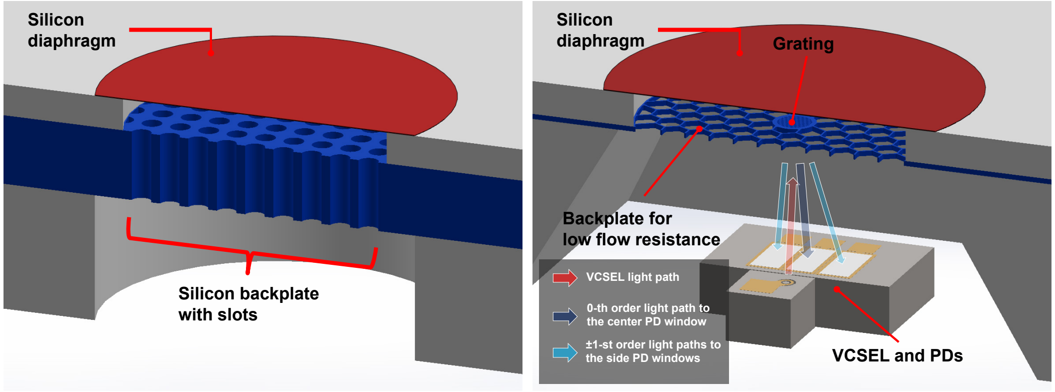

(a) (b)

Figure 1.2: Schematics of (a) a conventional capacitive MEMS microphone and (b) and optical microphone.

exploring optical microphone design for sub 15-dBA noise floor or 74-dB SNR, based on the rigorous microphone model.

1.2 Working Principle of an Optical Microphone

Unlike a capacitive MEMS microphone, an optical microphone utilizes a interferometric-based displacement sensing technique to detect the diaphragm motion. The primary role of the backplate for the optical microphone is providing a fixture for the optical grating at the center of the diaphragm. Figure 1.3(b) illustrates how the optical microphone works. The optoelectronics to detect the diaphragm motion consists of a VCSEL and three PDs to capture 0th-order and ±1st-order interference patterns respectively. The built-in VCSEL light shines the Michelson-type grating, and 50% of the beam intensity is reflected at the grating surface, while the other 50 % of the light intensity goes through the grating and is reflected by the diaphragm, i.e., a fill factor of 50%.

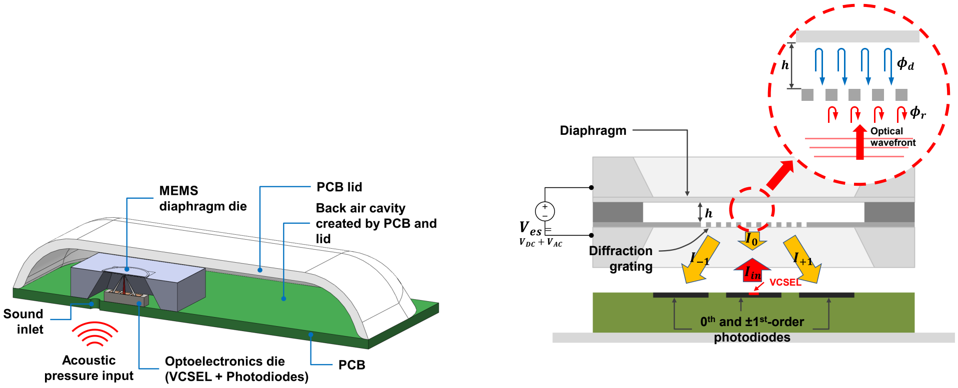

(a) (b)

Figure 1.3: (a) Illustration of the optical microphone package, and (b) schematic of the optical readout system of the proposed microphone.

When input sound pressure deforms the diaphragm, the gap h between the diaphragm and the grating is changed as shown in Figure 1.3(b). The gap change induces a phase difference between two light paths, and finally the phase difference $(\phi_r - \phi_d)$ creates 0th-order and ±1st-order interference pattern light intensities (I_0 and $I_{\pm 1}$) as illustrated in the inset of Figure 1.3(b). The light intensity variations of the 0th and ±1st order diffraction patterns are detected by the PD array, and the photocurrent outputs from the PDs are converted to voltage outputs through a TIA, which serves as a microphone output. Figure 1.4 shows a normalized light intensity vs. diaphragm gap height for the 0th-order diffraction, assuming the light wavelength as 850 nm. In the same figure, an example of an optical microphone operation range is also shown. The microphone can be operated on any position on the slope in the operation range, e.g., P1, P2 or P3. However, the diaphragm must be positioned at P2 for a maximum/linear displacement sensitivity. To actuate the diaphragm to P2, external actuation force is required. Electrostatic actuation is used for to DC tuning of the diaphragm on an optical microphone.

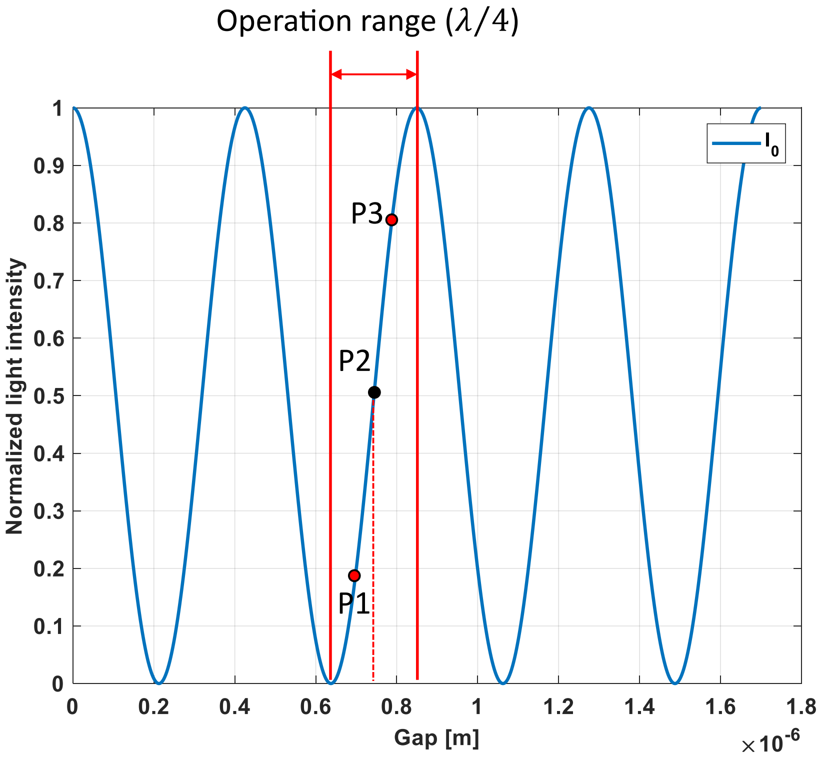

Figure 1.4: A plot of normalized light intensity vs. gap height. The wavelength of the laser is assumed as 850 nm.

Even though the conductive diaphragm and backplate are still necessary for electrostatic actuation, the changed transduction scheme enables a more flexible backplate design for optical microphones. Therefore, a high perforation density beyond that of capacitive MEMS microphones is possible. The implementation of a minimalistic backplate leads to a significant flow resistance reduction, which in-turn improves the SNR drastically, compared to capacitive MEMS microphones. Therefore, a reliable flow-resistance modeling technique is required to maximize the SNR on an optical microphone.

1.3 Objectives

The primary goal of this present work is exploring design space for an optical microphone to achieve sub 15-dBA noise floor. A comprehensive microphone model is required to simulate the system noise floor accurately. As studied by Gabrielson, the primary noise source of a miniature microphone is the thermal-mechanical noise induced by the squeeze-film damping [13] [14]. Therefore, a computational fluid dynamics (CFD)-based simulation technique is explored in this work to estimate the flow resistance of a given backplate design, followed by model validation with the fabricated prototype. Finally, the optical microphone design toward sub 15-dBA noise floor will be identified with design-of-experiments (DoE) approach.

The second goal is performing a feasibility study on a realization of the piezoelectric optical microphone. The piezoelectric optical microphone consists of two critical pieces: a minimalistic backplate and Si membrane with piezoelectric actuators. The minimalistic backplate is a necessary condition for a high-SNR microphone, and the Si membrane with piezoelectric actuators requires to counterbalance a high input pressure via force-feedback operation.

For a capacitive MEMS microphone, higher AOP is achieved by sacrificing its SNR, typically using a higher diaphragm stiffness. However, the force-feedback optical microphone is a concept to achieve higher acoustic overloading point (AOP) without a SNR degradation.

1.4 Chapter Overview

The rest of the dissertation is outlined as follows: Chapter 2 discusses the lumped-parameter network model of the optical microphone. CFD-based flow-resistance simulation of the backplate is also studied in the chapter. Chapter 3 describes the detailed fabrication processes of the first prototype backplate, followed by Chapter 4, in which the prototype microphone was tested and compared to the state-of-the-art commercial MEMS microphones. Chapter 5 explores the design space of the optical microphone to achieve the target noise floor, i.e., 15 dBA based on the model established in Chapter 2. In Chapter 6, a feasibility study of piezoelectric optical microphone is presented as a first step toward a force-feedback optical microphone to improve AOP performance, including the improved high-aspect ratio backplate design for a higher vertical stiffness. Finally, Chapter 7 presents the summary of this work and future work.

Chapter 2

System Modeling of the Optical Microphone

2.1 Overview

Capacitive MEMS microphones have been commonly modeled using the lumped-element network approach for noise spectral density and frequency response simulation [15] [5]. In the lumped-element network model, system components are represented as either mass-spring-damper in the mechanical domain, or inductance-capacitance-resistance in the electrical domain. This allows that frequency response or noise analysis can be performed simply by solving the equivalent circuit model using the well-known Kirchhoff's rules. However, it is important that each lumped parameter must represent the corresponding system element accurately. If failing do so, the model cannot represent the system accurately.

The thermal-mechanical noise analysis of a capacitive MEMS microphone via lumped-parameter approach was previously discussed in [16] [13]. Like Johnson-Nyquist noise found in electrical systems, each resistive element in the microphone system can be treated as a thermal-mechanical noise source. All resistive elements in the system also play an important role since these elements contribute to the shape of the noise floor over the target frequency range. Figure 2.1 illustrates the schematic of an optical microphone system, in which the corresponding lumped-element network model is superimposed. The lumped parameter model of an optical microphone in Figure 2.1 is fundamentally the same as capacitive MEMS microphones, except the additional optoelectronics, which enables a different displacement sensing technique in conjunction with a built-in Michelson-type grating, i.e., phase-sensitive interferometric-based optical readout, rather than the capacitive readout.

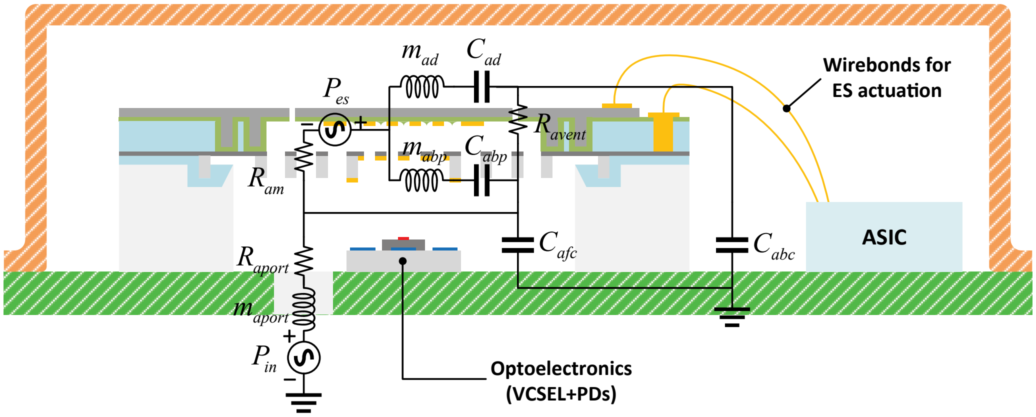

Figure 2.1: Equivalent lumped-element network model superimposed to the schematic of the proposed microphone.

Models like one shown in Figure 2.1 are used for two primary purposes: Simulating frequency response functions (i.e., sensitivity curves), and simulating thermal-mechanical noise spectra. Figure 2.2 presents noise simulation of a typical commercial capacitive MEMS microphone using the same lumped-parameter model approach.

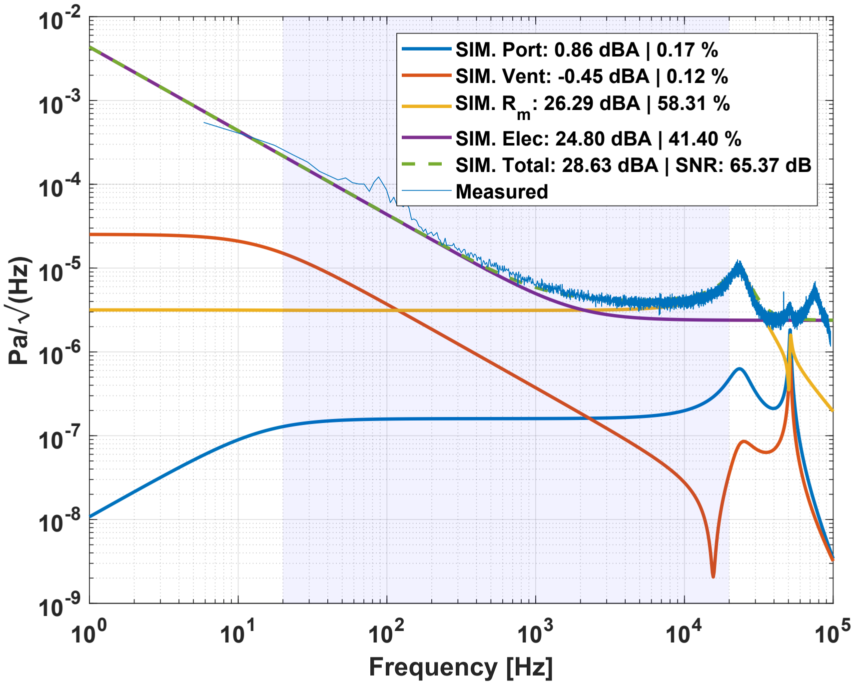

Figure 2.2: Simulated component-wise noises of a capacitive MEMS microphone. The simulated overall noise is compared to the measured noise spectrum.

The total noise can be broken down into contributors. Here is a list of important contributors for a capacitive MEMS microphone:

- R_{am}: Thermal-mechanical noise of the MEMS structure due to the flow resistance induced by the squeeze-film damping between the diaphragm and perforated backplate.
- R_{avent}: Inlet-port resistance.
- R_{avent}: Vent resistance in conjunction with the acoustic back-cavity com-

pliance.

- Electronics noise.

With respect to SNR, the primary figure-of-merit is an integrated noise with the so-called A-weighting filter applied. The A-weighted noise includes the effect that the relative loudness perceived by human depending on frequencies. The shape of the A-weighting filter is presented in Figure 2.3.

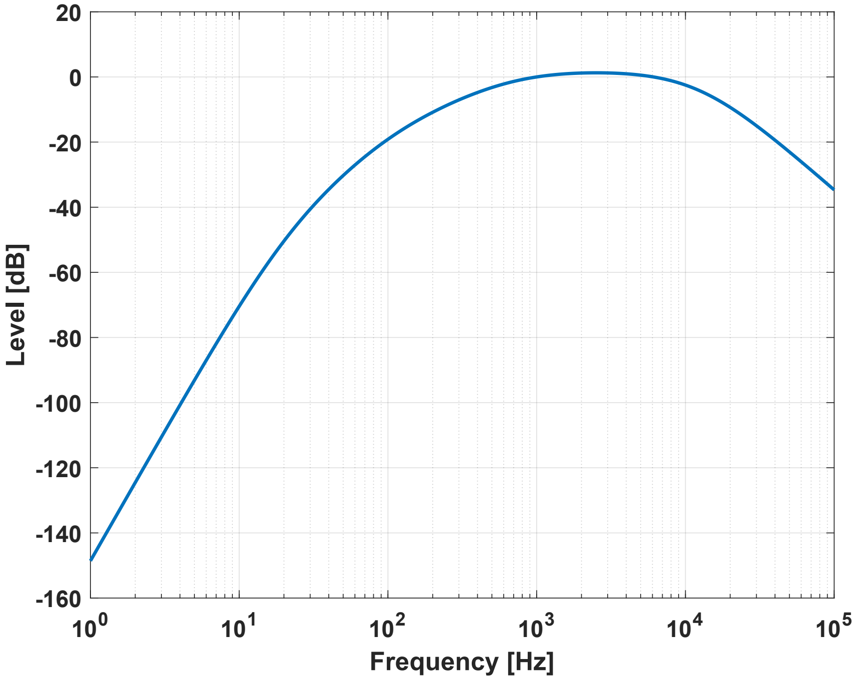

Figure 2.3: A-weighting filter defined in the International standard IEC 61672:2003.

The A-weighting filter $A(f)$ is defined in the International standard IEC 61672:2003 as shown in (2.1).

$$A(f) = \sqrt{\frac{\left(3.5 \times 10^{16}\right) \times f^8}{\left(20.6^2 + f^2\right)^2 \left(107.7^2 + f^2\right) \left(737.9^2 + f^2\right) \left(12194.2^2 + f^2\right)^2}} \tag{2.1}$$

The A-weighted noise can be obtained by integrating $P_{tm,i}$ over a frequency range, typically from 20 Hz to 20 kHz. When an input pressure-referred noise spectral density at each frequency bin is known over a frequency range, the A-weighted noise can be calculated by,

$$\text{dBA} = 20\log_{10}\left(\frac{\sum_{i=1}^{N} P_{tm,i} A(f_i)\sqrt{f_{bin}}}{P_{ref}}\right), \tag{2.2}$$

where, P_{ref} is the reference pressure (20 μPa), which is a human-threshold pressure level. A-weighted noise contributions for sample capacitive MEMS microphone presented in Figure 2.2 are presented in Table 2.1.

Table 2.1: A-weighted noise contribution for sample capacitive MEMS microphone.

Vent [dBA]	Port [dBA]	Backplate [dBA]	Electronics [dBA]	Simulated total [dBA]	SNR [dB]
-0.45	0.86	26.29	24.80	28.63	65.37

As shown in Table 2.1, the backplate damping and ASIC noise are dominant thermal-mechanical noise sources [8]. Way to reduce backplate damping is to perforate backplate to lesson value of R_{am}. This reduces active capacitance however, which in-turn increases ASIC related noise. Figure 2.4 illustrates the relationship between a smaller device capacitance and ASIC related noise, one recognizes that all field-effect transistors (FET) amplifiers have finite input capacitance, resulting in a signal division between capacitance of MEMS microphone C_{MEMS} and C_{gs} of FET, in which parasitic capacitance C_p worsens the signal loss.

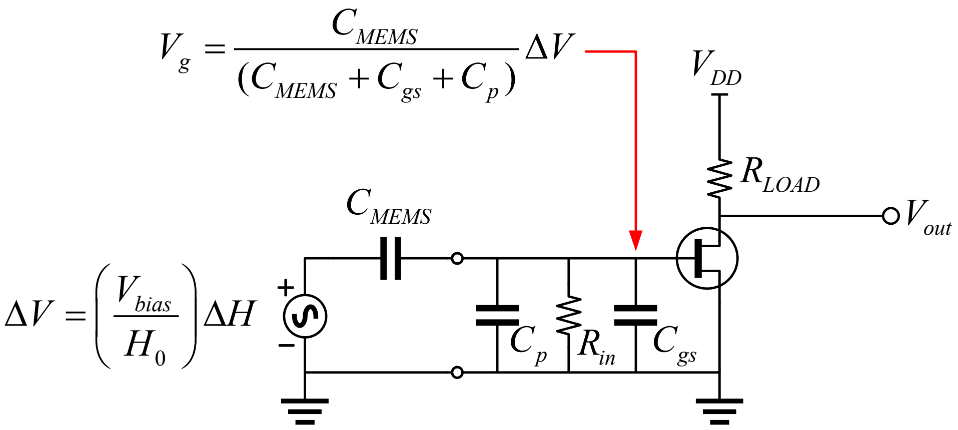

Figure 2.4: Signal degradation due to the effect of the finite input capacitance C_{gs} of the JFET and parasitic capacitance C_p.

The divider effect restricts size of FET that can be used. Small FETs have higher voltage noise at low frequencies. The design compromise between reducing flow-induced backplate noise and ASIC related noise is precisely what limits SNR of capacitive MEMS microphone. This is the advantage of the optical microphone: Decoupling this design compromise but providing high-fidelity displacement resolving of the microphone diaphragm independent of device capacitance. Instead of the electronics noise from the input impedance of the amplifier, the following electronics related noise contributors are considered for an optical microphone.

- Optoelectronics-related noise including shot noise of the PD and relative intensity noise (RIN) due to the noisy laser source.
- Johnson-Nyquist noise of the feedback resistance and the noises of the op-amp itself in the TIA.

The backplate damping is a dominant noise source for MEMS microphones so it warrants special attention and detailed modeling. In particular, the microphone does have an important constraint in this respect. The optical grating must be special pitch, e.g., 4 μm in this presented work. This presents unique modeling challenge.

2.2 Thermal-Mechanical Noise due to Squeeze-Film Damping

2.2.1 Flow Resistance due to the Presence of Grating

The squeeze-film damping effect is caused by viscous air flow in the gap defined by the diaphragm and the backplate. A finite element analysis (FEA), ANSYS FLOTRAN, was used to study the flow resistance at the grating region to observe this behavior. The arrayed nature of the grating enables study of flow around a single finger with application of symmetry boundary conditions on each side. Air flow induced by the diaphragm motion is input to the model, and the resulting pressure at the surface of the diaphragm is computed. The ratio P/v is a specific acoustic impedance, and multiplication by total grating area results in mechanical resistance R_m in units of N·s/m.

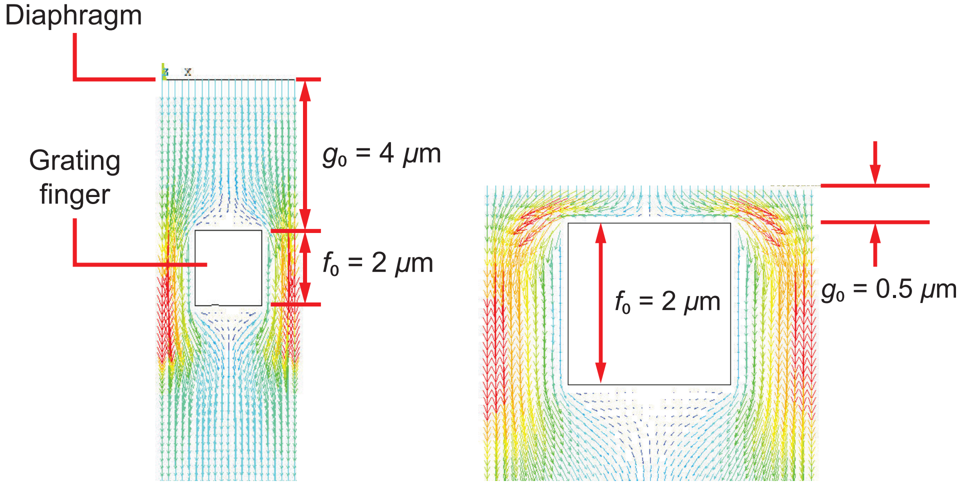

(a) (b)

Figure 2.5: Flow resistance simulation result with different gap heights, (a) $g_0 = 4$ μm and (b) $g_0 = 0.5$ μm, using ANSYS FLOTRAN.

Figure 2.5 presents a simulation result for one particular set of parameters. The grating design parameters affecting the P/v value are the diaphragm-grating gap height g_0 (e.g., 4 μm in Figure 2.5(a), the grating finger thickness f_0 (2 μm in Figure 2.5(a)), and the grating pitch and fill factor (assumed to be 50% fill factor and 4-μm pitch for all cases).

For a finger thickness, $f_0 = 2$ μm, the P/v resistance displays the trend in Figure 2.6. The damping is independent of the diaphragm-backplate gap height larger than 1 μm. In this flat region, the damping is approximately 400 Pa·s/m. Figure 2.6 also presents the specific acoustic impedance vs. gap height for a finger thickness, $f_0 = 0.8\ \mu$m. This shows a similar trend, but with smaller damping in the flat region equal to 200 Pa·s/m. A smart design is therefore to use a small gap height of 1 μm - 2 μm, as this has light damping while also keeping electrostatic-actuation voltages small.

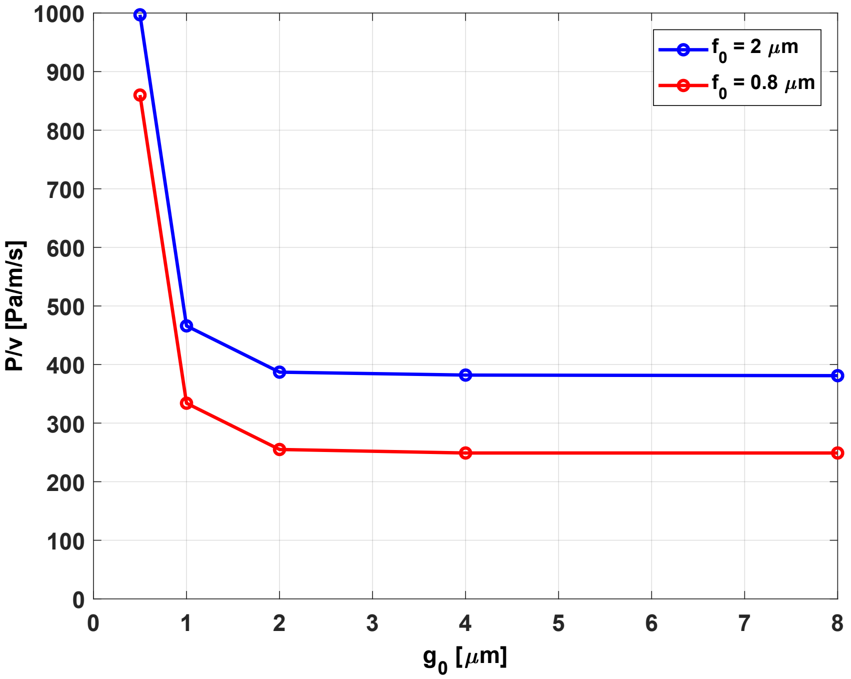

Figure 2.6: Flow resistance plot with different gap heights for two different grating finger thicknesses, $f_0 = 2\ \mu$m and 0.8 μm.

The physical explanation for flattening of the curves in Figure 2.6 is as follows: Damping is the combination of lateral shearing across the top surface of the finger and vertical shearing down the thickness of the finger. Comparing Figures 2.5(a) and 2.5(b), one can observe that lateral shearing is significant compared to vertical shearing only for the small g_0 case ($g_0 = 0.5\ \mu$m). For

g_0 greater than 1 μm, vertical shearing along the finger thickness dominates which is independent of g_0.

To identify the fundamental noise limit by the specific flow resistance R_{sp} simulated using FEA, the flow resistance R_m can be computed by,

$$R_m = R_{sp} A_{grat}, \tag{2.3}$$

where, A_{grat} is the grating area. With R_m, the input force-referred thermal-mechanical noise spectral density (N/$\sqrt{\text{Hz}}$) is defined by,

$$F_{tm} = \sqrt{4 k_b T R_m} \tag{2.4}$$

where, k_b is the Boltzmann constant ($1.3806488 \times 10^{-23}$ J/K), and T is room temperature with units of Kelvin. The Brownian motion of the diaphragm induced by F_{tm} plays an important role in achieving a high SNR microphone.

2.2.2 Effective Diaphragm Area

The computed thermal-mechanical noise F_{tm} can be represented as input pressure-referred noise P_n in units of Pa/$\sqrt{\text{Hz}}$, by simply dividing F_{tm} by the area of the diaphragm A_d in case of an ideal parallel-plate system for analysis in the acoustical domain. However, the actual diaphragm area cannot be used directly for most cases since the boundary condition for membranes on MEMS microphones is typically clamped and prohibits the piston-like motion.

Figure 2.7 illustrates the difference in displaced air volumes with a clamped diaphragm and parallel-plate model.

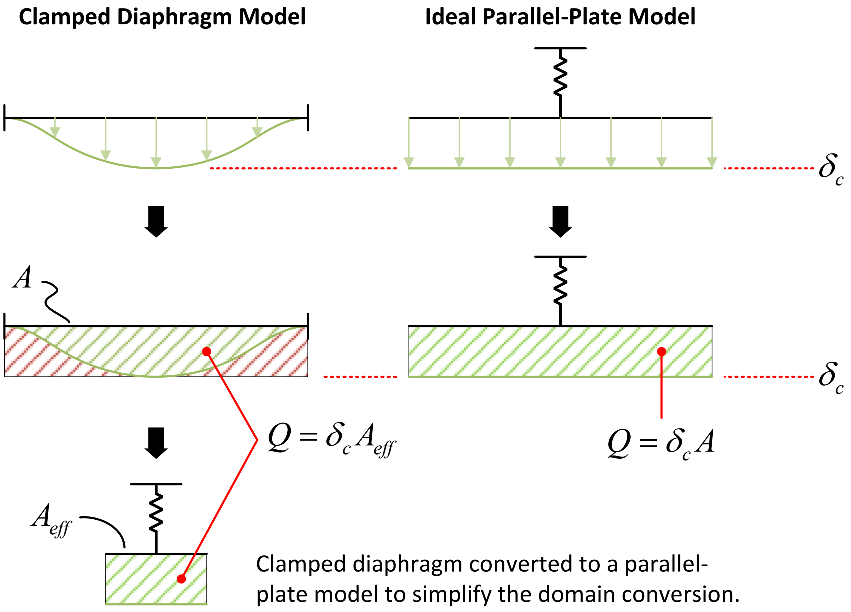

Figure 2.7: Illustration of the effective area of a clamped diaphragm.

As shown in Figure 2.7, the air volume displaced by the clamped diaphragm is lower than the parallel-plate case due to the non-uniform diaphragm deflection profile. In the figure, the difference is represented in red hatched area. The displaced air volume due to a diaphragm deflection $\delta(x, y)$ can be computed by,

$$Q = \int_A \delta\left(x, y\right) dA = \beta \delta_c A, \tag{2.5}$$

where, β, δ_c, and A are the effective area ratio of the diaphragm, the displacement at the center of the diaphragm and the diaphragm area, respectively. The effective area ratio β is required to refer the volume flow back to the center displacement of the clamped diaphragm. In this case, the effective area of the diaphragm is defined as $A_{eff} = \beta A$, which can be used for a domain conversion in a lumped-parameter model, e.g., mechanical to acoustical domain. Once A_{eff} is defined, the input pressure-referred noise spectral density P_{tm} can be computed with,

$$P_{tm} = \frac{F_{tm}}{A_{eff}}. \tag{2.6}$$

The accurate volume displacement from a complex-shaped diaphragm can be readily obtained by taking a surface integral of the diaphragm deflection using FEA. A commercial FEA package, ANSYS Workbench, is used to perform static and modal analyses to simulate diaphragm compliance and resonance frequency respectively. Figure 2.8(a) shows the z-direction static deflection contour plot of a 1-mm × 1-mm Si diaphragm displacement with 1-Pa input pressure applied normal to the diaphragm surface. The center displacement of the diaphragm is used to determine the diaphragm compliance in units of m/Pa. The simulated 1.3-μm-thick Si membrane has a diaphragm compliance C_{mp} = 44 nm/Pa and its fundamental resonance frequency was simulated as 17.5 kHz from the modal analysis as shown in Figure 2.8(b). The β for the non-tensioned clamped rectangular diaphragm is simulated as 0.2268.

It is worth to mention that β is close to 0.33 and 0.5 in case of a stress-free and tension-dominated circular membrane, respectively.

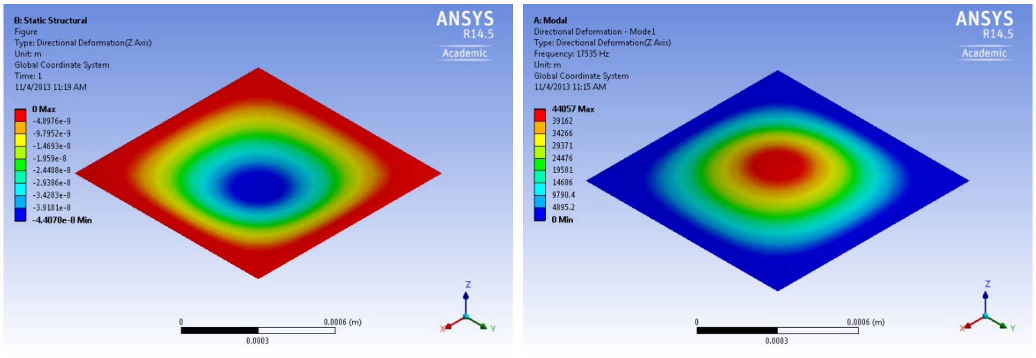

(a) (b)

Figure 2.8: FEA results of (a) the diaphragm displacement under 1-Pa input pressure and (b) the modal analysis of the diaphragm mode shape and resonance frequency with a 1.3-μm-thick Si diaphragm.

Based on the flow resistance simulation results shown in Figure 2.6, corresponding SNR values were computed without considering the noise contribution from the microphone package. Assuming a frequency range from 20 Hz to 20 kHz, the estimated SNR result suggests that the lower flow resistance of Design 2 can theoretically achieve a 12.2-dBA noise floor, or 81.8-dB SNR, as shown in Table 2.2. Table 2.2 is important because it summarizes the motivation for the optical microphone: If the thermal-mechanical backplate damping is the dominant noise limit, the upper bound of achievable noise is over 80-dB SNR, which is 10-dB higher than capacitive MEMS microphones.

Table 2.2: Fundamental A-weighted noise limit due to the thermal-mechanical noise force induced by two different grating designs.

Design	f_0 (μm)	P/v (Pa ·s/m)	d_{grat} (μm)	R_m (μN ·s/m)	d_{bp} (μm)	R_a (MPa ·s/m^3)	P_{tm} (μPa/$\sqrt{\text{Hz}}$)	Total noise (dBA)	SNR (dB)
1	2.0	400	128	5.147	1150	76.4	1.12	15.92	78.02
2	0.8	200	50	0.392	750	32.2	0.73	12.20	81.80

2.2.3 Thermal-Mechanical Displacement and Minimum Detectable Displacement

The resultant thermal-mechanical displacement of the membrane d_{tm} in units of m/$\sqrt{\text{Hz}}$ due to F_{tm}, must be resolved by the Michelson-type grating-based optical readout system so that a thermal-mechanical noise limited sensor can be achieved. The thermal-mechanical displacement noise can be computed as,

$$d_{tm} = C_m F_{tm}, \tag{2.7}$$

or,

$$d_{tm} = C_{mp} P_{tm}, \tag{2.8}$$

where, C_m and C_{mp} are the mechanical compliances in units of m/N and m/Pa respectively. A minimum detectable displacement (MDD) is a noise spectral density of the optoelectronics referred to an equivalent diaphragm displacement. For example, if the Design-2 grating in Table 2.2 is used with the simulated diaphragm shown in Figure 2.8, the resultant d_{tm} is 32 fm/$\sqrt{\text{Hz}}$. Therefore, a MDD should be lower than d_{tm} to achieve the thermal-mechanical noise limited optical microphone.

2.3 Noise from Optoelectronics

A MDD is primarily defined by the two major noise contributors; the shot noise in a photodiode and relative intensity noise (RIN) by VCSEL. To refer the shot noise and RIN to diaphragm displacement, the displacement sensitivity given by the optoelectronics should be reviewed first.

2.3.1 Sensitivity Calculation of the Interferometric-based Phase-Sensitive Displacement Detection

In the interferometric-based displacement detection scheme used for the optical microphone, the light intensities falling on to the 0th-order and ±1st-order PDs can be estimated analytically as shown in (2.9) and (2.10).

$$I_0 = I_{in}\cos^2\left(\frac{2\pi d}{\lambda}\right) \tag{2.9}$$

$$I_{\pm 1} = \frac{4I_{in}}{\pi^2}\sin^2\left(\frac{2\pi d}{\lambda}\right) \tag{2.10}$$

where, I_{in} is the incident light intensity, and λ is the wavelength of the VCSEL (850 nm). Photocurrents i_0 and and $i_{\pm 1}$ from 0th-order and ±1st-order PDs can be obtained by $I_0 R_{PD}$ and $I_{\pm 1} R_{PD}$ respectively, where R_{PD} is the responsivity (A/W) of the PD used for the setup. The output photocurrents are converted to voltage outputs using a trans-impedance amplifier (TIA). The imperfection of the optical alignment can be evaluated by measuring the modulation efficiency (ME). The ME(%) of a PD output signal is defined by (2.11).

$$\mathrm{ME} = \frac{\Delta i}{i_{\max}} \times 100(\%) = \frac{\Delta V}{V_{\max}} \times 100(\%) \tag{2.11}$$

where, $\Delta V = R_f \Delta i = R_f(i_{max} - i_{min})$, and i_{max} and i_{min} are measured from a diaphragm displacement equivalent to $\lambda/4$. The displacement sensitivity S_{PD} (V/m) for a single PD can be computed by (2.12).

$$S_{PD} = \frac{2\pi}{\lambda}\Delta V = \frac{2\pi}{\lambda} R_f \Delta i = \frac{2\pi}{\lambda} R_f i_{\max}\left(\frac{i_{\max} - i_{\min}}{i_{\max}}\right) = \frac{2\pi}{\lambda} R_f i_{\max}\mathrm{ME} \tag{2.12}$$

Note that the sensitivity in units of A/m can be obtained, simply dividing (2.12) by the feedback resistance R_f. In (2.12), S_{PD} is proportional to the light power falling onto the photodiode. S_{PD} is deteriorated with a ME less than 100%. The obtained S_{PD} enables to refer the optoelectronics noise spectral density to equivalent diaphragm displacement or input pressure.

2.3.2 Shot Noise of Photodiode and MDD

For a photodiode, the shot noise, $1/f$ noise, and Johnson noise are well-known noise sources, and the shot noise is the dominant one among the sources [17]. The shot noise is generated by the random current fluctuation through the P-N junction in the photodiode. The shot-noise spectral density can be computed by the DC photocurrent of a given photodiode. Knowing the DC photocurrent level i_{DC}, the shot noise i_{shot} in units of A/$\sqrt{\text{Hz}}$, is computed by,

$$i_{shot} = \sqrt{2qi_{DC}}, \tag{2.13}$$

where, q is the elementary electric charge (1.602176565 $\times 10^{-19}$C). With the displacement sensitivity S_{PD} in units of A/m, the MDD is finally computed by,

$$\text{MDD} = \frac{i_{shot}}{S_{PD}} = \left(\frac{\lambda}{2\pi}\right)\frac{i_{shot}}{i_{\max}\,(\text{ME})}. \tag{2.14}$$

From (2.14), it is clear that the MDD can be lowered with a higher S_{PD} and lower shot noise. When the light intensity is increased N times, the corresponding MDD is increased $\sqrt{N}$ times. Therefore, the SNR of the interferometric displacement readout system can be improved $\sqrt{N}$ times. Figure 2.9 shows the resultant MDD vs. the available light power and ME(%). In the figure, the best MDD, 2.71 fm/$\sqrt{\text{Hz}}$ is achieved with the 1-mW light power and 100% ME, whereas the worst MDD is 171.2 fm/$\sqrt{\text{Hz}}$ with the smallest light power (25 μW) and 10% ME used for the simulation.

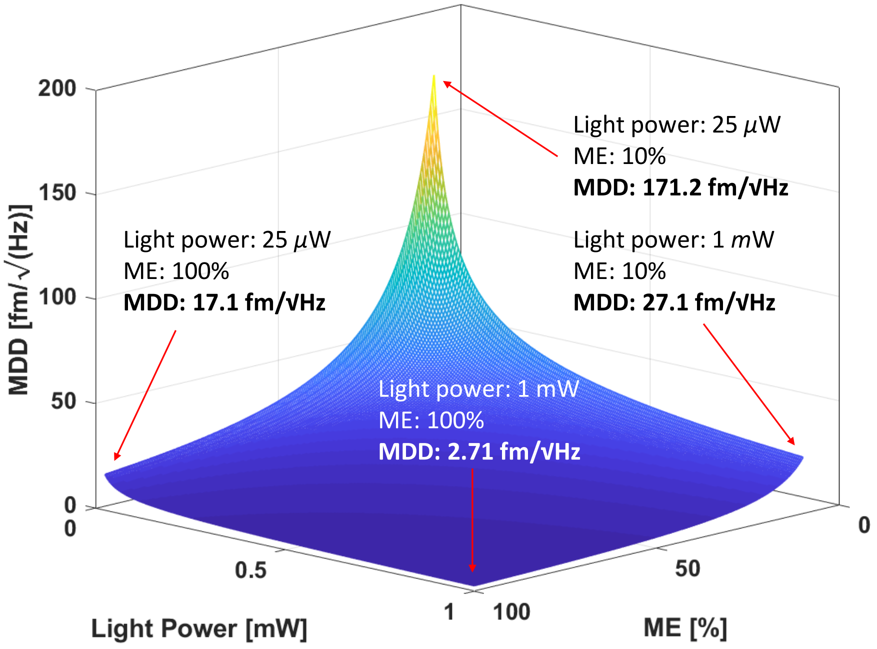

Figure 2.9: 3-D mesh plot showing the effect of the light power and ME(%) to MDD. For 1-mW laser light power, 2.7 fm/$\sqrt{\text{Hz}}$ is the best MDD, whereas a 10% ME with the same light power results in 27 fm/$\sqrt{\text{Hz}}$.

Figure 2.10 illustrates the importance of a higher ME(%). In Figure 2.10, a 1-mW light power and 100% ME results in a MDD with 2.71 fm/$\sqrt{\text{Hz}}$. However, with the same light power, a poor ME (10%) is only able to achieve 27.1 fm/$\sqrt{\text{Hz}}$. A better MDD, 17.1 fm/$\sqrt{\text{Hz}}$, can be achieved with a 25-μW light power with 100% ME. The latter case would be ideal in terms of power consumption. Therefore, a higher ME(%) is always desirable to achieve both a low power consumption and the lowest MDD (lower is better).

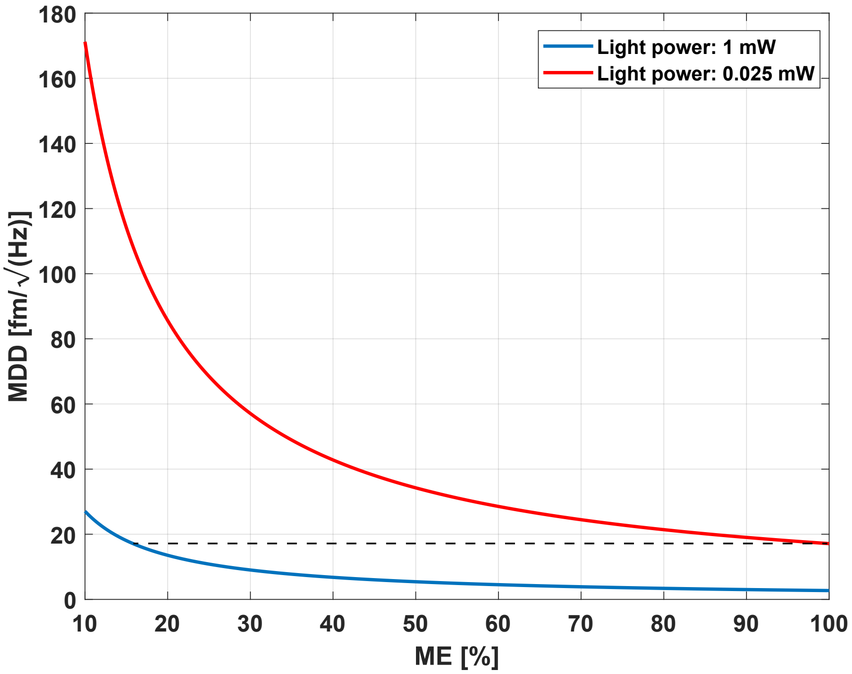

Figure 2.10: A comparison of MDD vs. ME(%) for 1-mW and 25-μW light power.

2.3.3 Relative Intensity Noise

While the shot noise of the PD fundamentally defines the MDD, the noise induced by the light intensity fluctuation from VCSEL must be considered at low frequencies, which is known as relative intensity noise (RIN). VCSEL inherently produces random light power fluctuation, and the intensity fluctuation contributes to the output noise level of the photodiode. The RIN is dominant over shot-noise effect at a low frequency range since it decays as frequency increases, i.e., $1/f$ type noise behavior. The RIN can be greatly suppressed by the RIN-cancellation scheme, demonstrated by Littrell et al. [18]. The noise cancellation performance can reach theoretically up to the shot-noise limit of the photodetector, assuming a perfect RIN cancellation. The success of the RIN cancellation is depending on whether the PD array (0th and ±1st order PDs) can detect the common-mode fluctuation simultaneously. If the PD array detects the common-mode fluctuation without any additional phase to the detected signals, the RIN can be cancelled out using a differential readout scheme. However, if the photocurrent signals have different phase to each other, the effectiveness of the RIN cancellation is drastically decreased since the common-mode RIN detected by two PDs cannot be cancelled out. Therefore, the electronics for a post signal process must be carefully designed not to add an additional phase to the detected photocurrents. To minimize the adverse effect of an additional phase, the RIN cancellation can also be done by summing the photocurrents from 0th and ±1st order PDs directly before the trans-impedance amplification stage.

2.4 Electronics Noise

For the optical detection, the photocurrents from the 0th-order and ±1st-order photodiodes are converted to voltage outputs, using a trans-impedance amplifier (TIA). To establish a shot-noise limited optoelectronics system, the TIA must provide a sufficiently low noise floor, generally at least an order of magnitudes lower noise floor, i.e., 20 dB, to properly observe the photocurrents without degrading the signals due to the noise of the amplifier itself.

For the optical microphone, total three PDs are required to capture the 0th-order (1 PD) and ±1st-order light diffraction (2 PDs) pattern, and Figure 2.11 illustrates TIA configurations for the 0th-order and ±1st-order PDs.

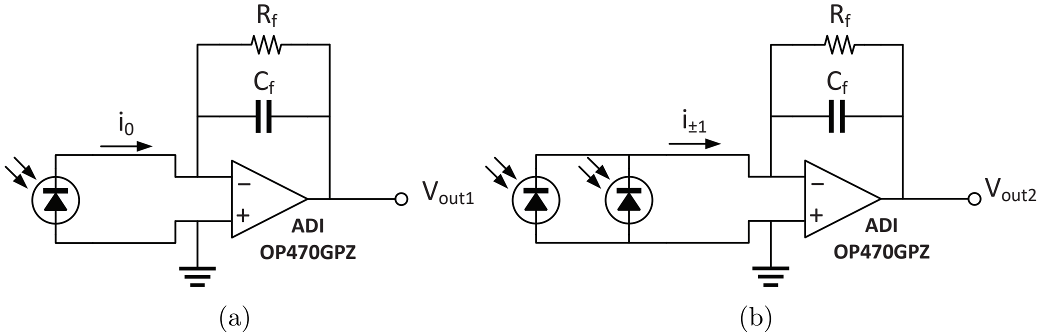

(a) (b)

Figure 2.11: TIA configurations for (a) 0th-order and (b)±1st-order PDs. Analog Devices OP470GPZ op-amp is used.

The main noise sources associated with the TIA are the current noise i_{n-} and voltage noise e_n of the given op-amp, and the Johnson-Nyquist noise from the feedback resistor R_f. The current noise at the negative terminal of the op-amp i_{n-} is transformed to output voltage noise, and the voltage output noise spectral density is given by,

$$V_{no,i_{n-}} = Z_f i_{n-} \tag{2.15}$$

where, the feedback impedance, $Z_f = R_f \parallel C_f = R_f/(1 + j\omega R_f C_f)$. The feedback capacitor C_f is added to improve the stability of the amplifier at frequencies above $f_{cut} = 1/(2\pi R_f C_f)$. If the feedback capacitor $C_f = 0$, $Z_f = R_f$. The output noise due to the op-amp voltage noise e_n is computed by,

$$V_{no,e_n} = \left(1 + \frac{Z_f}{Z_{in}}\right) e_n \tag{2.16}$$

Finally, the Johnson noise of the feedback resistor R_f can be modeled as a voltage noise source as shown in below,

$$V_{n,R_f} = \sqrt{4k_bTR_f}, \tag{2.17}$$

where, k_b is the Boltzmann constant (1.38×10^{-23} J/K), and T is room temperature. The resultant output noise due to V_{n,R_f} can be calculated by,

$$V_{no,R_f} = \frac{V_{n,R_f}}{1 + j\omega R_f C_f} \tag{2.18}$$

The overall output voltage-referred noise density of the op amp in open-circuit conditions can be obtained by incoherent summation, which is given by,

$$V_{no,total} = \sqrt{V_{no,i_{n-}}^2 + V_{no,e_n}^2 + V_{no,R_f}^2} \tag{2.19}$$

Figure 2.12 shows a simulated noise of a TIA. For the simulation, an op-amp, Analog Devices OP470GPZ, is used with the feedback loop R_f = 50 kΩ and C$_f$ = 12 pF. The op-amp has a 0.4-pA/$\sqrt{\text{Hz}}$ current noise and 5-nV/$\sqrt{\text{Hz}}$ voltage noise, which noise specs are readily available from commercially available op-amps. As shown in Figure 2.12, the output-referred voltage noise spectral density of the TIA is approximately 42 $\mathrm{nV}/\sqrt{\mathrm{Hz}}$ over the microphone operation frequency range from 20 Hz to 20 kHz. The dominant noise contributors are due to the feedback resistor and op-amps current noise.

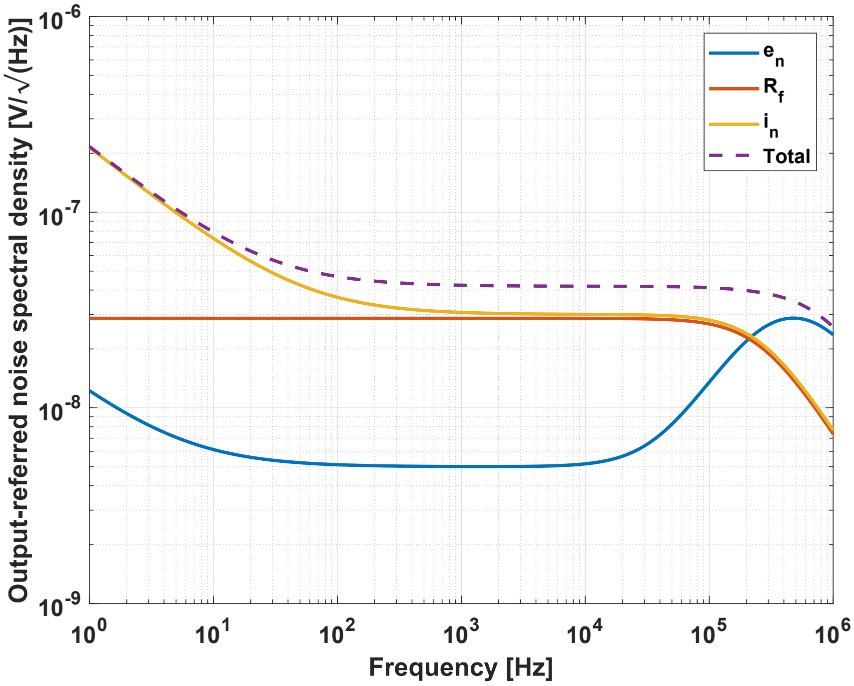

Figure 2.12: A simulated noise spectra of a TIA with ADI OP470GPZ.

Figure 2.13 shows a input displacement-referred noise floor of the TIA simulated in Figure 2.12, compared to the best MDD with 1-mW light power and 100% ME in Figure 2.9. The equivalent input-displacement referred noise of the given TIA is 0.28 $\mathrm{fm}/\sqrt{\mathrm{Hz}}$, which is 19.6-dB lower than the MDD corresponding to the simulated condition as shown in Figure 2.13. Op-amps with sub $\mathrm{fA}/\sqrt{\mathrm{Hz}}$ current noise are commercially available so the MDD-limited displacement detection system is readily realizable.

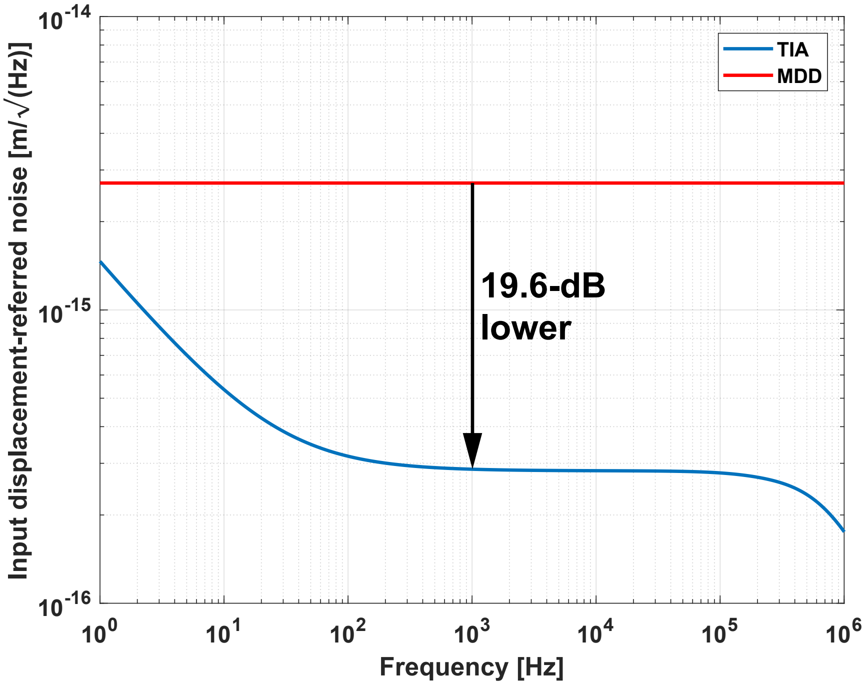

Figure 2.13: Input displacement-referred noise of the TIA compared to the lowest MDD shown in Figure 2.9.

2.5 Noise of Additional Packaging Components

Figure 2.2 is the noise plot for typical capacitive MEMS microphone. The noise spectra include the acoustical effect of the microphone packaging. Here we provide expressions for those elements. In case of bottom-inlet MEMS microphones, a PCB has a sound inlet to introduce the input sound pressure to the diaphragm. The sound inlet forms a port resistance and port mass in the acoustic domain. For a cylindrical-shaped inlet port, the inlet port resistance may be computed by,

$$\mathrm{R}_{aport} = \frac{8\eta l}{\pi a^4} \tag{2.20}$$

where, η is the kinematic viscosity of air (18.6×10^{-6} m^2/s), and l and a are the length and radius of the inlet port respectively. For the same inlet port, the acoustic port mass including the end effect is computed by,

$$m_{aport} = \frac{\rho\,(l + 1.7a)}{\pi a^2} \tag{2.21}$$

The acoustic port mass plays an important role in conjunction with the system compliance on the system resonance. Therefore, the inlet-port dimension can be tuned to achieve a target system resonance instead of adjusting the system compliance. In case of a commercial microphone, such as ST Microelectronics MP33AB01H, the inlet port radius is 125 μm, and the port length which is defined by the PCB thickness is 300 μm. The computed R_{aport} is $5.82 \times 10^{+7}$ $\mathrm{Pa} \cdot \mathrm{s/m}^3$, and the pressure-input-referred noise spectral density due to R_{aport} ($= \sqrt{4k_bTR_{aport}}$) is 0.978 $\mu\mathrm{Pa}/\sqrt{\mathrm{Hz}}$.

The other acoustical resistance taken into account for a microphone modeling is the vent resistance R_{avent} which is originated from venting holes to equalize the static pressure difference across front and back sides of diaphragm. R_{avent} and the acoustic compliance of the back cavity C_{abc} define a low cut-off frequency of a given microphone. By assuming the desired f_{cut} is 20 Hz (a lower bound of the audible sound frequency range), R_{avent} can be calculated with the known back cavity volume, V_{bc} from the spec of the microphone, e.g., 1 mm^3 for ST Microelectronics MB33AB01H. The acoustical compliance due to the back cavity is given by (2.22).

$$C_{abc} = \frac{V_{bc}}{\rho_{air} c^2} \tag{2.22}$$

where, ρ_{air} and c are the air density and speed of sound in air. The acoustical low cut-off frequency is defined by (2.23).

$$f_c = \frac{1}{2\pi R_{avent} C_{abc}} \tag{2.23}$$

When the cut-off frequency and the acoustical compliance are fixed, a required vent resistance R_{avent} is computed by $1/(2\pi f_c C_{abc})$. For example, the simulated microphone has a back-cavity compliance $C_{abc} = 7.48 \times 10^{-15}$ m^3/Pa. Therefore, the vent resistance R_{avent} should be $1.42 \times 10^{+12}$ Pa·s/m^3 to achieve a 15-Hz low cut-off frequency of the given microphone.

Acoustic radiation impedance R_{ar} is generally ignored for a noise simulation of small MEMS microphones [19]. A MEMS microphone diaphragm diameter is typically less than 1.5 mm, and therefore ka is very small, where k is the wavenumber (ω/c) and a is the diaphragm radius. Equation (2.24) shows the relationship between R_{ar} and ka.

$$R_{ar} \propto \frac{\rho S (ka)^2}{4} \tag{2.24}$$

In (2.24), a small ka leads to a small acoustical resistance relative to other resistive components.

2.6 Summary

In this chapter, the details of modeling an optical MEMS microphone is studied. The noise contributors in the optical microphone are categorized into the four major parts; thermal-mechanical, optoelectronics, electronics, and acoustical noises. The individual noise sources are used to establish a lumped parameter model to simulate the noise floor of an optical microphone. The noise model will be verified with prototype sensors in the following chapters.

Chapter 3

Prototype Fabrication and Flow-Resistance Verification

3.1 Overview

For the verification of the lumped parameter model, including the CFD-based flow resistance model, prototype devices were fabricated at the Microelectronics Research Center at The University of Texas at Austin. To build a prototype optical microphone, the diaphragm and backplate were fabricated using two separate wafers. The singulated diaphragm and backplate dies were stacked together to form the diaphragm-backplate structure. The separated-die approach provides a flexibility in terms of adjusting mechanical properties of the diaphragm and backplate with additional processes. For example, the diaphragm thickness can be easily changed with an additional reactive etching process, which is directly related to the compliance of the diaphragm, and the backplate stiffness can be controlled by depositing a tensile layer. In addition, the two-chip construction enables a characterization of the diaphragm and backplate can be observed independently.

3.2 Diaphragm Fabrication

The fabrication flow of the diaphragm module is illustrated in Figure 3.1. The diaphragm module was fabricated with a silicon-on-insulator (SOI) wafer. A 140-nm LPCVD Si_3N_4 layer was deposited and patterned for the hard mask in a potassium-hydroxide (KOH) etching process. A stoichiometry Si_3N_4 layer via LPCVD is commonly used for a KOH etching process due to the high selectivity against KOH [20].

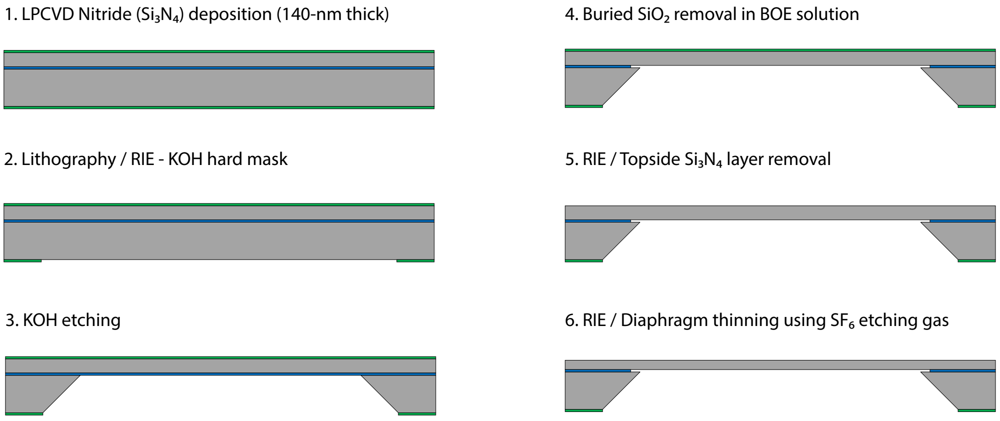

Figure 3.1: Fabrication flow of the diaphragm module.

On the backside of the SOI wafer, a KOH etching pattern was created by using a standard lithography technique (AZ5214E-IR photoresist and EVG620 aligner were used). The PR-patterned Si_3N_4 layer on the backside was etched using Oxford PlasmaLab 80+ reactive-ion etching (RIE) machine with SF_6 gas, and the etched wafer was assembled with A.M.M.T. one-side etching chuck as shown in Figure 3.2(a), and the entire thickness of the Si handle layer was etched in 90 °C 45% KOH solution.

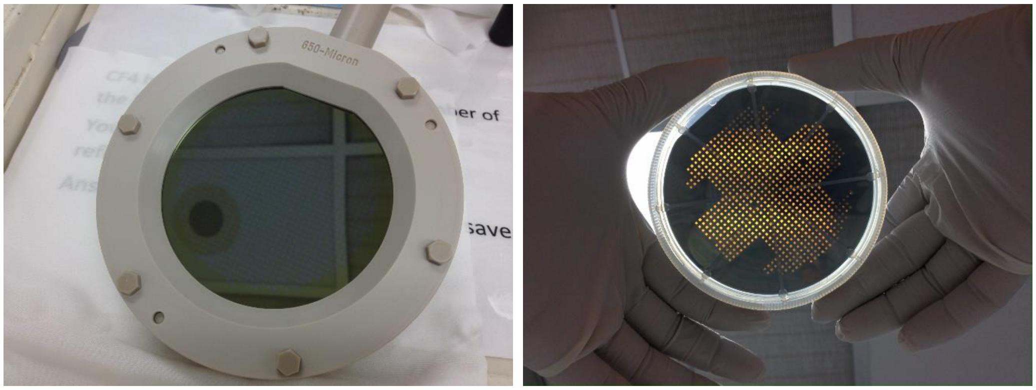

(a) (b)

Figure 3.2: (a) A wafer assembled to A.M.M.T. one-side etching chuck prior to KOH etching process. (b) A KOH-etched wafer for diaphragm modules - the 2-μm-thick diaphragms are semi-transparent.

The completion of a KOH etching is visually determined by the termination of H_2 bubble generation which is a by-product of Si etching process in KOH solution [21]. After the KOH etching, the wafer was submerged into 1:6 buffered oxide etch (BOE) solution for 15 minutes to remove the buried SiO_2 layer which causes a diaphragm deformation due to mismatched coefficients of thermal expansion (CTE) between the Si device layer and buried SiO_2 layer, caused during the SOI wafer manufacturing process (high-temperature fusion bonding). Then, each Si diaphragm die was singulated using ADT7100 dicing saw. Additional reactive-ion etching (RIE) was performed on each singulated die to thin down the diaphragm thickness for a higher diaphragm compliance. Upon a completion of the membrane, a 100-nm-think Au layer was coated on the diaphragm surface for a higher optical reflectivity, using Cressington 208 HR sputtering coater.

3.3 Backplate Fabrication

The backplate fabrication flow is illustrated in Figure 3.3. The low flow-resistance backplate module was also fabricated with a SOI wafer, which consists of a 2-μm-thick Si device layer, 1-μm-thick buried SiO_2 layer, and 500-μm-thick Si handle layer. The 2-μm-thick Si device layer was selected primarily for the thickness of grating. The fabrication of the backplate module is started with depositing a 140-nm-thick stoichiometric Si_3N_4 layer (LPCVD) on the piranha-cleaned SOI wafer. The deposited Si_3N_4 layer serves as a hard mask for a deep reactive-ion etching (DRIE) process in the subsequent step.

The backplate features, including grating fingers (2-μm width and 4-μm pitch) and 5-μm-wide honeycomb-shaped perforations, were patterned on the Si3N4 layer, using a standard lithography technique with AZ5214E-IR photoresist (PR). Then, the PR-patterned Si_3N_4 layer was etched by using Oxford PlasmaLab 80+ RIE tool with SF_6 gas.

After the topside hard-mask patterning process (1st hard mask) as shown in Figure 3.4, the backside Si_3N_4 hard mask was patterned to create a backside cavity underneath the grating and perforation structure by KOH-etching process (2nd hard mask). After the 1st and 2nd hard-mask patterning processes on the both sides of the wafer, a 2-μm-thick undoped LPCVD polysilicon (poly-Si) layer was deposited, followed by another 140-nm-thick LPCVD

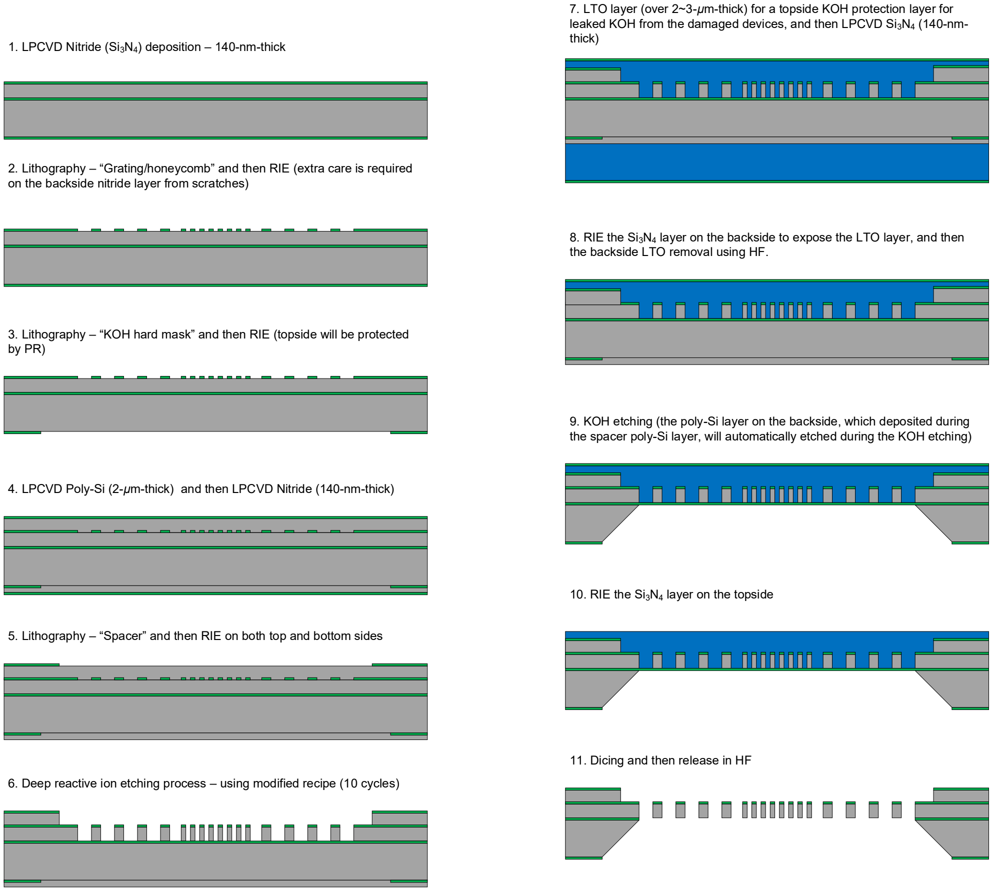

1. LPCVD Nitride (Si_3N_4) deposition – 140-nm-thick

2. Lithography – "Grating/honeycomb" and then RIE (extra care is required on the backside nitride layer from scratches)

3. Lithography – "KOH hard mask" and then RIE (topside will be protected by PR)

4. LPCVD Poly-Si (2-μm-thick) and then LPCVD Nitride (140-nm-thick)

5. Lithography – "Spacer" and then RIE on both top and bottom sides

6. Deep reactive ion etching process – using modified recipe (10 cycles)

7. LTO layer (over 2~3-μm-thick) for a topside KOH protection layer for leaked KOH from the damaged devices, and then LPCVD Si_3N_4 (140-nm-thick)

8. RIE the Si_3N_4 layer on the backside to expose the LTO layer, and then the backside LTO removal using HF.

9. KOH etching (the poly-Si layer on the backside, which deposited during the spacer poly-Si layer, will automatically etched during the KOH etching)

10. RIE the Si_3N_4 layer on the topside

11. Dicing and then release in HF

Figure 3.3: Fabrication flow of the backplate module.

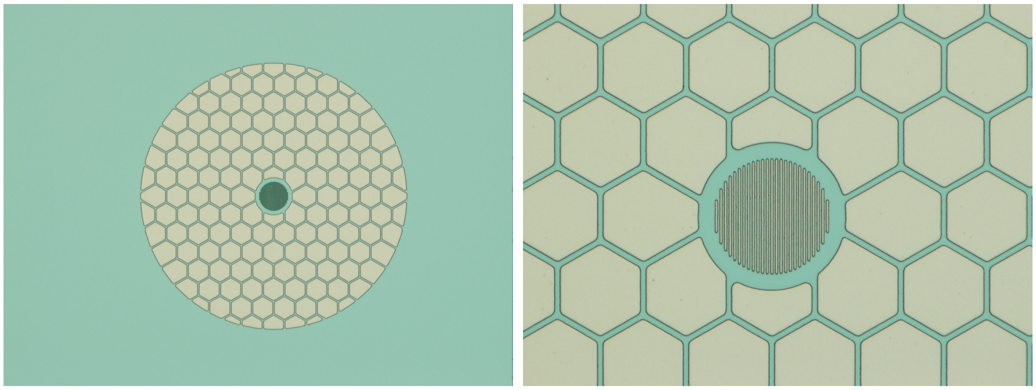
(a) (b)

Figure 3.4: After the 1st hard mask (Si_3N_4) RIE process.

Si_3N_4 layer deposition. The 2-μm-thick poly-Si layer defines the gap height between the reflector and the grating/perforation surfaces. On the deposited Si_3N_4 layer, spacer features were patterned by the same lithography technique and RIE process used for the grating hard mask pattern (3rd hard mask). Upon the completion of the 3rd hard mask layer, the Si_3N_4 layer on the backside of the SOI wafer was removed by the same RIE process. It is required to etch the backside poly-Si layer during the following KOH etching process prior to exposing the actual 2nd hard mask to form backside cavities.

After the 3rd hard-mask patterning, the remaining PR was removed by a piranha clean. The topside of the wafer was etched with a DRIE tool (PlasmaTherm DSE) to realize the spacer and grating/perforation features. Both spacer and grating features are realized in the single DRIE process. At the beginning of the etching process, the spacer structure is realized first, and then the buried Si_3N_4 grating/perforation hard mask is exposed upon the p-Si etching (spacer layer) is finished. At this point, the device Si layer is etched to realize the grating/perforation features. The buried SiO_2 layer serves as an etch stop in this DRIE process. The finished structures including grating/backplate and spacer are shown in Figure 3.5.

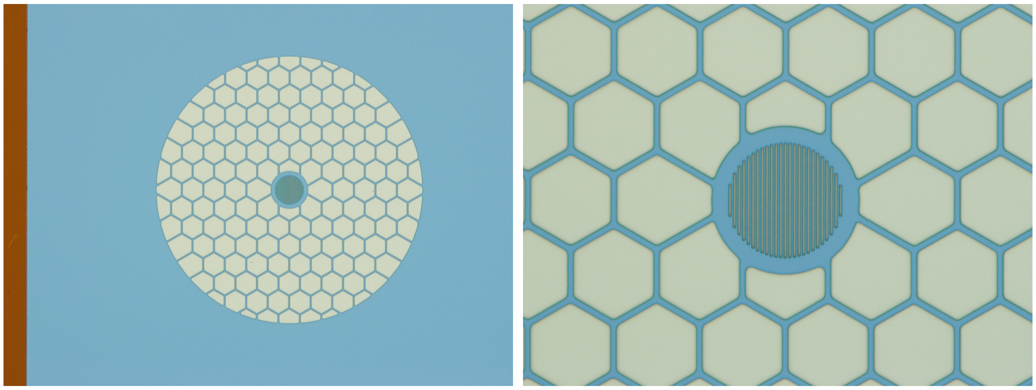
(a) (b)

Figure 3.5: After DRIE process on the top surface.

A 3-μm-thick low-temperature oxide (LTO) layer was deposited and followed by a 140-nm-thick LPCVD Si_3N_4 layer. The LTO layer provides a mechanical support to suppress an excessive deformation on the backplate structure due to the CTE mismatching in between the device Si layer and the buried SiO_2 layer when the back-cavity is realized upon a completion of the KOH etching process. In addition, the thick LTO layer provides a secondary protection for the topside structure from KOH solution in case of a failure on the topside Si_3N_4 layer. To etch the backside of the wafer selectively in KOH solution, the wafer was assembled with the A.M.M.T. single-side etcher. Prior to the KOH etching process, the wafer-assembled etching chuck was submerged into 49% aqueous HF to remove the remaining LTO layer on the backside so that Si surface can be exposed to KOH solution. The KOH etching was performed at 90 °C until the buried SiO_2 layer was exposed. Figure 3.6 shows the micrographs of the topside of the KOH-etched backplate module.

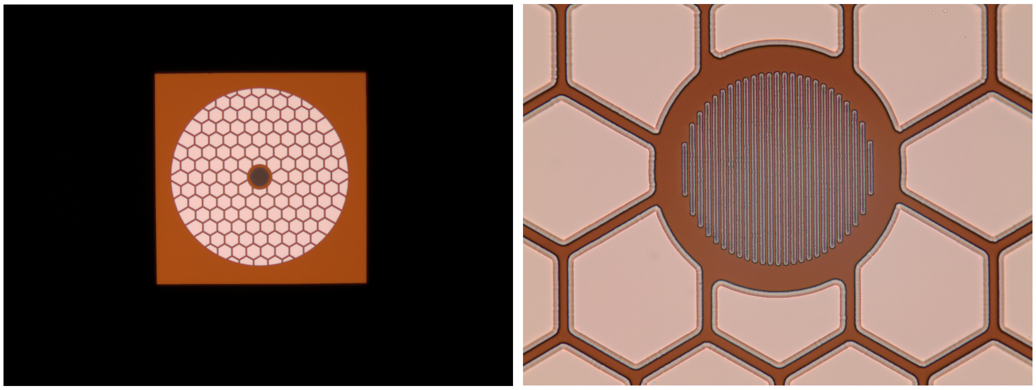
(a) (b)

Figure 3.6: After KOH etching for a back-side cavity.

After the KOH etching process, the remaining Si_3N_4 layer on the topside was removed by the RIE process, and then the wafer was diced using ADT 7100 dicing tool, and the remaining SiO_2 was released in 49% HF solution for 15 min. It was observed that the remaining Si_3N_4 hard-mask layer used for the grating/perforations induces a significant amount of deformation from the devices released for 5-min and 10-min-released devices. Since HF also etches Si_3N_4 at a slow rate, a longer release process (more than 10-min) was performed to remove the remaining Si_3N_4 so that the excessive deformation was eliminated. The micrographs of the finished backplate are shown in Figure 3.7.

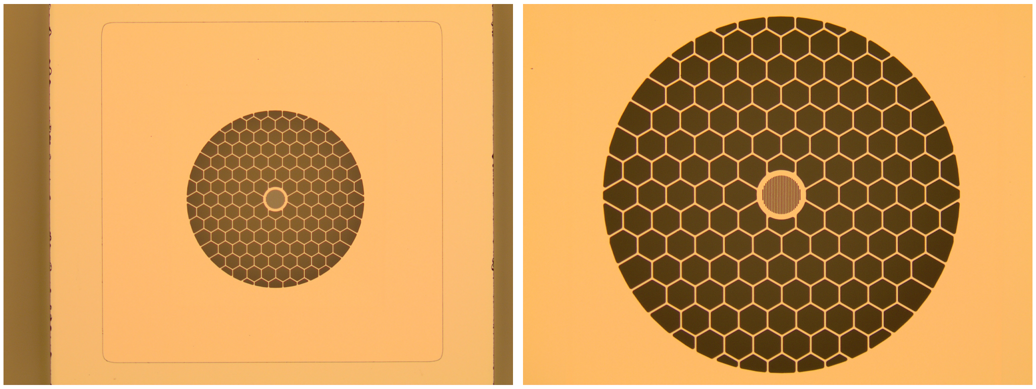

(a) (b)

Figure 3.7: Micrographs of the topside of a backplate module after a release process in 49% HF solution for 15 min.

The scanning-electron micrograph (SEM) images of the finished backplate module are shown in Figure 3.8. The KOH-etched cavity was coated with a 100-nm-think Au layer by the same method used for the optical reflective coating of the diaphragm module, as shown in Figure 3.9.

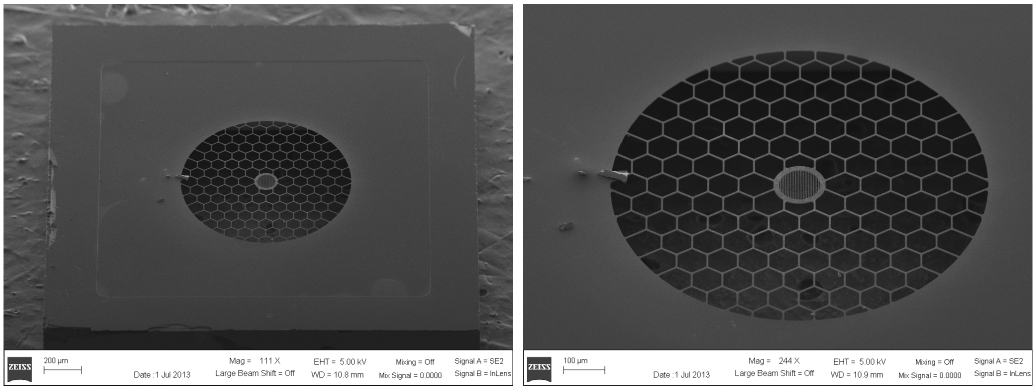

(a) (b)

Figure 3.8: SEM images of the completed backplate.

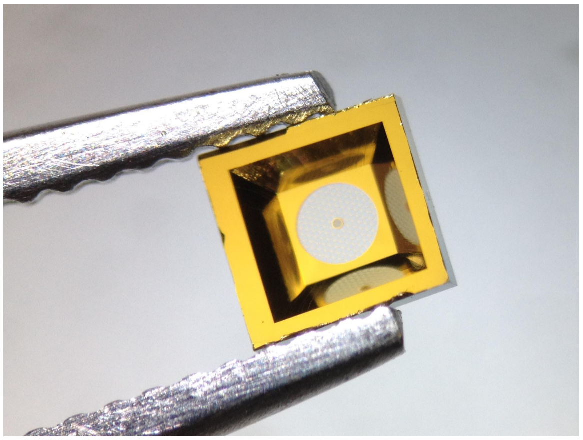

Figure 3.9: Micrograph of the Au-coated backplate.

3.4 Backplate Stiffening with PECVD Silicon Nitride

The minimalistic backplate is the key component to achieve a lower thermal-mechanical noise. In calculations presented in Chapter 2, the equivalent input-referred noise level is computed assuming that the backplate is completely rigid. However, the initial prototype testing and FEA simulation in Figure 3.10 of the prototype backplate revealed that the backplate compliance is too high to achieve the target noise level. A compliant backplate moves in response to the thermal-mechanical noise force associated with the backplate flow resistance. This motion is coherent and out of phase with the diaphragm motion in response to this same noise force. The 0th and ±1st order diffraction intensities are varied due to the relative displacement, not solely due to the diaphragm displacement. Therefore, the overall thermal-mechanical displacement noise is increased. As an example, if the backplate compliance is

6% of the diaphragm compliance, the thermal mechanical displacement noise generated by the backplate flow resistance will be 0.5-dB larger than it would be with a completely rigid backplate.

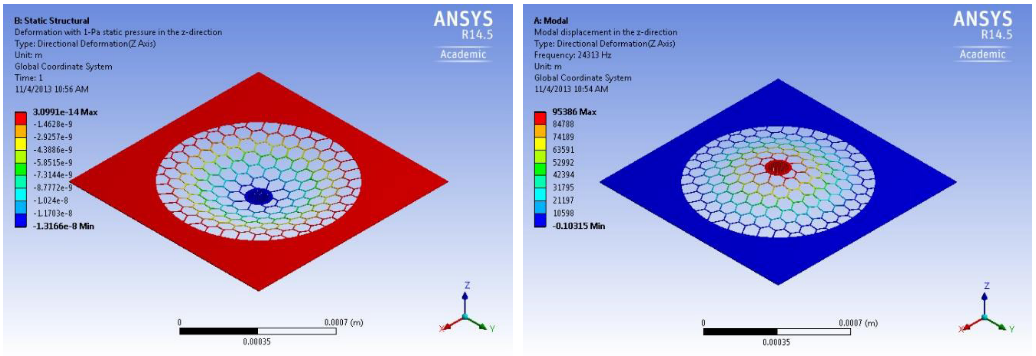

(a) (b)

Figure 3.10: FEA results of (a) the static deflection with 1-Pa input pressure, and (b) the modal analysis of the compliant backplate module.

To increase the stiffness of the fabricated backplate, a silicon nitride (SiNx) layer was deposited onto the finished backplate using PECVD as shown in Figure 3.11. SiNx induces tensile stress using CTE mismatching between the additional layer and the backplate Si layer (3.2 ppm/°C and 2.6 ppm/°C respectively). Various combinations of SiNx thicknesses on the front and back sides were attempted to produce a relatively flat backplate surface while the backplate is stiffened. Finally, 70-nm and 350-nm-thick PECVD SiNx layers were deposited at 250 °C on the topside and inside of the KOH cavity respectively, using PlasmaTherm 790 PECVD tool. Note that the topside PECVD SiNx layer is also served as the insulation layer to prevent shorting the stacked reflector and backplate module when the structure is actuated electrostatically.

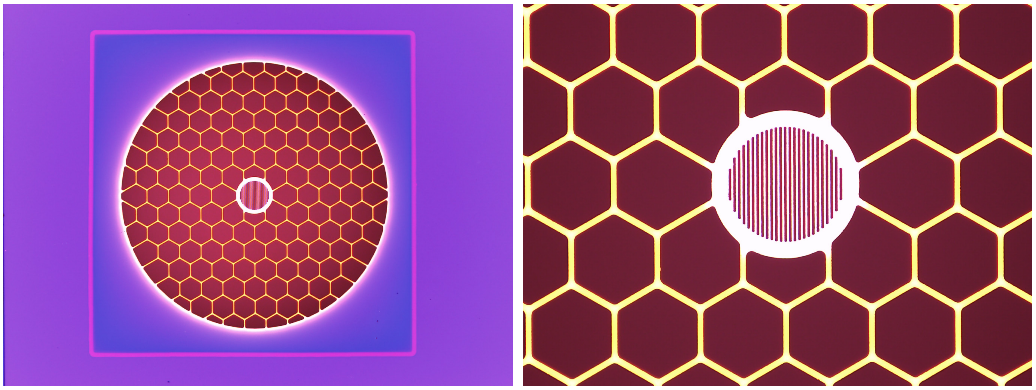
(a) (b)

Figure 3.11: Micrographs of the topside of the backplate module after PECVD SiNx deposition.

The backplate surface profile after the SiNx depositions was measured with Veeco NT-9100 optical profiler as shown in Figure 3.12(a). Using FEA, the static deformation profile of the stiffened backplate was simulated until the simulated profile is matched to the measured profile, as shown in Figure 3.12(b). In the matched case, the residual stress induced by the PECVD SiNx layers was 178-MPa tensile stress onto the backplate, which stress is within values reported from literatures [22] [23] [24]. The FEA modal analysis with the identical residual stress also predicts a drastic resonance frequency change from 24.3 kHz to 72.6 kHz before and after PECVD SiNx deposition as shown in Figure 3.12(c).

The verification of the successful stiffening was performed with an assembly of the stiffened backplate module and a rigid reflector. The rigid re-

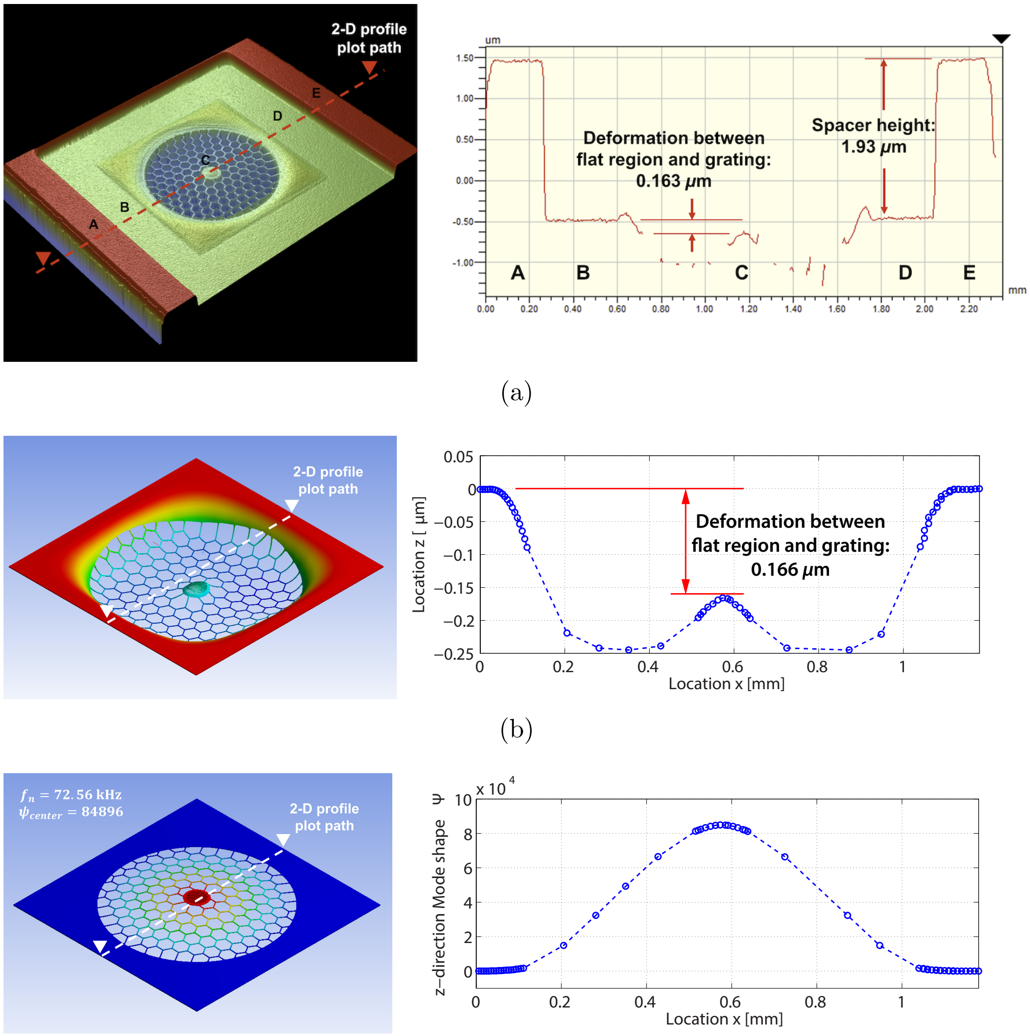

(a)

(b)

(c)

Figure 3.12: (a) Surface profilometry result with Veeco NT-9100 optical profiler and ANSYS FEA simulation results of (b) the deformation due to CTE mismatching and (c) the fundamental resonance frequency of the backplate structure after PECVD SiNx deposition.

flector was coated with 100-nm-thick Au layer to improve light reflection. The rigid reflector (a 500-μm-thick Si die) enables an observation of the backplate motion only. The frequency response of the stiffened backplate was obtained with electrostatic actuation. The backplate resonance frequency is increased from approximately 24.3 kHz to 72.6 kHz after the backplate stiffening process as shown in Figure 3.12(c). The 3× higher resonance frequency suggests that the stiffness of the backplate is increased as much as 9× compared to the original backplate.

3.5 Backplate and Grating Flow-Resistance Simulation

A 2-D grating flow resistance simulation was performed in Chapter 2. In this section, the 2-D-based flow resistance simulation is extended to a 3-D-based flow resistance simulation. The flow resistances of the fabricated diffraction grating and the honeycomb-shaped backplate region are simulated using a commercial computational-fluid-dynamics (CFD) software package, ANSYS Fluent. A laminar-flow condition is assumed for the following simulations. Separate 3-D CFD simulations are performed for the grating and honeycomb region to reduce computational effort since each model requires a high mesh density to provide an accurate solution. The integration of these results is discussed after an analysis of each section.

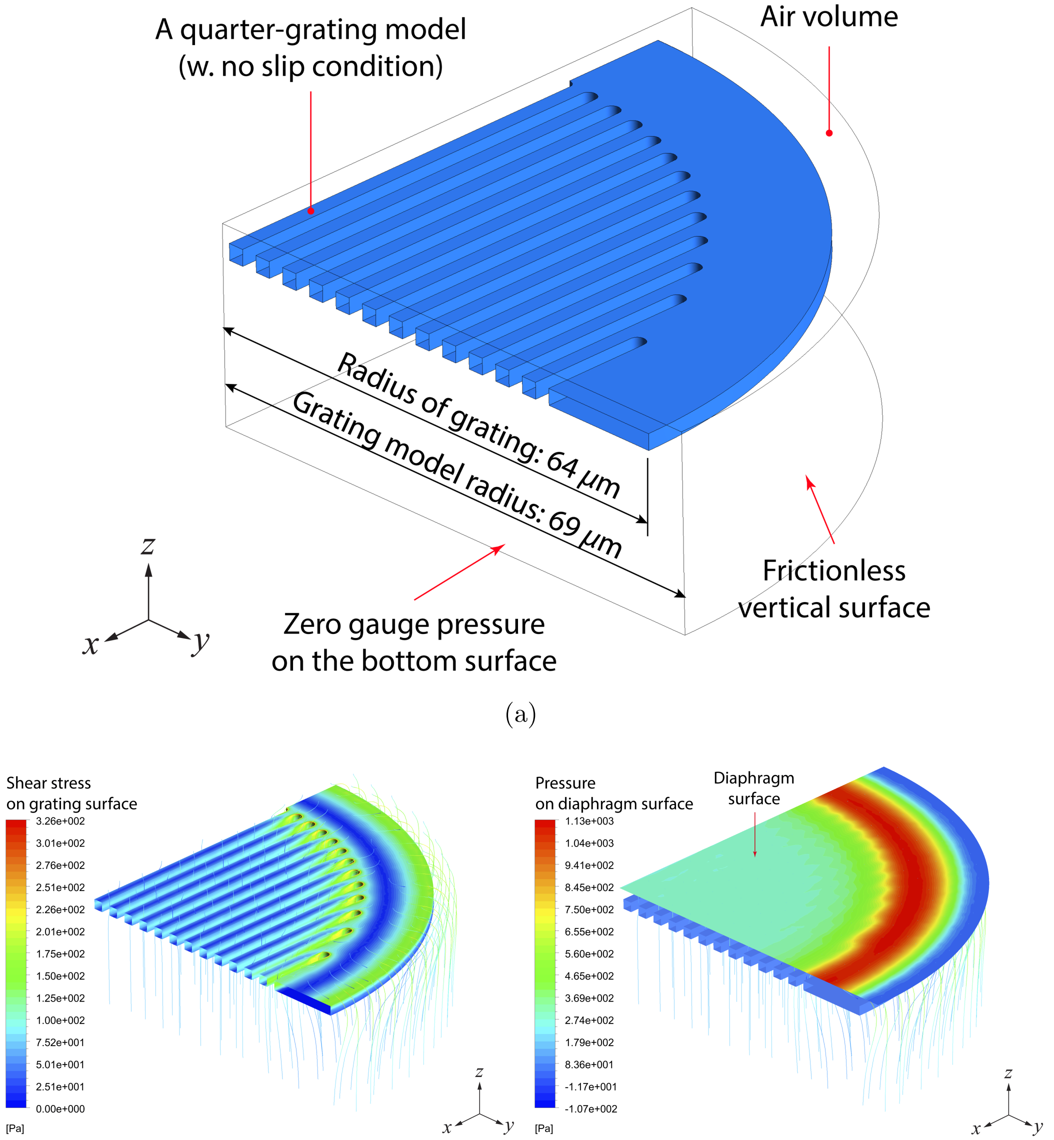

(a)

(b) (c)

Figure 3.13: (a) Surface profilometry result with Veeco NT-9100 optical profiler and ANSYS FEA simulation results of (b) the deformation due to CTE mismatching and (c) the fundamental resonance frequency of the backplate structure after PECVD SiNx deposition.

Figure 3.13 summarizes analysis of the grating region. To reduce computational effort, a 3-D quarter grating model is used instead of a full-grating model as shown in Figure 3.13(a), and the air gap between the diaphragm and the grating is set to 2 μm, as this is the measured gap in the grating region per the results presented in Figure 3.12(a). The diaphragm-induced airflow is modeled by setting a uniform 1-m/s velocity inlet normal to the diaphragm surface (i.e., 1 m/s in the z-direction). The total volume of air meshed is everything within the lines shown in Figure 3.13(a). As labeled in Figure 3.13(a), the vertical exterior surface of the air is set to a frictionless surface while the grating surface follows the no-slip condition. The bottom surface is set to atmospheric pressure, i.e., zero-gauge pressure. The flow resistance in units of N·s/m is computed by taking a surface integral of static pressure over the diaphragm surface. The flow resistance was monitored to confirm the convergence of the surface integral value within a tolerance equal to 4 significant digits. From the simulation, the flow resistance for the quarter model is computed as 1.831 μN·s/m. Thus, the flow resistance induced by the full grating becomes 7.324 μN·s/m.

A similar analysis is performed on a unit cell of the honeycomb-shaped backplate perforations as shown in Figure 3.14(a). The width and thickness of the beams forming the honeycombs are 5 μm and 2 μm respectively, as labeled in Figure 3.14(b). Thus, the beam width in the unit honeycomb cell is 2.5 μm. A symmetry boundary condition is applied to the vertical surface of the exterior of the air volume, and a no slip condition is applied to the honeycomb surfaces.

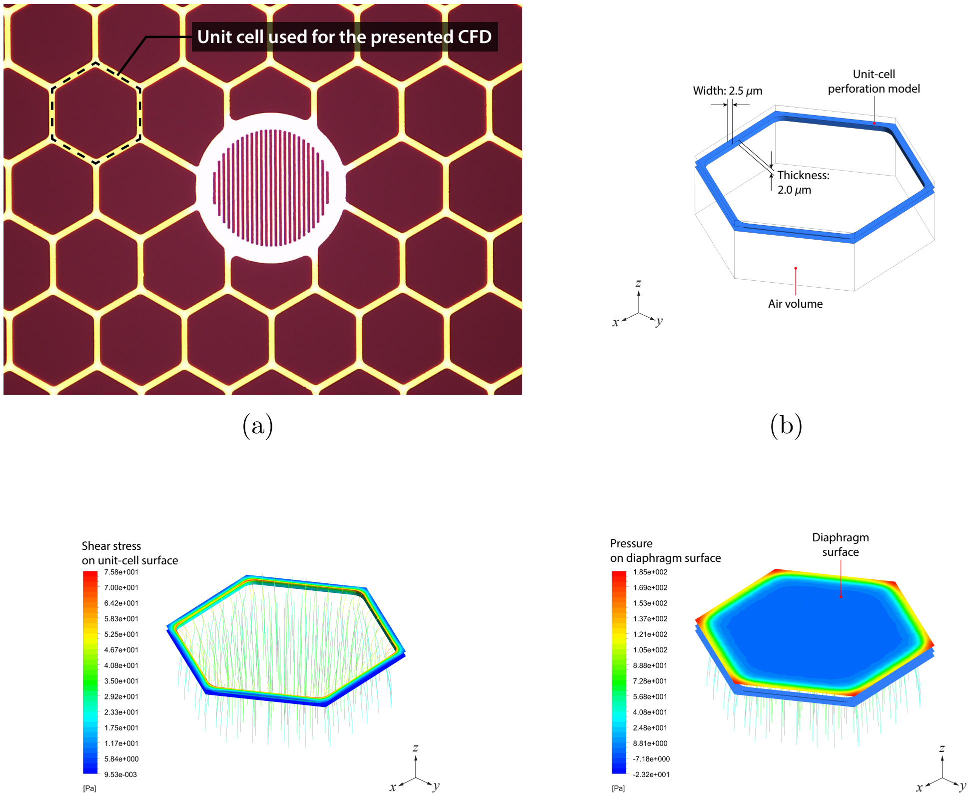

(a) (b)

(c) (d)

Figure 3.14: ANSYS Fluent simulation was performed on (a) one of the back-plate honeycomb-shape perforations, and (b) the unit-cell geometry is built for the CFD simulation. The contour plots show (c) the shear stress on the unit-cell honeycomb structure and (d) the pressure on the diaphragm due to the viscous air flow induced by the diaphragm motion, i.e., -1 m/s in the z-direction). Streamlines are also shown on (b) and (c) to visualize air flow through the unit-cell honeycomb structure.

The air gap between the honeycomb and diaphragm is assumed to be 2.5 μm following the measured backplate deflection profile in Figure 3.12(a) in the honeycomb region. The flow resistance for the unit cell is computed as 0.1097 μN·s/m.

The damping simulations are performed under uniform diaphragm-deflection conditions which would be applicable to piston-type motion of a diaphragm-backplate system. The majority of MEMS microphone diaphragms are clamped to rigid supports along the perimeter, and thus the deformation profile is not uniform. For non-piston type deflection profiles between the diaphragm and backplate, a rigorous way to compute total system damping is to use a modal coordinate description of the deflection.

In this procedure, the first vibration mode of the diaphragm is used as a basis function such that the distributed diaphragm deflection is $u_d(x, y, t) = \psi_d(x, y)\eta_d(t)$, where $\psi_d(x, y)$ is the first mode shape of the diaphragm and is normalized to have a value of unity at the center.

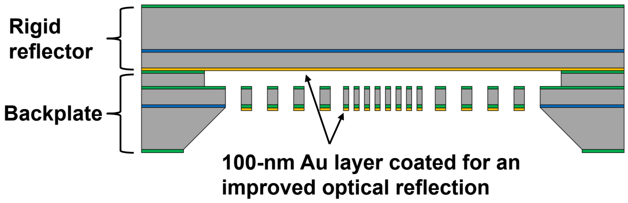

Figure 3.15: A schematic of the test assembly, consisting of the completed backplate mounted against a rigid reflector surface.

For the test structure presented in this work illustrated in Figure 3.15, the diaphragm is a rigid reflector and the backplate is the vibrating element under electrostatic actuation. The relative displacement between the reflector and backplate is therefore $u_{bp}(x, y, t) = \psi_{bp}(x, y)\eta_{bp}(t)$ where $\psi_{bp}(x, y)$ is the first vibration mode of the backplate for the test structure. η_{bp} is therefore a modal coordinate, and when using this analytical framework the mass, compliance, and damping of the system have rigorous mathematical definitions. In particular, modal damping is defined as,

$$R_m = \iint_A R_{sp}\psi_{bp}^2(x, y)dA \tag{3.1}$$

where, R_{sp} is the specific damping defined as the backplate damping per unit area with units Pa·s/m. R_{sp} is different for the honeycomb and grating regions, and the integral may therefore be divided and computed as follows:

$$R_{m,grat} = 2\pi \int_0^{r_g} R_{sp,grat}\psi_{bp}^2(r)dA \tag{3.2}$$

$$R_{m,hc} = 2\pi \int_{r_g}^{r_{bp}} R_{sp,hc}\psi_{bp}^2(r)dA \tag{3.3}$$

where, r_g and r_{bp} are the radii of the grating and backplate, respectively. The first mode shape of the backplate is obtained from ANSYS Workbench. The extracted mode shape is discretized due to the perforations, so the discrete profile is fitted with a 10th-degree polynomial in MATALB to obtain a continuous profile, which is required to compute the integral in (3.2) and (3.3). The continuous mode shape is presented in Figure 3.16.

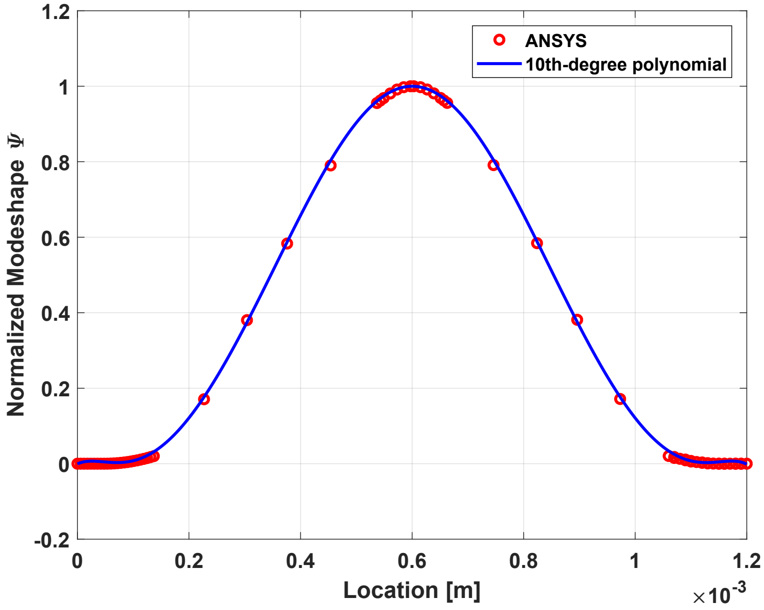

Figure 3.16: The first mode shape profile presented in Figure 3.12(c) is normalized to have a value of unity at the center and then fitted with a 10th-degree polynomial fit which provides a continuous mode shape profile for the flow resistance calculation.

Equations (3.2) and (3.3) also require computation of $R_{sp,grat}$ and $R_{sp,hc}$. In the CFD simulation, the flow resistance for the 138-μm-diameter grating region, labeled in Figure 3.13(a), is computed as 7.324 μN·s/m. The specific flow resistance of the grating is therefore calculated as,

$$R_{sp,grat} = \frac{R_{m,grat}}{A_{d,grat}} = 489.8 \text{ Pa} \cdot \text{s/m} \tag{3.4}$$

The flow resistance for the honeycomb unit cell is computed as 0.1097 μN·s/m with ANSYS Fluent, and the area of a unit cell is 4779 μm^2. Thus, the specific flow resistance for the honeycomb region is computed as,

$$R_{sp,hc} = 22.96\ \mathrm{Pa} \cdot \mathrm{s/m} \tag{3.5}$$

With specific flow resistances $R_{sp,grat}$ and $R_{sp,hc}$ from (3.4) and (3.5), computation of the total mechanical system damping R_m is,

$$R_m = R_{m,grat} + R_{m,hc} = 8.961\ \mu\mathrm{N} \cdot \mathrm{s/m}. \tag{3.6}$$

The complete model for the test structure is summarized in Figure 3.17(a). The modal mass and compliance of the backplate are obtained directly from ANSYS. The network model in Figure 3.17(a) is used to simulate the center point backplate deflection in response to electrostatic excitation with the result presented in Figure 3.19.

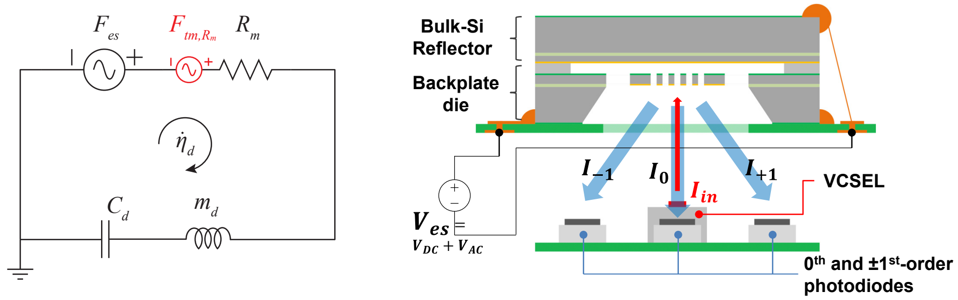

(a) (b)

Figure 3.17: (a) The equivalent circuit model of the backplate testing structure and (b) a schematic of the backplate testing setup for a frequency response measurement with electrostatic actuation.

The goal of experimental evaluation is to perform system identification (ID) on the backplate. Specifically, the goal is to measure the frequency response and extract the resonance frequency and quality factor (Q) for comparison against simulated values. To accomplish this goal, the backplate module presented in Figure 3.15 was configured for optical readout as summarized in Figure 3.17(b). Electrostatic actuation between the reflector and the backplate in combination with optical readout is used to measure the frequency response of the backplate system. An 850-nm VCSEL is used to illuminate the grating/reflector system, and inner and outer PDs were set in place to measure the center (i.e., 0th-order) and outer (i.e., ±1st-order diffracted beams) intensities. A schematic of this setup is presented in Figure 3.17(b). Center- and outer-beam photocurrents were amplified and converted to a voltage using trans-impedance amplifiers (TIAs) with a feedback resistor, $R_f = 50$ kΩ.

To confirm successful operation of the optical-readout technique, a first experiment was performed in which a slow-varying, high-voltage triangle actuation-voltage waveform is input to the device while 0th-order and ±1st-order beam signals are measured. Figure 3.18 presents both the input triangle waveform and the resulting PD signals. As expected [25], the center and outer beam intensities are complimentary and display high ME(%) while several interference cycles are traversed. The frequency response was then measured by biasing the system to a point of maximum sensitivity and linearity on one the curves while applying a broadband, small-signal AC voltage in the form of white noise.

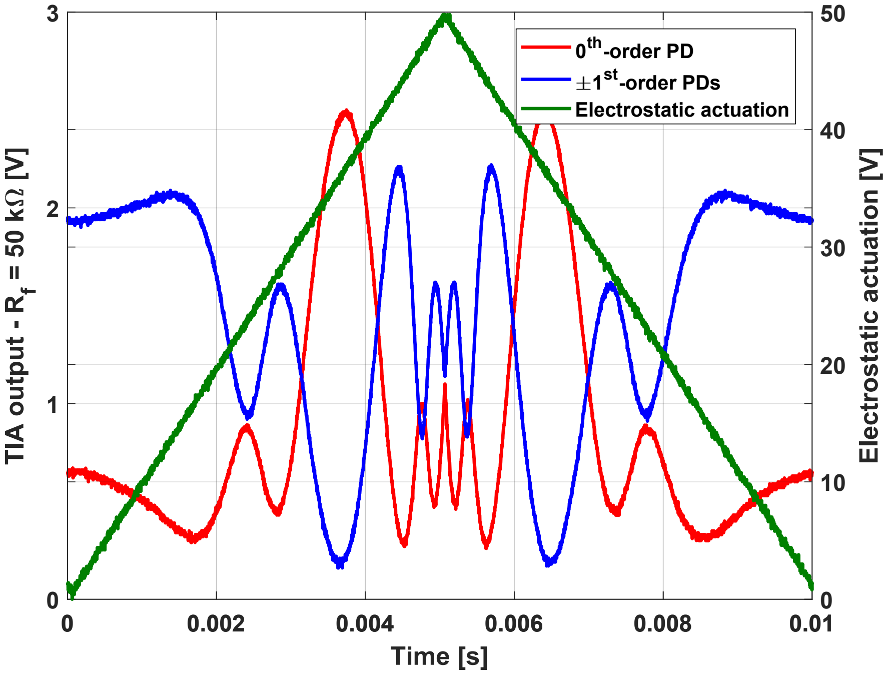

Figure 3.18: Measured PD output signals with a triangular input signal.

The measured output fast-Fourier-transform (FFT) amplitude spectrum is normalized to the input to obtain the frequency response presented in Figure 3.19. To ensure a linear measurement, the input signal was very small and increased only to the point of allowing the fundamental resonance frequency and Q to be visible and measured. The Q is very close to the predicted value based on the damping simulation (9.20 vs. 9.97). The measured f_n and Q, in combination with the modal mass, are used to compute the experimentally extracted R_m as 8.23 μN·s/m. The extracted R_m is in close agreement with the simulated value within 8.2% agreement.

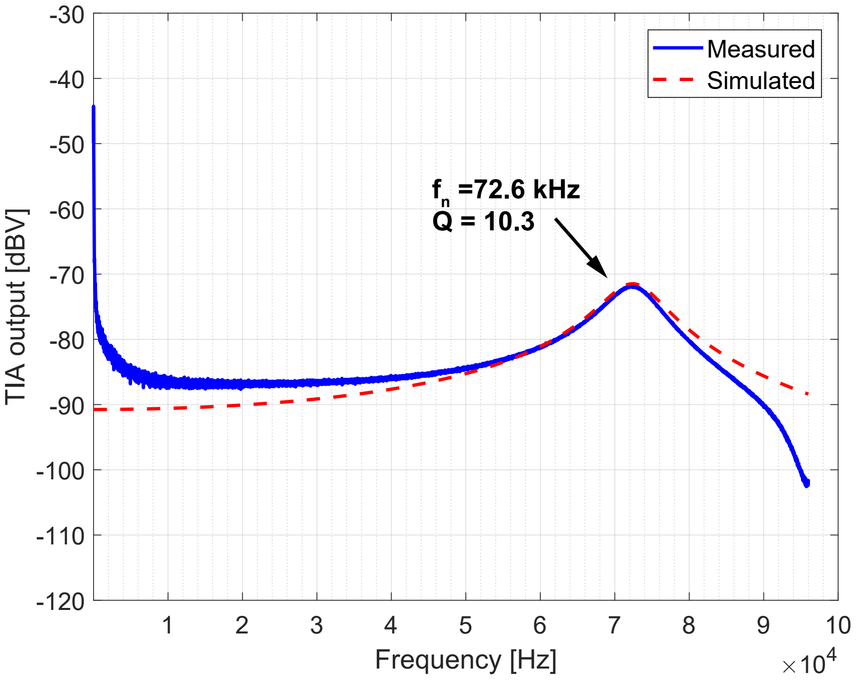

Figure 3.19: Frequency response of the backplate module with electrostatic actuation.

3.6 Summary

The first prototype device is fabricated using SOI wafers with a 2-μm-thick device Si layer. The first prototype utilizes two-chip solution, in which diaphragm and backplate are fabricated separately for rapid prototyping and robust characterization by testing them independently. A backplate-reflector system was constructed first to isolate study of the grating damping with minimal additional variables that would otherwise be introduced in a fully functional microphone. The CFD-based grating flow-resistance model was experimentally validated with the prototype backplate. It is also found that thin backplates can be tensioned using tensile layers such as PECVD SiNx, and that the resulting deformation does not significantly affect optical performance in adverse ways.

Chapter 4

Analysis of the Prototype Optical Microphone

4.1 Overview

In Chapter 3, the fabricated prototype backplate was independently characterized. The CFD-based flow-resistance modeling technique was experimentally validated with the fabricated backplate. This section presents the process of building a diaphragm-backplate structure. In the later section, the diaphragm-backplate structure is used to measure the displacement sensitivity and modulation efficiency. Each noise component discussed in Chapter 2 was measured separately and compared to the model. Finally, a fully-packaged optical microphone was tested with commercially available capacitive MEMS microphones.

4.2 Construction of a Diaphragm-Backplate Structure

Figure 4.1 shows the construction of the diaphragm-backplate structure. The stiffened backplate die using PECVD SiNx was attached on to the dedicated PCB first, using conductive epoxy (Epoxy Technology EPO-TEK H20E). The conductive epoxy establishes an electrical connection to the backplate for electrostatic actuation. An Au-coated diaphragm was stacked on top of the mounted backplate. Two dies were attached together using DYMAX UV-cured epoxy. The gap between diaphragm and backplate is defined by the 2-μm-thick polycrystalline-Si (p-Si) spacer built on the backplate die.

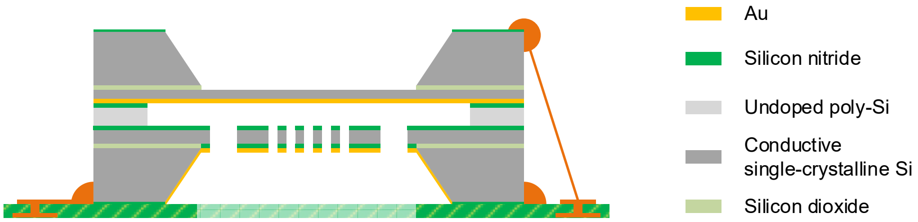

Figure 4.1: Schematic of the assembled prototype device.

Finally, a 25-μm-diameter Au wire was used to establish electrical connection to the diaphragm for electrostatic actuation. The diaphragm-backplate structure with different zoom levels is shown in Figure 4.2. Figures 4.2(c) and 4.2(d) confirm the gap between the backplate and diaphragm formed by the 2-μm-tall p-Si spacer on the backplate die.

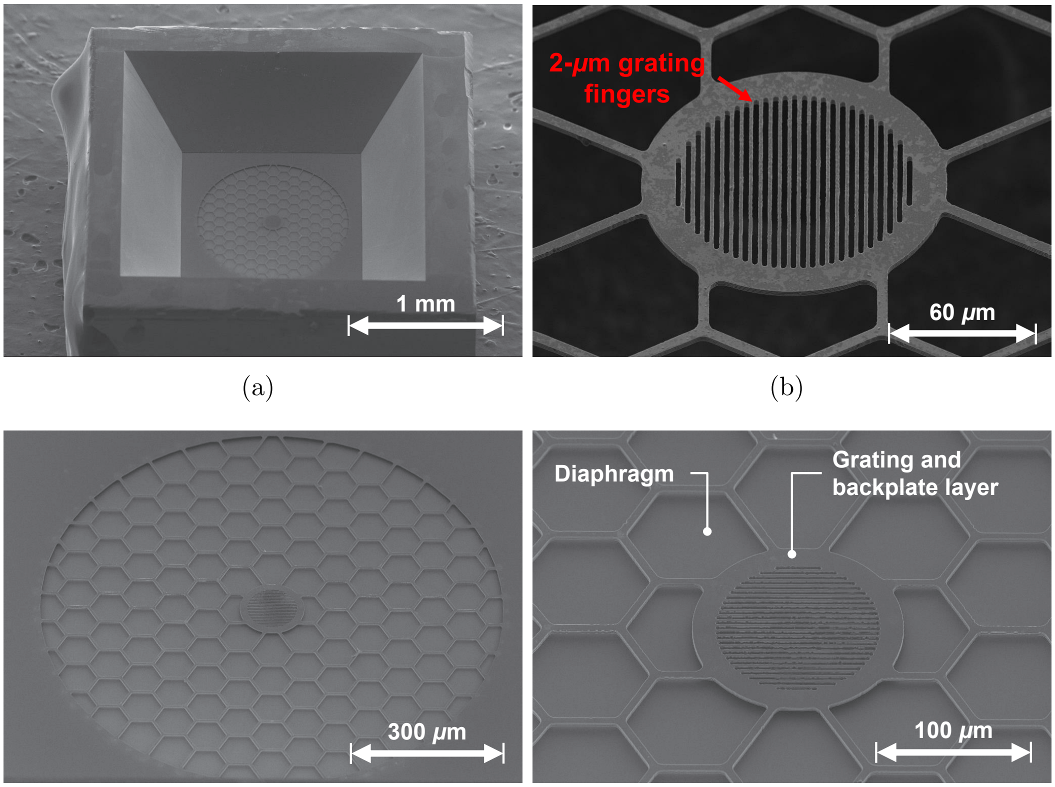

(a) (b) (c) (d)

Figure 4.2: SEM images of the assembled prototype devices (a) overview from the backside, (b) magnified view of the grating, (c) magnified view of the perforations, and (d) magnified view of the grating, perforation, and the gap between diaphragm and backplate.

4.3 Measurement Setup

The assembled prototype was fixed on the stage, and the optoelectronics was mounted on a 3-axis optical stage as shown in Figure 4.3. The 3-axis optical stage enables a precise alignment of the optoelectronics with respect to the prototype sensor to achieve a high modulation efficiency (ME).

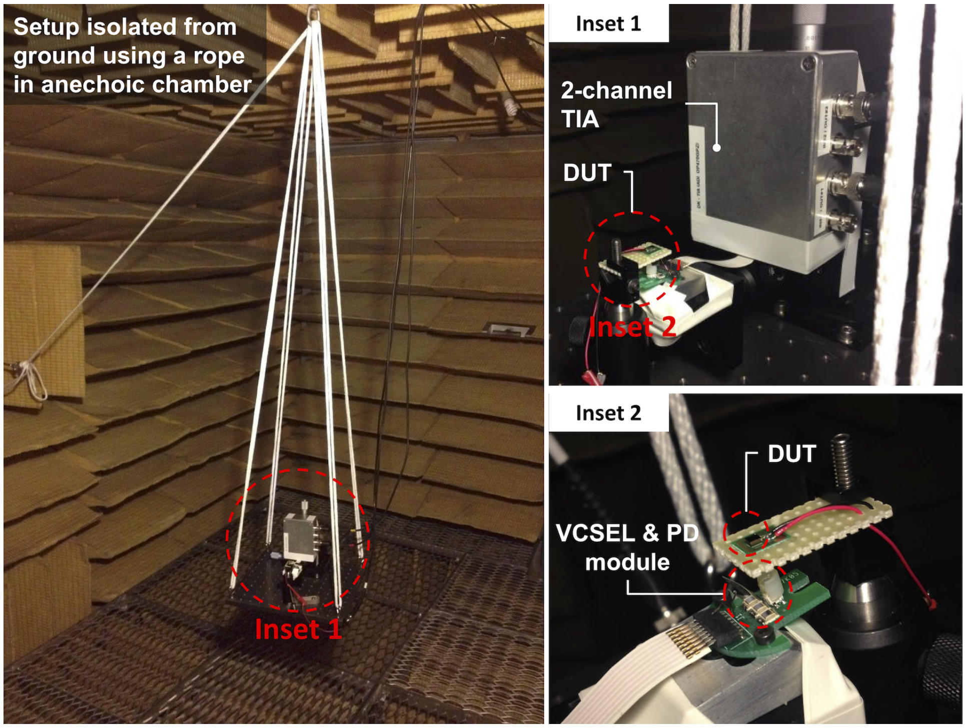

Figure 4.3: Anechoic chamber testing setup.

The photodiodes (PDs) on the optoelectronics module were connected to a trans-impedance amplifier (TIA) using a flexible flat cable as shown in Inset 2 on 4.3. The TIA was built with Analog Devices, Inc. OP470GPZ quad operational amplifier (op amp). A feedback resistor $R_f = 50$ kΩ with $C_f = 12$ pF in parallel is used for both channels, and the theoretical cut-off frequency of the feedback loop is above 265 kHz, which is sufficient for the targeted measurement frequency range, up to 96 kHz. The 0th-order and the summed ±1st-order photocurrents are fed into each channel of the TIA, and the output signals from the TIA were recorded by PrismSound dScope Series III audio analyzer. To isolate ambient noise, all the measurements were performed in the anechoic chamber (10×10×10 ft^3) at The University of Texas at Austin.

4.4 Modulation Efficiency and Sensitivity Measurement

The 0th and ±1st-order diffracted light intensities were observed with an oscilloscope while the diaphragm is being actuated electrostatically until the maximum ME is achieved, i.e., the best MDD. A function generator (HP 33120A) and a high-voltage amplifier (A.A. LAB SYSTEMS A-301) were used to generate a triangular voltage signal varying from 0 V to 25 V for electrostatic actuation. Photocurrents, i_0 and $i_{\pm 1}$ from 0th-order and ±1st-order PDs can be obtained by IR_{PD}, where I is light power falling onto each PD, and R_{PD} is the responsivity (A/W) of the PD used for the setup (Advanced Photonix, Inc. PDB-C154SM). The responsivity of the PDB-C154SM is specified as 0.5 A/W. The output photocurrents are converted to voltage outputs through the 2-channel TIA as described in Figure 2.11.

The modulation curves presented in Figure 4.4 was obtained by recording TIA output voltages corresponding to 0-to-25V triangular electrostatic actuation input using Tektronix TDS 3014 digital phosphor oscilloscope. The frequency and peak-to-peak voltage of the input triangular signal were 100 Hz and 0-to-25 V respectively. The measured MEs of the system are 72% and 79% for 0th-order and ±1st-order PDs respectively. For the 0th-order PD, the displacement sensitivity S_{PD} is measured as 0.0203 V/nm. As discussed before, the shot noise of the PD defines the MDD of the given system. The

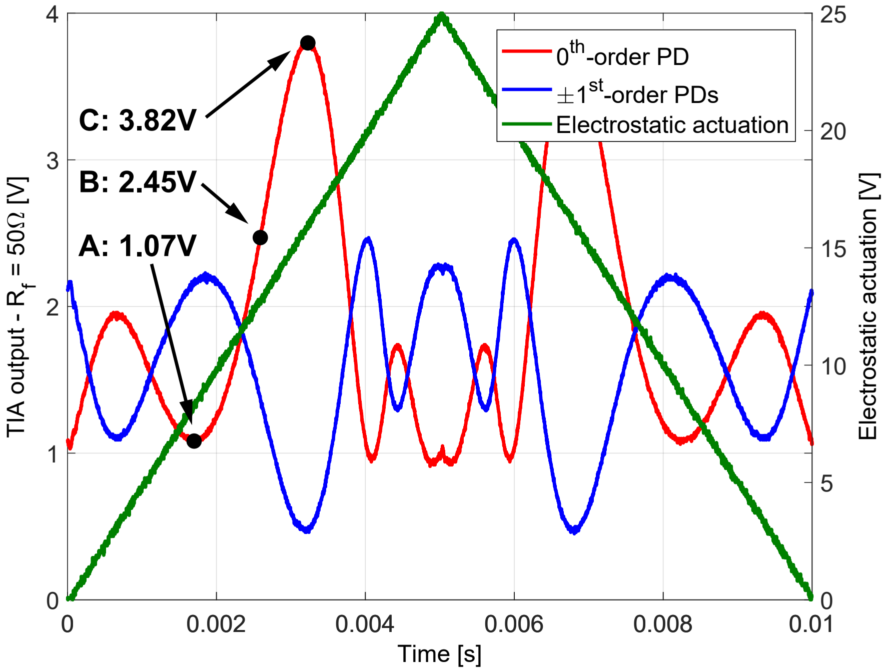

Figure 4.4: Optical modulation test with 25-V triangular signal at 100 Hz.

voltage level of the TIA output due to the shot noise i_{shot} can be defined by,

$$V_{shot} = -R_f i_{shot} \tag{4.1}$$

From the 0th-order beam, the computed shot noise V_{shot} is 130.93 nV/$\sqrt{\text{Hz}}$, and the MDD of the prototype therefore is computed as 6.44 fm/$\sqrt{\text{Hz}}$. Note that MDD can be converted to the input pressure-referred noise spectral density in units of Pa/$\sqrt{\text{Hz}}$ with the diaphragm compliance C_{mp} [m/Pa], and eventually A-weighted noise (dBA) over a specific frequency range (typically from 20 Hz to 20 kHz).

4.5 Electrostatic Actuation Measurement

To measure the device resonance frequency and the quality factor (Q), a frequency response measurement was performed with electrostatic actuation while the diaphragm motion was monitored via the optoelectronics. To maximize the detection resolution, the DC bias voltage was tuned to the most sensitive position (most steep slope on the optical curve), and the diaphragm was actuated with a small-amplitude white-noise like AC signal (bin-center) from PrismSound dScope Series III fast-Fourier transform (FFT) acoustic spectrum analyzer.

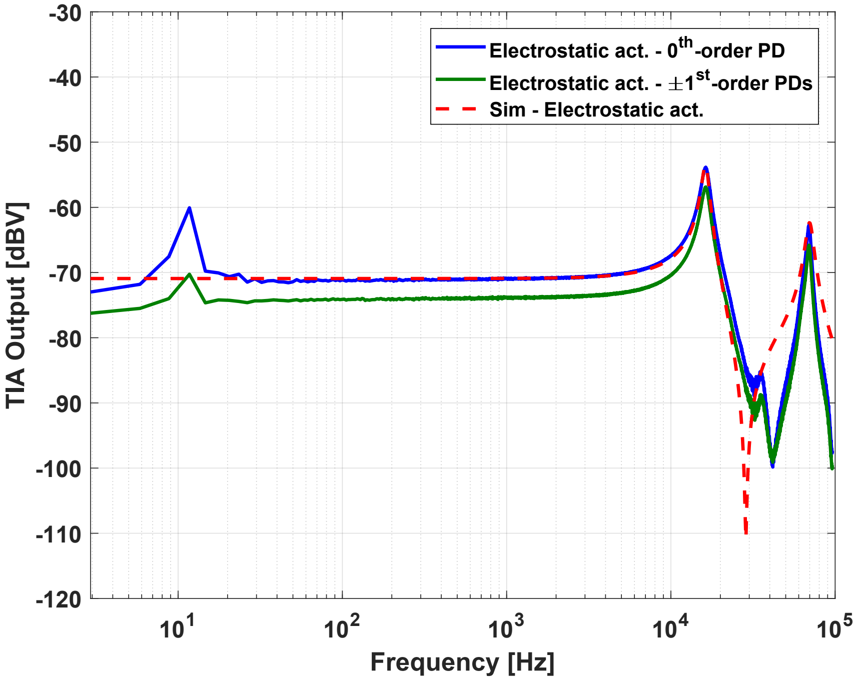

Figure 4.5: Frequency response of the diaphragm-backplate structure using electrostatic actuation.

From the frequency response measurement with electrostatic actuation, two distinct resonance peaks were observed at approx. 16.3 kHz and 70 kHz as shown in Figure 4.5. Compared to the FEA result, the first peak represents the fundamental resonance of the diaphragm, and the second peak at 70 kHz is due to the backplate resonance. To extract the compliance of the diaphragm from the diaphragm resonance frequency, the effective mass of the diaphragm m_{eff} is required. To compute m_{eff}, the modal analysis of the Si diaphragm is used to compute the modal mass in the vertical direction. From the ratio of the modal mass to the actual Si-diaphragm mass, the actual effective mass of the diaphragm was computed. The actual mass of the diaphragm includes not only the Si membrane mass but also the amount of Au layer deposited on to the diaphragm to improve optical reflection (approximately 100 nm). Finally, the diaphragm compliance C_m or C_{mp}, is estimated as 0.1175 m/N or 30.71 nm/Pa respectively.

Based on the modeling fitting using the measured and extracted model parameters as presented in Tables 4.1 and 4.2, the major damping mechanism of the prototype structure is the flow resistance at the grating region as expected. Although the honeycomb-shaped perforations provide much lower flow resistance than commercial capacitive-type MEMS microphones, the backplate design has room for improvement to reduce the flow resistance.

Table 4.1: Measured model parameters from the frequency response measurement with electrostatic actuation.

Variable	Description	Value
f_d	Diaphragm resonance frequency	16.3 kHz
Q_d	Diaphragm quality factor	17.90
f_{bp}	Backplate resonance frequency	70.0 kHz
Q_{bp}	Backplate quality factor	10.72

Table 4.2: Extracted model parameters.

Variable	Description	Value
m_d	Diaphragm effective mass	0.81×10^{-9} kg
C_d	Diaphragm compliance	0.1175 m/N
m_{bp}	Backplate effective mass	0.11×10^{-9} kg
C_{bp}	Backplate compliance	0.0470 m/N
R_m	Flow resistance due to grating	4.6325×10^{-6} N·s/m

4.6 Thermal-mechanical Noise Measurement

Prior to the prototype noise measurement, the component-wise noise floor was measured to compare to the corresponding individual noise model. In this prototype testing, no protective lid was attached, and therefore the package-related noises sources were not included in this analysis. The noise floor of the electronics was measured to ensure that it can resolve the thermal-mechanical noise of the prototype. To isolate the TIA noise floor from the RIN, the VCSEL was turned off, and the voltage output through the TIA was measured in the dark chamber. The amplifier output noise is due to the combination of Johnson-Nyquist noise of the feedback resistor, computed as $V_{no,R_f} = \sqrt{4k_bTR_f} = 28.7$ nV/$\sqrt{\text{Hz}}$, and internal current noise of the op amp, computed as $V_{no,i_{n-}} = i_{n-}R_f = 35$ nV/$\sqrt{\text{Hz}}$ for the Analog Devices, Inc. OP470GPZ op amp used with specd current noise of $i_{n-} = 0.7$ pA/$\sqrt{\text{Hz}}$. The incoherent summation of these two voltage-noise spectral densities, 45.26 nV/$\sqrt{\text{Hz}}$, produces the simulated trace shown in Figure 4.6.

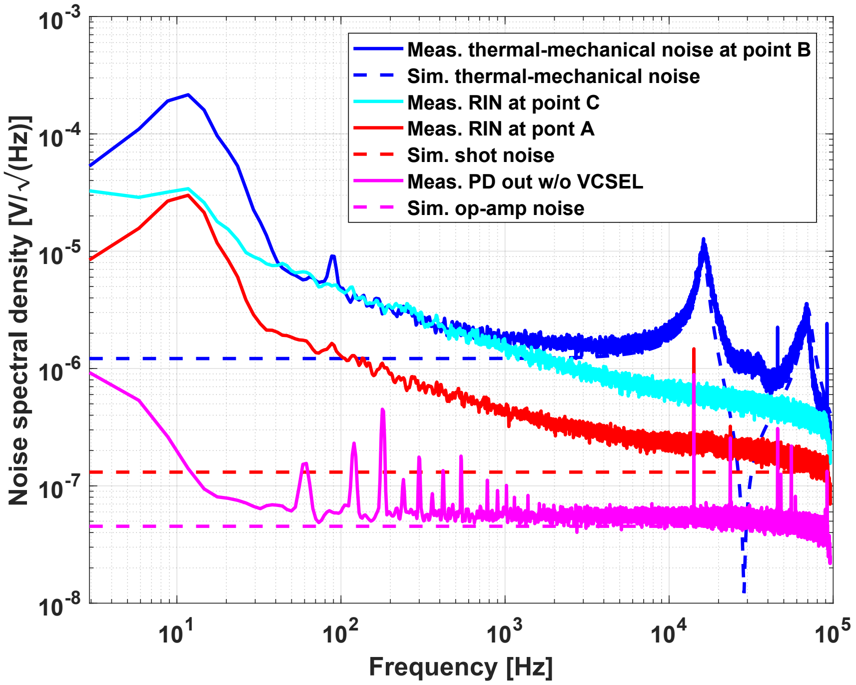

Figure 4.6: Measured and simulated noise spectral density spectra.

Since the measured diaphragm-backplate structure is not fully packaged, the equivalent circuit model in Figure 2.1 is simplified to the one in Figure 4.7. The simplified equivalent circuit model was used to simulate the thermal-mechanical noise of the prototype with the measured and extracted system parameters listed in Tables 4.1 and 4.2.

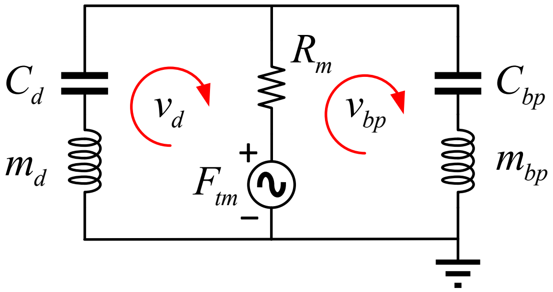

Figure 4.7: Simplified equivalent circuit model of the prototype.

The simulated noise level and the actual device noise floor are in close agreement as shown in Figure 4.6. As discussed in Chapter 3, the backplate is not perfectly rigid, and thus the effect of the compliant backplate is included to simulate the noise floor.

$$d_{tm} = F_{tm}(C_d + C_{bp}) \tag{4.2}$$

The resultant thermal-mechanical displacement is approximately at the flat response region, which is approximately 20-dB higher than the measured MDD (6.44 fm/$\sqrt{\text{Hz}}$). Therefore, it is confirmed that the measured noise floor is thermal-mechanical displacement limited. The extracted model parameters also indicate that (i.e., 40% of the diaphragm compliance), and, in consequence, the backplate compliance induces 1.4× higher thermal-mechanical noise than the case of a completely rigid backplate. In other words, additional 3-dB higher noise is generated due to the compliant backplate. The backplate compliance should be less than 6% of in order to avoid the noise penalty due to the compliant backplate less than 0.5 dB.

In the thermal-mechanical noise measurement, the measured noise spectral density is about 24 dBA while the simulated thermal-mechanical noise of the prototype based on the values from Tables 4.1 and 4.2 is about 21 dBA. The 3-dB discrepancy can be explained by the RIN measurement. The RIN effect is easily observable at the frequency range from DC to 4 kHz. To verify the RIN, the DC bias voltage applied to the diaphragm and backplate was changed to the values where the device sensitivity becomes zero, i.e., A and C in Figure 4.4. At the zero-sensitivity points, the optical detection cannot resolve any diaphragm motion, and thus it can only detect the RIN presented in the system. By comparing to the simulated shot noise levels, the RIN measurements show the evidence that RIN noise is dominating below 10 kHz.

4.7 Relative-intensity Noise Cancellation

In the noise measurement, the measured thermal-mechanical noise was higher than that the simulation predicted (21 dBA and 24.79 dBA for simulated and measured data respectively), and the discrepancy is induced by the RIN from the VCSEL. To suppress the RIN, the differential readout scheme was used as shown in Figure 4.8.

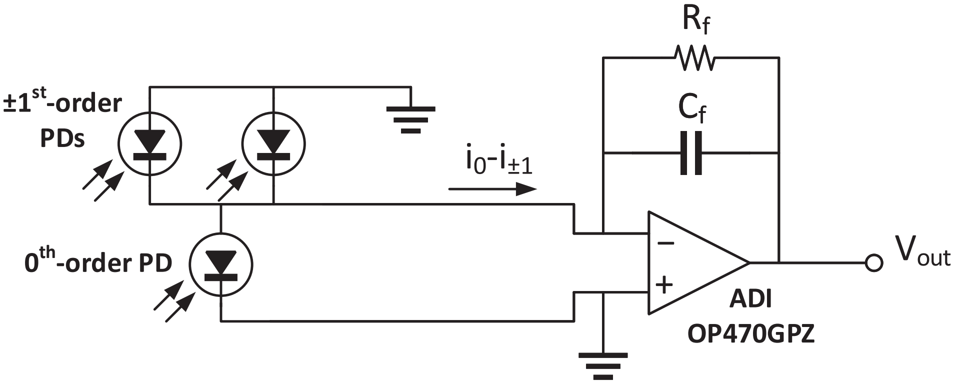

Figure 4.8: TIA circuit diagram for a differential readout of PDs to achieve RIN cancellation.

In this setup, the differential output $(i_0 - i_{\pm1})$ cancels the common-mode RIN presented on PD arrays as discussed before. The differential operation was done in photodiode level to prevent inducing any additional phase of the signals through the signal amplification stage, which lowers the effectiveness of the RIN cancellation. In theory, the RIN can be eliminated completely, if the 0th-order and ±1st-order PDs accept the same amount of light intensity (i.e., a perfectly aligned optics). The ideal condition is not easily achievable so that RIN cancellation performance is generally lower than the theoretical estimation in actual cases.

The thermal-mechanical noise spectral density was measured again with the differential-readout scheme, and the result shows the differential readout suppressing RIN down to 100 Hz as shown in Figure 4.9. At 1 kHz, the simulation suggests the system noise level as 21.02-dB A-weighted (dBA), while the actual measurement results show 24.13 dBA and 22.61 dBA without and with the RIN cancellation respectively.

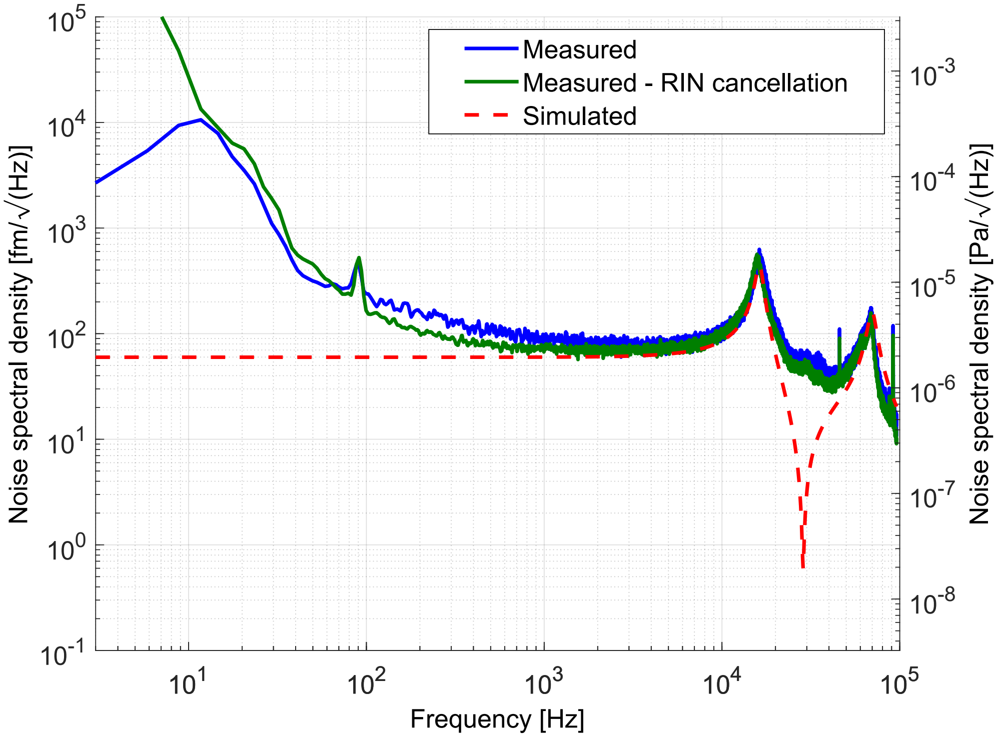

Figure 4.9: Noise spectral density comparison with / without RIN cancellation.

4.8 Noise Spectral Density and Frequency Response Measurement of the Prototype Optical Microphone Compared Against Commercial MEMS Microphones

In this section, noise-floor and frequency-response measurements are performed to compare the prototype optical microphone to the state-of-the-art capacitive MEMS microphones.

4.8.1 Interface Circuit for Analog Capacitive MEMS Microphone

Five commercial MEMS microphones were prepped for the measurements. A twisted pair of wires were attached to each surface-mount-type MEMS microphone as shown in Figure 4.10.

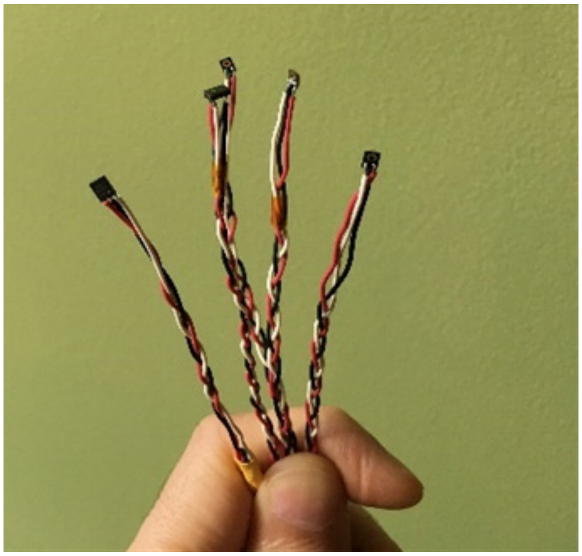

Figure 4.10: Tested commercial MEMS microphones.

The attached wires were connected to an interface box was built based on the application note by MEMS microphone manufacturers as shown in Figure 4.11.

Note that the C1 large capacitor at the analog output in Figure 4.11 to eliminate DC offset present in output signal due to the dc bias voltage applied across the diaphragm and backplate. A proper value of the decoupling capacitor must be selected not to disrupt the designed low cut-off frequency of the microphone. The combination of the C1 and the input impedance R, of

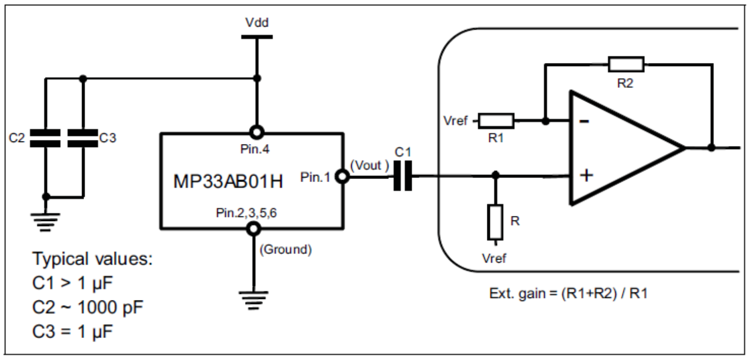

Figure 4.11: A schematic of electrical connections for a capacitive MEMS microphone. The interface box utilizes a large DC decoupling capacitance (C1) to remove a DC component from the microphone output [21].

the following amplifier or analyzer in Figure 4.11 can add a pole at a frequency higher than the low cut-off frequency. In this case, the specified low cut-off frequency cannot be observed.

4.8.2 Calibration Procedure for Noise and Frequency Response Measurements

A reference microphone, G.R.A.S. 40AF 1/2″ free-field microphone, is used to verify a noise floor inside a Brüel & Kjær Type 4232 test box prior to the subsequent noise measurements. Prior to the noise-floor verification, the sensitivity of the G.R.A.S. 40AF reference microphone was calibrated with a G.R.A.S. 42AB sound calibrator, which generates a calibrated 114-dB (i.e., 10 Pa) SPL at 1 kHz. The output signal under the 114-dB SPL input, is used to calculate a sensitivity in units of output voltage per unit pressure (i.e., 1 Pa or 94-dB SPL), which is calibrated as 43.8 mV/Pa. The G.R.A.S. 40AF has a thermal-mechanical noise of 14-dBA thermal noise over 20 kHz, while the noise floor of the anechoic test box was measured as 15.7 dBA.

The sensitivity of each MEMS microphone was verified inside the anechoic box with a 74-dBSPL signal at 1 kHz, which is regulated with the G.R.A.S. 40AF reference microphone. In each test, the tested MEMS microphone was placed near the reference microphone to measure the sensitivity without any acoustic diffraction effects, which can lead to an erroneous measurement result.

4.8.3 Discussion of Frequency Response Measurement Results

Figure 4.12 shows the normalized frequency responses of the DUTs with respect to the response measured with the G.R.A.S. 40AF reference microphone. Note that the 24 dB/octave attenuation above 10 kHz in the anechoic box leads to the frequency responses above 10 kHz are not meaningful. However, the low cut-off frequency of each DUT is clearly observable from the normalized frequency response. The low cut-off frequency of the prototype optical microphone is measured as 75 Hz. The measured low cut-off frequency is used for the noise model in the next section. ST Microelectronics MP33AB01H and MP23AB02B show the lowest and highest low cut-off frequencies respectively. With a consideration of package sizes of the tested microphones (i.e., back-cavity compliance), The MP33AB01H is expected to have a higher vent resistance.

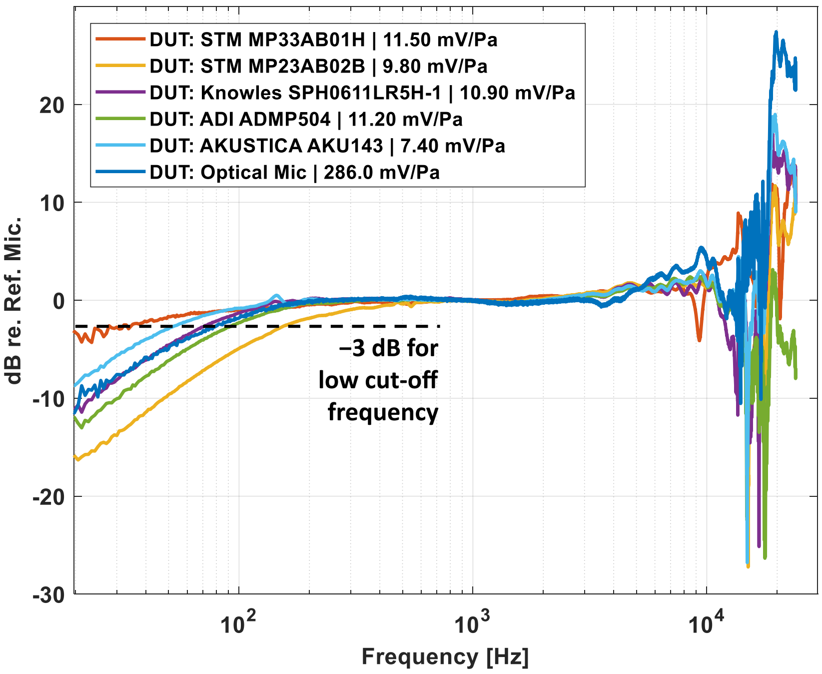

Figure 4.12: Frequency response plot of commercial MEMS microphones, normalized to G.R.A.S. 40AF 1/2″ free-field microphone.

4.8.4 Discussion of Noise Floor Measurement Results

The results of the sensitivity and A-weighted noise measurements in terms of SNR are summarized in Table 4.3. Figure 4.13 shows noise density spectra of DUTs including the G.R.A.S. 40AF reference microphone, which represents the absolute noise floor inside B&K 4232 anechoic test box. Noise density spectra presented in Figure 4.13 show raw input pressure-referred noise, i.e., minimal detectable pressure (MDP) without A-weighting filter applied. A-weighting filter is applied to the measured raw noise spectra from 20 Hz to 22 kHz (a brick-wall filter is used), as most commercial MEMS microphones specifies noise floor over the frequency range.

Table 4.3: Summary of the measurements with the prototype optical microphone and commercial MEMS microphones.

Manufacturer	Model	Typical sensitivity (dBA/Pa)	Measured sensitivity (dBA/Pa)	Typical SNR (dBA)	Measured SNR (dB)
N.A.	Prototype Optical Mic	-	-12.00	-	72.00
ST Microelectronics	MP33AB01H	-38	-38.79	66	65.49
ST Microelectronics	MP23AB02B	-38	-40.18	64	63.36
Knowles	SPH0611LR5H-1	-38	-39.25	65	64.75
Akustica	AKU143	-42	-42.62	65	58.84
Analog Devices	ADMP504	-38	-39.02	65	64.64

It was observed that the resonance of each tested microphone is located slightly above 22 kHz, as shown in Figure 4.13. This appears to be a strategical design to achieve the maximum system compliance for the highest sensitivity, whereas the resonance peak is not located within the target frequency range so that it does not increase A-weighted noise significantly. The optical microphone shows a significantly lower noise floor compared to the commercial MEMS microphones owing to the low flow resistance of the minimalistic backplate design. The measured noise floor of the prototype optical microphone was verified with the lumped parameter model presented in Chapter 2. Table 4.4 shows the key model parameters used for the simulated noise floor shown in Figure 4.14.

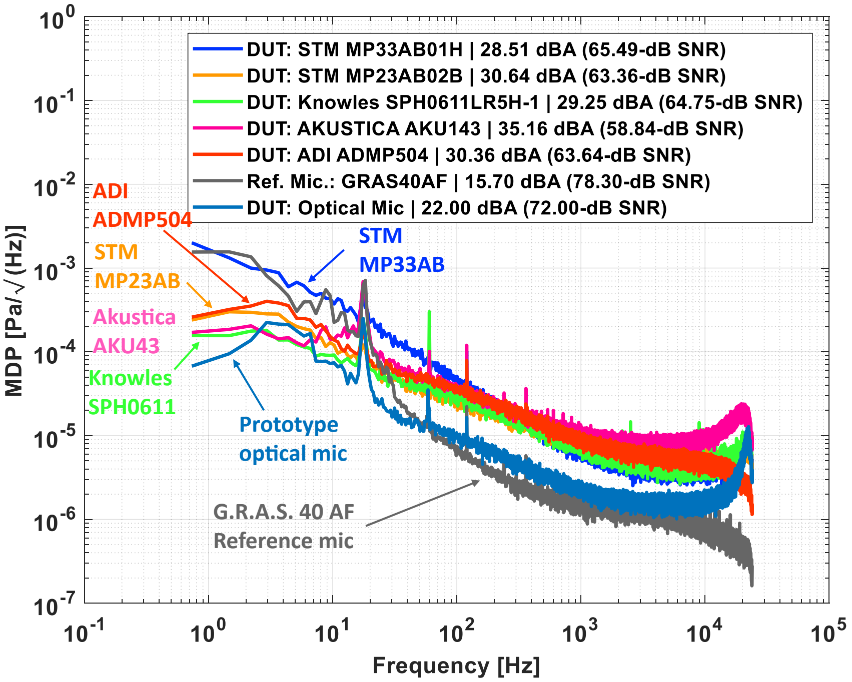

Figure 4.13: A comparison of commercial capacitive MEMS microphones. G.R.A.S. 40AF 1/2″ free-field reference microphone is used to verify the ambient noise level to ensure valid noise floor measurements with the MEMS microphones.

Table 4.4: Key parameters used to simulate the prototype optical microphone shown in Figure 4.14.

f_{cut} (Hz)	d_{dp} (mm)	C_{mp} (nm/Pa)	d_{grat} (μm)	N$_{spoke}$	V_{MEMS} (m^3)	V_{LID} (m^3)	V_{ASIC} (m^3)	V_{OPTO} (m^3)	MDD (fm/Hz)
75	1.5	10	154	16	1.9845	5.0	2.3710	2.4033	12

Table 4.5 shows the component-wise A-weighted noises simulated using the

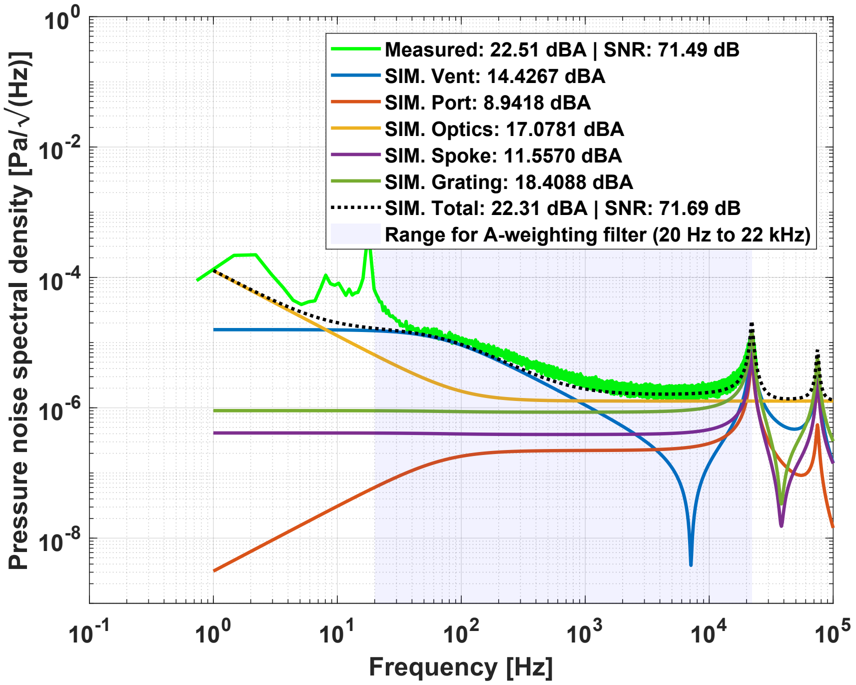

Figure 4.14: Simulated noise spectra of the prototype optical microphone. The measured noise floor is superimposed.

parameters in Table 4.4. The lumped parameter model predicted the overall noise floor as 22.51 dBA from 20 Hz to 22 kHz, which is within -0.2-dB difference compared to the measured noise floor.

Table 4.5: Simulated A-weighted noise due to noise sources, and a comparison between simulated and measured A-weighted noise.

Vent (dBA)	Port (dBA)	Optics (dBA)	Spoke (dBA)	Grating (dBA)	Total simulated (dBA)	Total measured (dBA)	Difference (dB)
11.43	8.94	17.08	11.56	18.41	22.51	22.31	-0.20

The simulated component-wise noise floor spectra reveal that the most significant noise contribution is from the grating (40.7%), followed by the optics noise (30.0%), i.e., shot-noise, or high MDD. Although the optics noise is higher from 1 kHz to 10 kHz range, the grating-induced noise has much higher influence due to the fact that the part of the system resonance is included in the 20-Hz-to-20-kHz frequency range. While the prototype optical microphone has 6-dB better SNR compared to tested commercial MEMS microphones, a further improvement on the grating design and optics would increase the optical microphone SNR even further than as-is.

4.9 Summary

In this chapter, the diaphragm-backplate structure was built and tested. The extracted system parameters were used to compare the model to the measured noise spectra. Finally, a prototype optical microphone and five state-of-the-art MEMS microphones were tested. The prototype optical microphone shows a 6-dB better SNR compared to commercially-available capacitive MEMS microphones. The lumped-parameter network model of the prototype optical microphone successfully predicts the measured noise floor within 0.2-dB difference. The simulated component-wise noise contribution on the prototype suggests that the SNR would be improved further if a lower MDD than the measured 12 fm/$\sqrt{\mathrm{Hz}}$ is achieved. The noise density spectra of commercial MEMS microphones are similar to each other across the audible frequency range, which suggests that each manufacturer struggles with the fundamental limit of the capacitive-based MEMS microphone design.

The design of experiments (DoE) for an optical microphone using the verified optical microphone noise model is presented in the next chapter. In the DoE, system parameters including diaphragm compliance, low cut-off frequency, back-cavity volume, etc., are perturbed to show individual parameter effect on SNR and AOP, in which design implications will be discussed to achieve sub 15-dBA noise floor.

Chapter 5

Design of Experiments for Optical Microphone with Sub 15-dBA Noise Floor

5.1 Overview

Optical microphone consists of multiple components across the mechanical, electrical and acoustical domains as presented in Figure 5.1. As a result, the effect due to changes on system parameters is often not intuitive for a fully-packaged MEMS microphone.

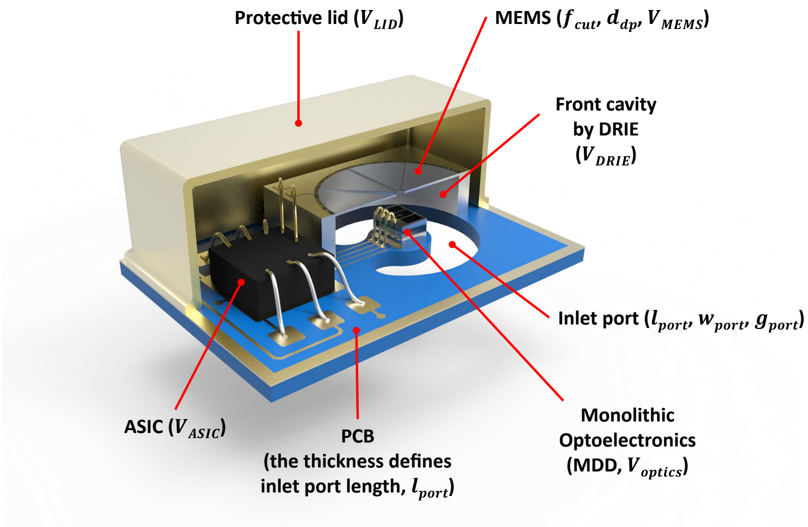

Figure 5.1: A cross-sectional view of a 3-D rendered optical microphone with a monolithic optoelectronics module, with key parameters described in Table 5.1.

In this chapter, the design of experiments (DoE) approach is utilized to study the impact of system parameters on the microphone SNR and the acoustic overload point (AOP). In the following sections, fixed system parameters for the subsequent DoE are explained, followed by a detailed discussion of the various set of DoE.

5.1.1 System Parameters used for DoE

Table 5.1 summarizes the key parameters used in the optical-microphone DoE. The listed values are used unless stated otherwise.

Table 5.1: System parameters and values used in the following DoE. Some parameters are perturbed to show their effect on SNR and AOP.

Variable	Description	Value
f_{cut}	Low cut-off frequency	5 kHz
d_{dp}	Diaphragm diameter	1 mm
MDD	Minimum detectable displacement	2.707 $\mathrm{fm}/\sqrt{\mathrm{Hz}}$
V_{MEMS}	Volume - MEMS die	0.432 mm^3 ($1.2\times1.2\times0.3$ mm^3)
V_{ASIC}	Volume - ASIC	0.05 mm^3 ($0.5\times0.5\times0.2$ mm^3)
V_{LID}	Volume - Lid (internal)	32.00 mm^3 ($4\times4\times2$ mm^3)
V_{bc}	Volume - Back cavity $V_{LID} - (V_{MEMS} + V_{ASIC})$	31.52 mm^3
V_{optics}	Volume - Optoelectronics	9.315×10^{-3} mm^3
V_{DRIE}	Volume - DRIE cavity volume on MEMS die	2.356×10^{-1} mm^3
V_{fc}	Volume - Front cavity $V_{DRIE} - V_{optics}$	2.263×10^{-1} mm^3
l_{port}	Inlet port length (PCB thickness)	0.1 mm
w_{port}	Inlet port width (longitudinal)	1.76 mm
t_{port}	Inlet port gap	0.3 mm

Table 5.2 presents acoustic mass, compliance, and resistance values using the packaging parameters from Table 5.1.

Table 5.2: Computed acoustic parameters used in DoE#1 to #7.

Acoustic parameter	Equation	Value
Inlet-port mass m_{aport}	$m_{aport} = \frac{\rho(l_{port}+1.7(t_{port}/2))}{w_{port}t_{port}+\pi t_{port}^2/4}$	$7.1156\times10^{+2}$ kg/m^4
Inlet-port resistance R_{aport}	$R_{aport} = \frac{12\nu l_{port}}{t_{port}^3 w_{port}}$	$4.6970\times10^{+5}$ Pa·s/m^3
Front-cavity compliance C_{afc}	$C_{afc} = \frac{V_{fc}}{\rho c^2}$	1.6314×10^{-15} m^3/Pa
Back-cavity compliance C_{abc}	$C_{abc} = \frac{V_{bc}}{\rho c^2}$	1.0943×10^{-14} m^3/Pa
Vent resistance R_{avent}	$R_{avent} = \frac{1}{2\pi f_{cut} C_{abc}}$	$1.4010\times10^{+11}$ Pa·s/m^3

5.2 Backplate Flow Resistance for DoE

The backplate design used in the following DoE is illustrated in Figure 5.2. A Michelson-type grating is located at the center, which is supported by multiple spokes. The backplate diameter d_{bp} is the same as the diaphragm diameter d_{dp}. The length of each spoke l_{bp} is determined by $(d_{bp} - d_{dp})/2$, and the number of spokes N_{sp} is set to 8 in this study.

To determine a grating flow resistance for the DoE, a smallest realizable grating diameter d_{grat} is considered, which is governed by the laser spot size on the grating surface. For example, a VCSEL with 17° beam divergence forms a 68.75-μm diameter laser spot on the grating surface, assuming 230-μm

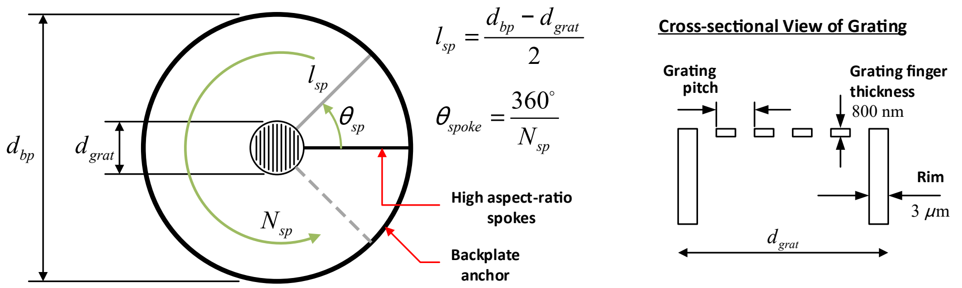

Figure 5.2: Illustration of the minimalistic backplate design used in the DoE.

away from the VCSEL aperture. If assuming 25 μm for a typical pick-and-place machine tolerance, approximately 100-μm diameter grating would be the smallest acceptable diameter. The most accurate pick-and-place machine on the market is capable of achieving 5-8 μm tolerance with a 3-sec placing time, and therefore 74-μm diameter grating is chosen in this study, coinciding with the most aggressive design that can be pursued.

The inset in Figure 5.2 shows the grating cross sectional view. The 74-μm-diameter grating design has a 3-μm-wide outer rim and grating finger thickness (800 nm). The rim thickness is matched to the spoke width, and the grating finger thickness is chosen based on the 2-D grating simulation in Chapter 2. While the grating pitch remains 4 μm, three different finger widths (1.5, 1.75 and 2 μm) are simulated to study flow resistance. Figure 5.3 shows the contour plots of induced pressure on the diaphragm and grating surface due to viscous air flow using ANSYS FLUENT. In the figure, the contour in red represent where the highest flow resistance occurs, and the grating rim area shows a high flow resistance as expected due to the flat surface normal to the air flow.

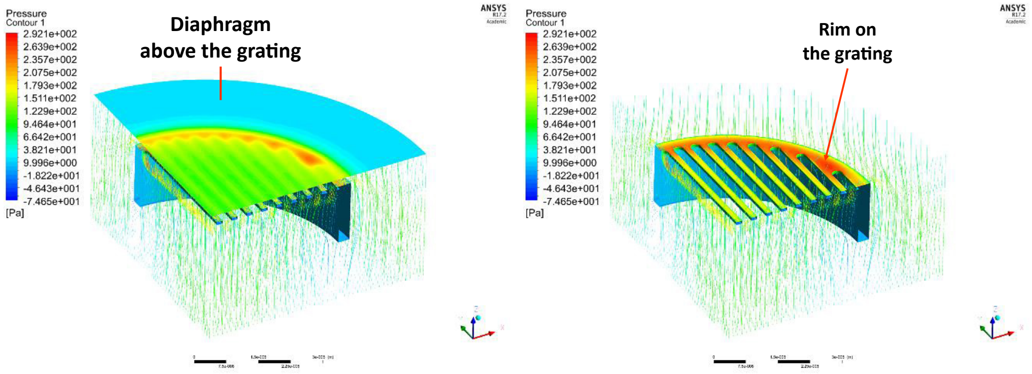

(a) (b)

Figure 5.3: Grating flow resistance simulation for a quadrant model (74-μm diameter grating). The flow resistance is obtained by taking surface integral of the generated pressure on the diaphragm due to the viscous air flow.

Table 5.3: Computed flow resistances from a 74-μm-diameter grating with three different finger widths using ANSYS FLUENT.

Description	R_m (N·s/m)
2.0-μm wide finger	1.0282×10^{-6}
1.75-μm wide finger	9.2347×10^{-7}
1.50-μm wide finger	7.0216×10^{-7}

Table 5.3 shows the summary of the simulated flow resistances for the three different grating cases. The narrowest grating-finger case (1.5-μm-wide) shows the smallest flow resistance, and the corresponding simulated flow resistance $R_m = 7.02\times10^{-7}$ N·s/m is used in the subsequent DoE. Using the same procedure, the flow resistance for 3-μm-wide spoke per unit length is simulated

as 6.7551×10^{-4} N·s/m per m.

5.2.1 Acoustic Overload Point

An important performance parameter of a microphone is dynamic range (DR) or acoustic overload point (AOP). This specification is important when the microphone is expected to measure a relatively high sound pressure level, e.g., recording at a loud concert or measuring jet-engine noise. The AOP is defined by a sound pressure level (SPL) causing 10% total harmonic distortion (THD). Figure 5.4 illustrates the relations among A-weighted noise, SNR, DR, and AOP.

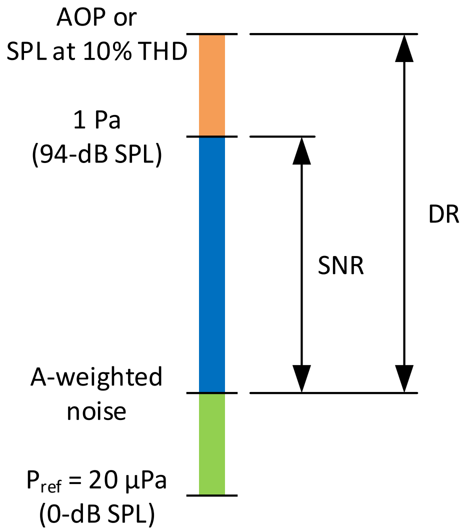

Figure 5.4: Illustration of the relations between A-weighted noise, SNR, and DR.

The THD(%) for a given input SPL is computed by comparing the incoherent sum of the harmonics to the fundamental peak amplitude from the

FFT of the DUT output as shown in (5.1).

$$\mathrm{THD}(\%\ ) = \frac{\sqrt{A_2^2 + A_3^2 + \cdots + A_n^2}}{A_1} \times 100 \tag{5.1}$$

where, A_n represents the n-th RMS amplitude of harmonics on the FFT. THD% at 1-Pa input (94-dB SPL) and SPL values at THD 1%, 3% and 10% are typically listed as microphone specs. For THD% for an optical microphone, light intensities of 0th and ±1st order diffraction patterns due to diaphragm motion is relevant. From [26], the differential output current from 0th and ±1st order is,

$$i_{out} = i_0 + i_{\pm 1} \propto IR \sin\left(\frac{4\pi}{\lambda}\Delta z\right) \tag{5.2}$$

where, I is the incident laser intensity [W], and R is the responsivity of the photodiode [A/W]. For a generalized THD analysis with respect to the light wavelength λ, the input displacement Δz is normalized to Δz_{max}, which is fundamentally determined by the wavelength of the light source.

$$\Delta z_{norm} = \frac{\Delta z}{\Delta z_{\max}} \tag{5.3}$$

where, $\Delta z_{max} = \lambda/8$. When substituting (5.3) into (5.2), the output signal follows the following relationship,

$$i_{out} \propto \sin\left(\frac{\pi}{2}\Delta z_{norm}\right) \tag{5.4}$$

where, $0 \leq \Delta z_{norm} \leq 1$. Fast Fourier transform (FFT) is taken on (5.4) to obtain harmonics, followed by the THD% calculation by (5.1).

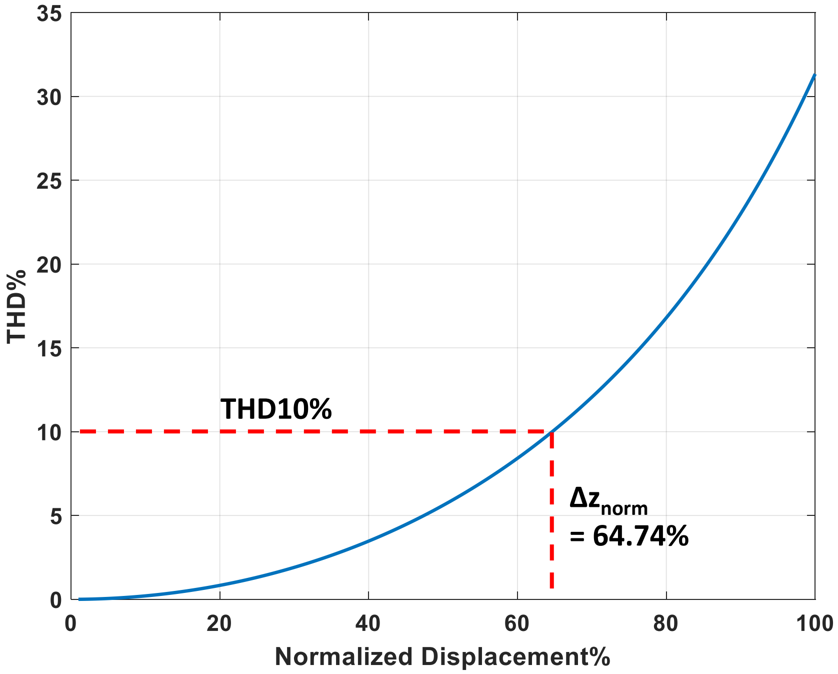

Figure 5.5: THD% vs. normalized diaphragm displacement with respect to Δz_{max}.

Figure 5.5 shows simulated THD% over 0 to 100% of the normalized diaphragm displacement. When the diaphragm is deformed as much as 9.41% of Δz_{max}, the corresponding THD% becomes 0.18%, and THD 10% occurs when the diaphragm deforms up to 64.74% of Δz_{max} as illustrated in Figure 5.6 For a laser with a wavelength $\lambda = 850$ nm, THD 10% occurs when diaphragm deflects 68.8 nm RMS. The resultant AOP with an integrated microphone compliance $C_{mp,int}$ in units of m/Pa is therefore calculated by,

$$\text{AOP} = 0.6474 \left(\frac{\lambda}{8}\right)\left(\frac{1}{C_{mp,int}}\right) \tag{5.5}$$

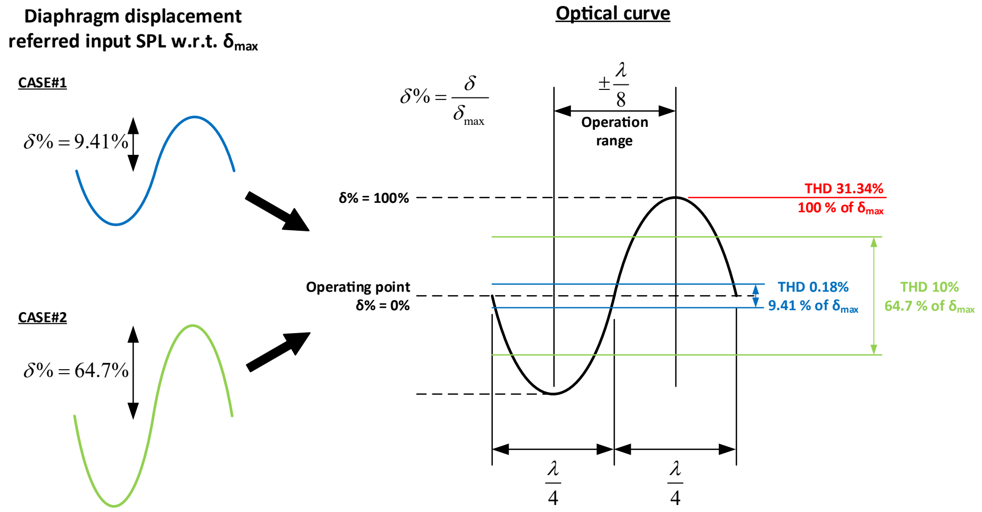

Figure 5.6: Illustration of the distortion of the optical microphone, in which the intrinsic DR is determined by the wavelength of the used VCSEL.

5.2.2 Electrical Power vs. MDD

The sensitivity of the interferometric-based displacement detection system and MDD are described in Chapter 2. From the discussion, the SNR of the displacement sensitive detection system scales with $\sqrt{I}$ where I is the light power. Electrical power is limited in consumer electronics applications. Table 5.4 shows MDD values with four different electrical power budgets. A 25% wall-plug efficiency for VCSEL, 0.4 A/W responsivity for PD and 100% ME is assumed. Typical high-performance capacitive MEMS microphones consume up to 500-μW electrical power (e.g., ST Microelectronics MP33AB01H analog capacitive MEMS microphone with 66-dB SNR). Table 5.4 shows the MDD-limited noise floor assuming no other components contribute to the noise level. For example, the lowest achievable A-weighted noise with 1.2-mW electrical power is 8.82 dBA, i.e., 85.18-dB SNR. It becomes clear that 0.04-mW electrical power cannot achieve a sub 15-dBA noise floor.

Table 5.4: Simulated MDD vs. electrical power assuming 100% ME.

Electrical power (mW)	Light power (mW)	Shot noise $A/\sqrt{Hz}$	Displacement sensitivity (A/m)	MDD $(fm/\sqrt{Hz})$	MDD limited dBA (assuming 10 nm/Pa)
4	1	8.01×10^{-12}	$2.96\times10^{+3}$	2.71	3.59 (90.41-dB SNR)
1.2	0.3	4.38×10^{-12}	$8.87\times10^{+2}$	4.94	8.82 (85.18-dB SNR)
0.4	0.1	2.53×10^{-12}	$2.96\times10^{+2}$	8.56	13.59 (80.41-dB SNR)
0.04	0.01	8.01×10^{-13}	$2.96\times10^{+1}$	27.1	23.59 (70.41-dB SNR)

5.3 Design of Experiments - Large Microphone Case

DoE#1 to #7 investigate diaphragm compliance impact on SNR and AOP. For DoE#1 to #7, it is assumed that the power budget and the microphone package size are not limited. Therefore, the lowest MDD (2.71 $fm/\sqrt{Hz}$) in Table 5.4 is used in the DoE (requiring the highest electrical power). The back-cavity volume for DoE#1 to #7 is set to 31.52 mm^3, which results in 10× higher acoustic compliance even compared to the acoustic compliance of the most compliant diaphragm (60 nm/Pa). The rest of the system parameters are identical as presented in Table 5.1. The simulated component-wise noises are presented in Table 5.5.

Table 5.5: Component-wise noise for DoE#1 to #7.

DoE #	C_{mp} (nm/Pa)	$C_{mp,int}$ (nm/Pa)	Vent noise (dBA)	Port noise (dBA)	Optics noise (dBA)	Spoke noise (dBA)	Grating noise (dBA)	Total noise (dBA)	AOP (dBSPL)
1	60	54.5	-3.884	2.640	-11.108	17.923	20.618	22.543	95.99
2	40	37.5	-4.323	-3.574	-7.862	11.807	14.501	16.466	99.24
3	20	19.4	-4.387	-5.366	-2.127	10.058	12.753	14.808	104.99
4	10	9.84	-4.404	-5.807	3.747	9.625	12.319	14.658	110.86
5	5	4.96	-4.412	-5.990	9.693	9.445	12.139	15.453	116.81
6	2.5	2.49	-4.415	-6.075	15.677	9.361	12.056	17.941	122.80
7	1.0	0.998	-4.418	-6.124	23.613	9.313	12.008	24.062	130.73

Among the resultant A-weighted noise components, the optics noise shows a noticeable change from -11.11 dB to 23.61 dB for DoE#1 and #7. The same MDD refers to a lower input pressure-referred noise with a more compliant diaphragm. On the contrary, the AOP increases as the diaphragm compliance decreases. From (5.5), this trend is expected.

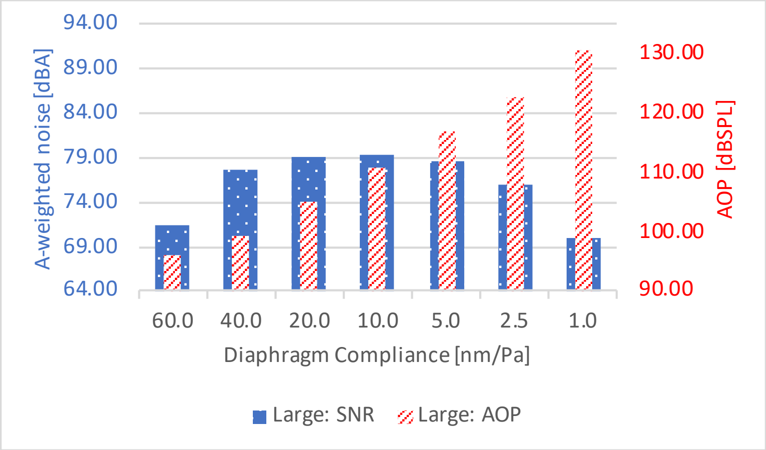

Figure 5.7: Comparison of SNR and AOP from DoE#1 to #7.

Figure 5.7 shows a comparison of SNR and AOP from DoE#1 to #7. In the figure, the SNR is not monotonically decreased as the diaphragm stiffness increases. It is expected that a higher diaphragm compliance (60 nm/Pa) would increase SNR by suppressing the optics noise. However, the highest SNR is achieved with 10 nm/Pa diaphragm 79.34 dB. Figure 5.8 shows the RAW total noise spectra simulated using design #1 to #7. The shaded area represents the frequency range where the A-weighting filter is applied (brick wall at 20 Hz and 20 kHz) for integrated noises.

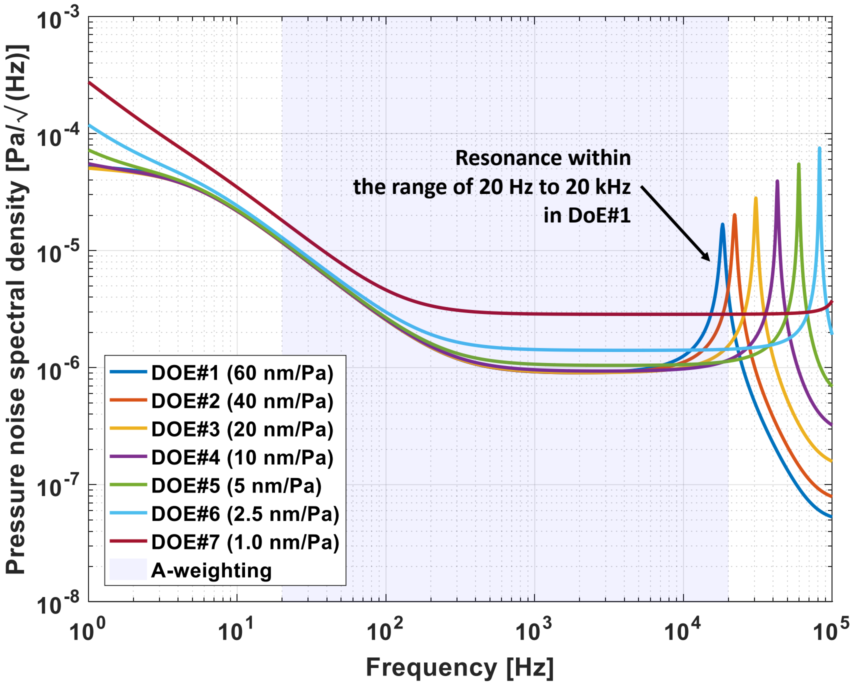

Figure 5.8: Noise spectra with various diaphragm compliances from 60 nm/Pa (DoE#1) to 1 nm/Pa (DoE#7).

Figure 5.9 shows noise components for DoE#1. The high diaphragm compliance (60 nm/Pa) makes the optics noise is corresponding to only 0.04% of the overall noise level. The same figure reveals why the DoE#1 design cannot achieve the highest SNR with the lowest optics noise. The high diaphragm compliance places the system resonance within the operational frequency range (20 Hz to 20 kHz) as shown in Figure 5.8, which in-turn increases the integrated noise level significantly. The 6.1-dB noise reduction can be found from DoE#1 to #2 in Figure 5.8. The optics noise in DoE#2 only corresponds to 0.37% of the overall noise, but the slightly stiffer diaphragm pushes the resonance above 20 kHz, so that the SNR is drastically improved from 71.46 dB (DoE#1) to 77.53 dB (DoE#2).

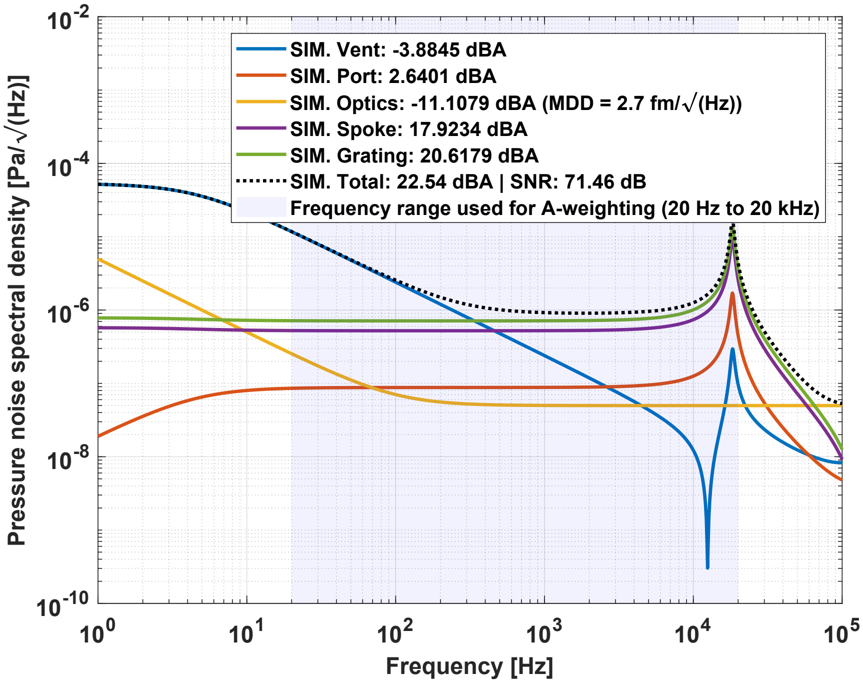

Figure 5.9: Component-wise noise spectra from DoE#1. The excessively compliant diaphragm leads to the system resonance within the operation frequency range, which increases the A-weighted noise figure significantly.

In cases of diaphragm compliances below 10 nm/Pa, the shot noise, i.e., optics, starts becoming a dominant noise source. The same MDD with a stiffer diaphragm leads to a higher input pressure-referred noise. As the diaphragm stiffness increases further, the optics noise exceeds the backplate-induced noise, and therefore the SNR deteriorates rapidly, illustrated in Figure 5.10.

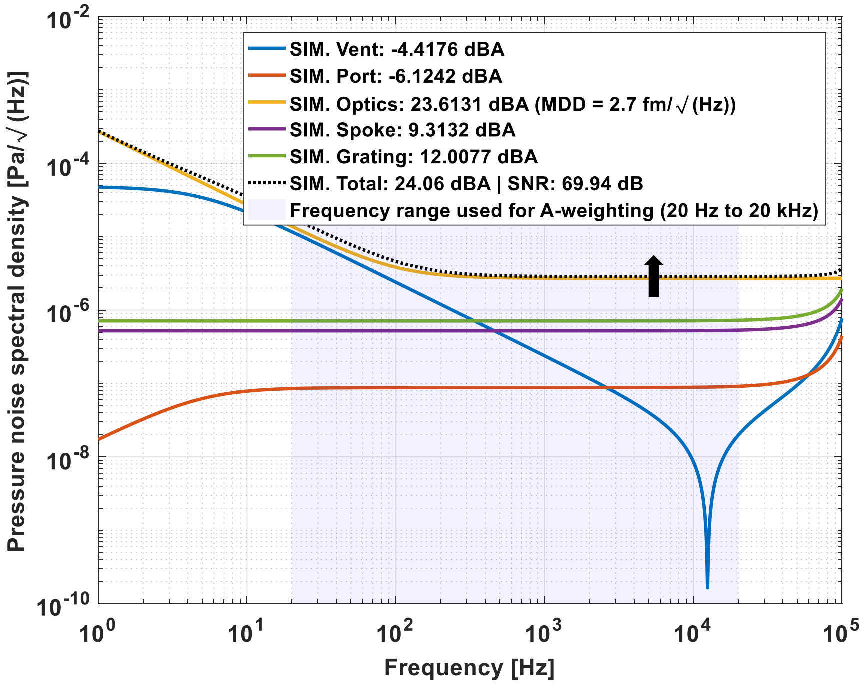

Figure 5.10: Component-wise noises DoE#7. The lower diaphragm compliance is responsible for the high optics noise, which is dominant over the backplate induced noise (grating and spokes).

In terms of AOP, DoE#1 to #7 use a large back-cavity volume, approximately 10× higher than the acoustic compliance of the diaphragm, and therefore the AOP is primarily determined by the diaphragm compliance using (5.5). The most compliant diaphragm results in the worst AOP, 95.99-dB SPL, close to 20-dB lower than commercial capacitive MEMS microphones offering, e.g., 124-dB SPL. Although the highest AOP (130.78-dB SPL) is accomplished with the 1-nm/Pa diaphragm (DoE#7), the DoE#7 design only improves SNR, 4-dB higher than state-of-the-arts capacitive MEMS microphones, so the figure-of-merit is vanished. If a similar AOP performance to capacitive MEMS microphone is required, the DoE#6 would offer both improved SNR and comparable AOP.

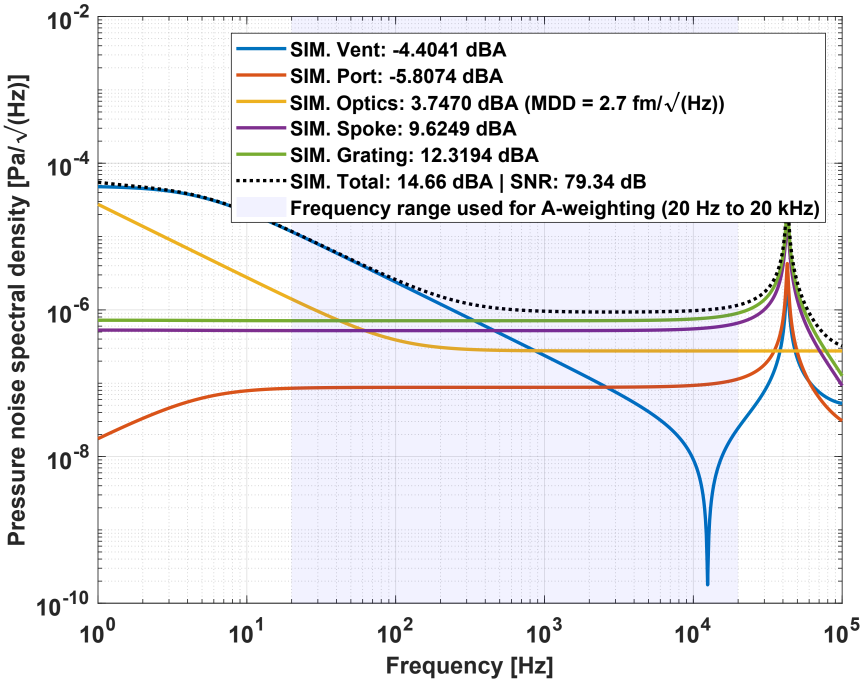

Figure 5.11: Component-wise noise spectra from DoE#4. This design achieved the highest SNR, 79.34 dB among DoE#1 to #7.

The highest SNR design (DoE#4) in Figure 5.11 would be useful for voice recognition applications, in which a higher SNR is preferred over a wider DR.

5.4 Design of Experiments - Small Microphone Case

In the previous section, SNR and AOP trend for an optical microphone with a large packaging was studied with seven different diaphragm compliance from 60 nm/Pa to 1 nm/Pa. In this section, the same analysis was performed for a smaller packaging case. V_{bc} is set to 2 mm^3, instead of 31.52 mm^3 used in the DoE#1 to #7. The summary of the DoE is presented in Table 5.6.

Table 5.6: Component-wise noise for DoE#63 to #69.

DoE #	C_{mp} (nm/Pa)	$C_{mp,int}$ (nm/Pa)	Vent noise (dBA)	Port noise (dBA)	Optics noise (dBA)	Spoke noise (dBA)	Grating noise (dBA)	Total noise (dBA)	AOP (dBSPL)
63	60	19.0	9.000	-5.382	-1.990	10.207	12.901	15.895	105.12
64	40	16.4	8.993	-5.516	-0.712	10.022	12.717	15.775	106.40
65	20	11.7	8.981	-5.733	2.277	9.755	12.449	15.669	109.39
66	10	7.36	8.970	-5.903	6.262	9.560	12.254	15.822	113.38
67	5	4.24	8.963	-6.016	11.052	9.435	12.129	16.625	118.17
68	2.5	2.29	8.958	-6.082	16.382	9.362	12.057	18.826	123.51
769	1.0	9.65	8.955	-6.125	23.904	9.315	12.010	24.444	131.03

The acoustic compliance of the back-cavity C_{abc} is 1.09434×10^{-14} m^3/Pa. Compared to C_{abc}, the 60-nm/Pa diaphragm compliance can be converted to acoustic compliance $C_{ad} = 2.3562\times10^{-14}$ m^3/Pa using $A_{d,eff} = \beta A_d$, where $\beta = 0.5$. From (5.6), the combination of C_{abc} and C_{ad} leads to $C_{mp,int} = 19$ nm/Pa, even if a 60-nm/Pa diaphragm compliance is used.

From (5.6), when a diaphragm compliance is much smaller than the back cavity compliance, the integrated microphone compliance, $C_{am,int} \approx C_{ad}$. On the contrary, if the C_{ad} is the same as C_{abc}, the integrated compliant $C_{mp,int} = 0.5C_{ad}$.

$$C_{am,int} = \frac{C_{ad}C_{abc}}{C_{ad} + C_{abc}} \tag{5.6}$$

For the 5-nm/Pa diaphragm, the corresponding acoustic compliance of the diaphragm $C_{ad} = 5.573C_{abc}$, and therefore $C_{am,int} \approx 0.848C_{ad}$ using (5.6). The stiffer $C_{mp,int}$ increases the optics noise. In Figure 5.12, the optics noise becomes another dominant noise source with a diaphragm compliance below 5 nm/Pa.

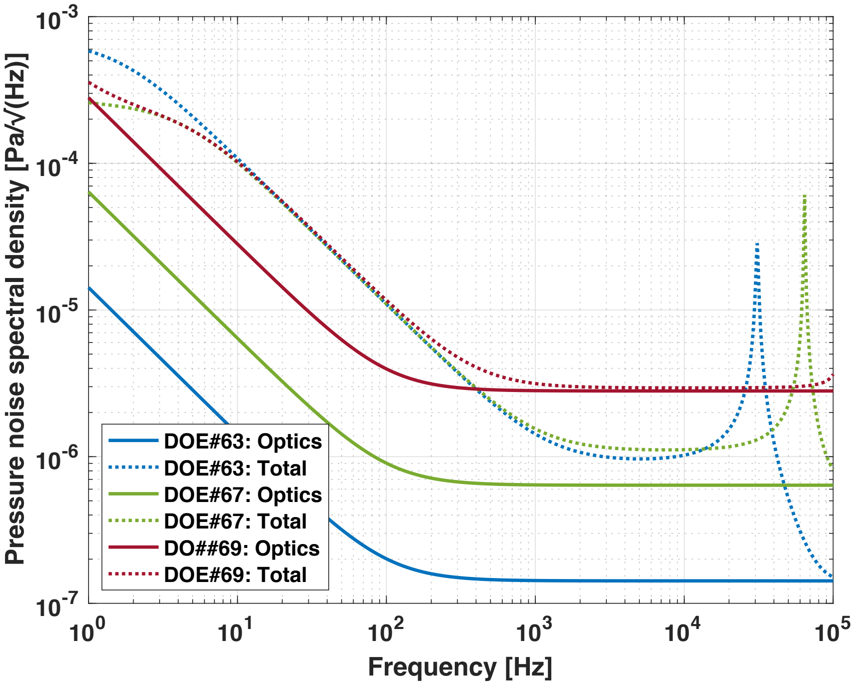

Figure 5.12: Noise spectra from DoE#63, #67, and #69. As the diaphragm is stiffer, the optics noise increases significantly.

Figure 5.13 shows the trend of SNR and AOP for a small optical microphone packaging. SNR deteriorates rapidly as the optics noise increases while the rest of noise components remain approximately the same. Unlike the large packaging case, the higher diaphragm compliance (DoE#63) still has the integrated system resonance is mostly out of the 20-Hz-to-20-kHz frequency range so the 60-nm/Pa diaphragm does not drastically decrease the SNR.

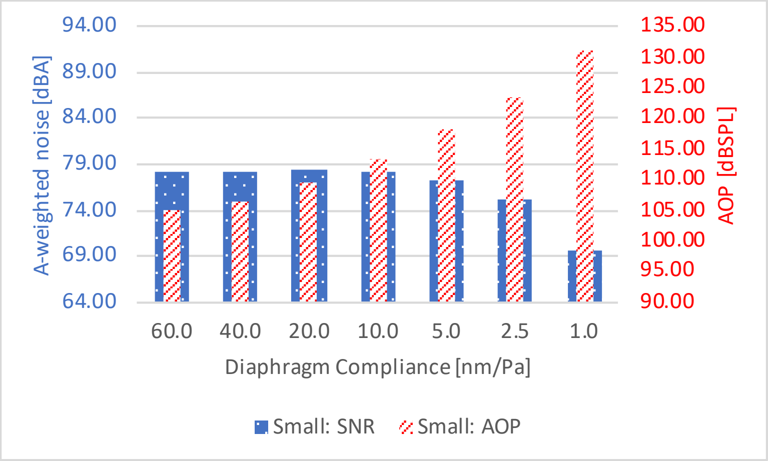

Figure 5.13: Comparison of SNR and AOP from DoE#63 to #69.

Above $C_{mp} = 5$-nm/Pa, the $C_{mp,int}$ is affected by the back-cavity compliance, and therefore the AOP is not linearly increased as the diaphragm compliance decreases down to 10 nm Pa. However, below 5 nm/Pa, the diaphragm directly affects the $C_{mp,int}$, AOP is increased proportionally.

5.5 Design of Experiments - Low Cut-Off Frequency with a Small Back Cavity

In this DoE, the effect of the acoustic low cut-off frequency to microphone SNR is explored. The low cut-off frequency is set by R_{avent} and C_{abc} to compensate wind noise. Since the wind noise is dominant at frequencies up to 100 Hz [8], a low cut-off frequency of capacitive MEMS microphones is typically set to 80 to 100 Hz. Equation (5.7) shows that a higher R_{avent} is required to achieve a lower cut-off frequency f_{cut} when the back-cavity compliance is fixed.

$$f_c = \frac{1}{2\pi R_{avent} C_{abc}} \tag{5.7}$$

The diaphragm compliance C_{mp} and the back-cavity volume V_{bc} are set to 10 nm/Pa and 1.52 mm^3 respectively. The rest of system parameters are used as listed in Table 5.1. Table 5.7 summarizes the resultant SNR with different cut-off frequencies from 5 Hz to 100 Hz.

Table 5.7: Component-wise noises from DoE#25, #45 to #50. In this set of DoE, the low cut-off frequency is perturbed from 5 Hz to 100 Hz.

DoE #	f_{cut} (Hz)	R_{avent} (Pa·s/m^3)	Vent noise (dBA)	Port noise (dBA)	Optics noise (dBA)	Spoke noise (dBA)	Grating noise (dBA)	Total noise (dBA)
25	5	$2.91\times10^{+12}$	8.970	-5.903	6.262	9.560	12.254	15.822
45	10	$1.45\times10^{+12}$	11.979	-5.903	6.262	9.560	12.254	16.637
46	20	$7.27\times10^{+11}$	14.982	-5.903	6.262	9.560	12.254	17.911
47	40	$3.64\times10^{+11}$	17.967	-5.904	6.262	9.560	12.255	19.682
48	60	$2.42\times10^{+11}$	19.691	-5.905	6.262	9.561	12.256	20.916
49	80	$1.82\times10^{+11}$	20.896	-5.906	6.262	9.562	12.257	21.854
50	100	$1.45\times10^{+11}$	21.814	-5.908	6.262	9.563	12.258	22.605

In the table, it is observed that the R_{avent} does not affect other noise components. In addition, the SNR becomes small as the vent resistant R_{avent} is lowered, in which A-weighted noise increases from 15.82 dBA to 22.61 dBA, i.e., 6.78-dB higher noise. The reason of this potentially counter-intuitive behavior is illustrated in Figure 5.14. In the figure, although a lower f_{cut} causes a higher R_{avent}, the higher R_{avent} does not affect to the A-weighted floor since the effect is dominant outside of the operational range.

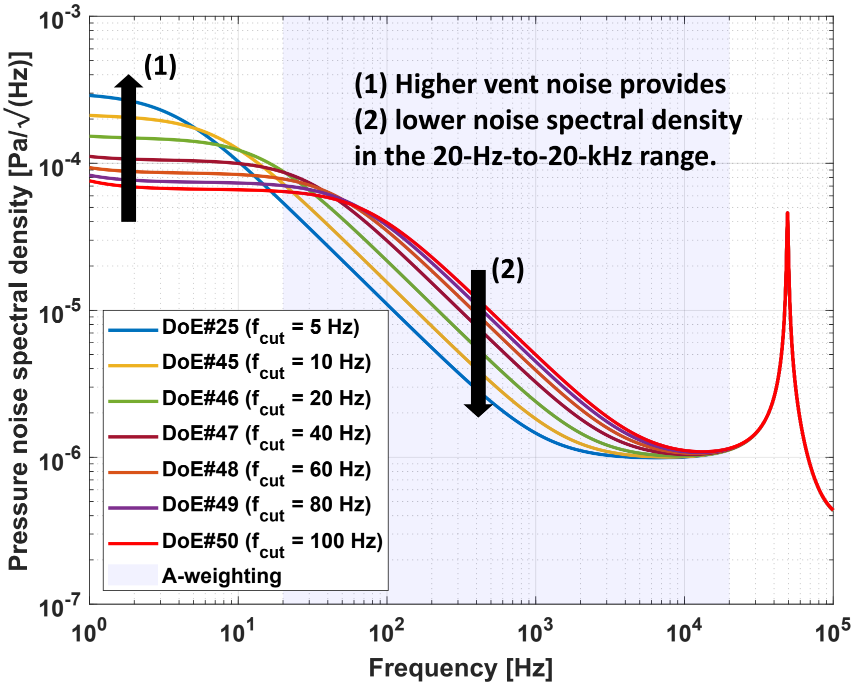

Figure 5.14: System noise spectra comparison from DoE#25, #45 to #50.

Setting the cut-off frequency as low as possible lowers noise, as the 20-dB/sec slope starts at a lower frequency. The lower f_{cut} effect becomes more significant when the back-cavity volume is smaller. As V_{bc} becomes smaller, the back-cavity compliance is also linearly decreased, and the vent resistance therefore must be higher to achieve the same cut-off frequency. Figure 5.15 shows the overall system noise from DoE#13 and #50. DoE#13 is simulated with the same as DoE#50 but the back-cavity volume set to 31.52 mm^3 instead of 1.52 mm^3. The cut-off frequency is the same 100 Hz for both cases, but the resultant A-weighted noise is drastically different (7.1 dB higher in DoE#50).

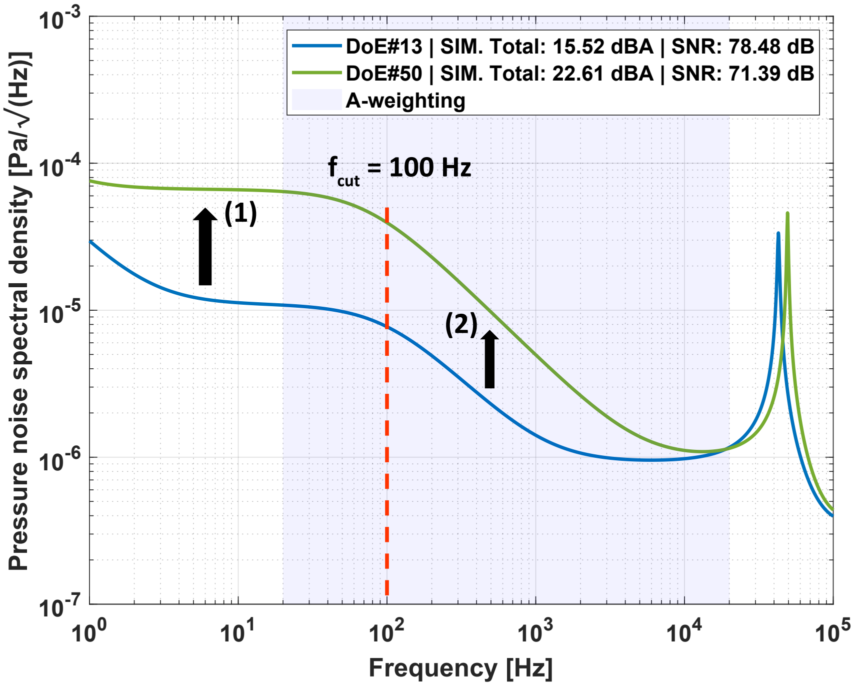

Figure 5.15: Comparison of DoE#13 and #50. Both designs utilize $f_{cut} = 100$ Hz. However, the smaller back-cavity volume makes the A-weighted noise with DoE#50 7.1-dB higher than DoE#13, which has identical system components except a larger back-cavity volume.

The back-cavity of DoE#13 is 20.76× larger than that of DoE#50, and therefore R_{avent} in DoE#50 is 20.76× higher (effect 1 on Figure 5.15). In consequence, the spectral density on the 20 dB/decade region is increased significantly in DoE#50 (effect 2 on Figure 5.12). This result suggests that setting a low cut-off frequency plays a critical role to achieve a high SNR when using a smaller MEMS microphone packaging. In case of optical microphone, the low cut-off frequency can be set to a much lower value, such as 5 Hz, since the wind noise effect can be suppressed using the integral action, used for the

DC tuning of the diaphragm, rather than relying on the acoustic low-cut off behavior.

5.6 Design of Experiments - Effect of Additional Inlet Port

A MEMS microphone is typically attached to a PCB using a solder reflow process. In case of a bottom-port MEMS microphone, the attached PCB must provide a sound inlet. The effect of additional port is focused in this study. The additional inlet port can be also formed by electronics housing itself, e.g., a sound inlet port on smartphones. In this study, the additional port radius is changed from 0.4 mm to 0.2 mm, while the length of the port is set to 1 mm for all cases. The microphone parameters remain the same as those of DoE#4. Table 5.8 shows the additional acoustic mass and resistance for each radius, which are placed in series with the microphone inlet port mass and resistance.

Table 5.8: Additional acoustic resistance and mass due to the additional sound port (circular) induced by the PCB that the optical microphone is attached to.

DoE #	PCB port radius (mm)	$R_{a,PCB}$ (Pa·s/m^3)	$m_{a,PCB}$ (kg/m^4)
51	0.40	$1.8502\times10^{+6}$	$4.0107\times10^{+3}$
52	0.35	$3.1563\times10^{+6}$	$4.9734\times10^{+3}$
53	0.30	$5.8475\times10^{+6}$	$6.4086\times10^{+3}$
54	0.25	$1.2125\times10^{+7}$	$8.7090\times10^{+3}$
55	0.20	$2.9603\times10^{+7}$	$1.2796\times10^{+4}$

Figure 5.16 shows the comparison of the simulated noise spectra with

the additional inlet port mass and resistance, and Table 5.9 summarizes the DoE result.

Table 5.9: Component-wise noises from DoE#4, #51 to #55.

DoE #	R_{aport} (Pa·s/m^3)	m_{aport} (kg/m^4)	Vent noise (dBA)	Port noise (dBA)	Optics noise (dBA)	Spoke noise (dBA)	Grating noise (dBA)	Total noise (dBA)
4	$4.697\times10^{+5}$	$7.116\times10^{+2}$	-4.404	-5.807	3.747	9.625	12.319	14.658
51	$2.320\times10^{+6}$	$4.722\times10^{+3}$	-2.100	1.954	3.747	10.209	12.904	15.386
52	$3.626\times10^{+6}$	$5.685\times10^{+3}$	-0.616	4.195	3.747	10.422	13.116	15.726
53	$6.317\times10^{+6}$	$7.120\times10^{+3}$	2.142	7.238	3.747	10.867	13.561	16.456
54	$1.269\times10^{+7}$	$9.421\times10^{+3}$	9.830	13.235	3.747	13.056	15.750	19.583
55	$3.007\times10^{+7}$	$1.351\times10^{+4}$	19.466	22.894	3.747	17.872	20.567	26.634

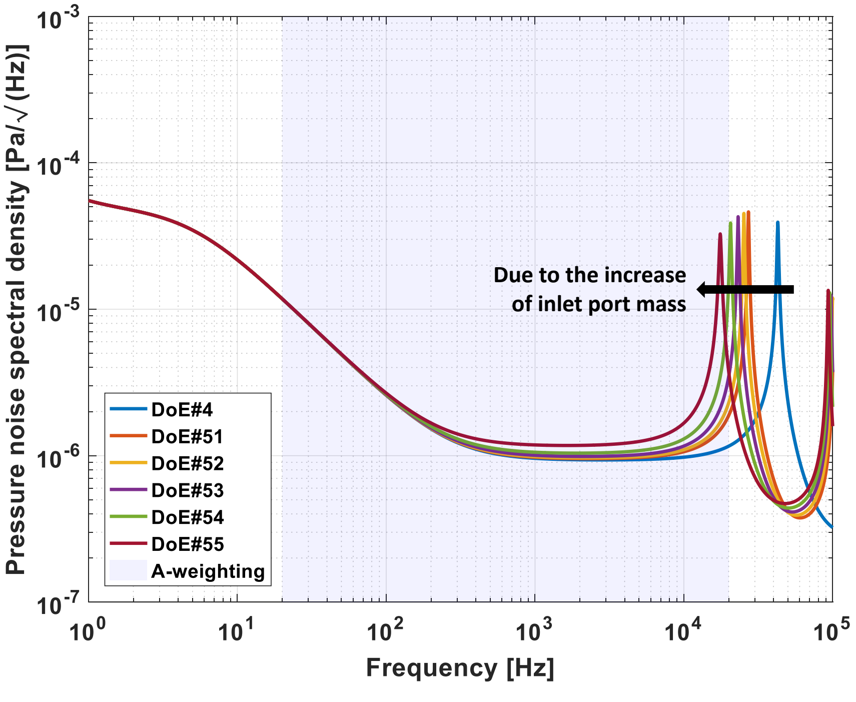

Figure 5.16: System noise spectra comparison from DoE#4, #51 to #55.

Figure 5.17 presents the effect of port-induced noise to the system noise level by comparing DoE#4, #51, and #55. When comparing DoE#54 to DoE#50, R_{aport} and m_{aport} are increased as much as 12.96× and 18.98× as the diameter of the additional inlet port is decreased from 0.4 mm to 0.2 mm.

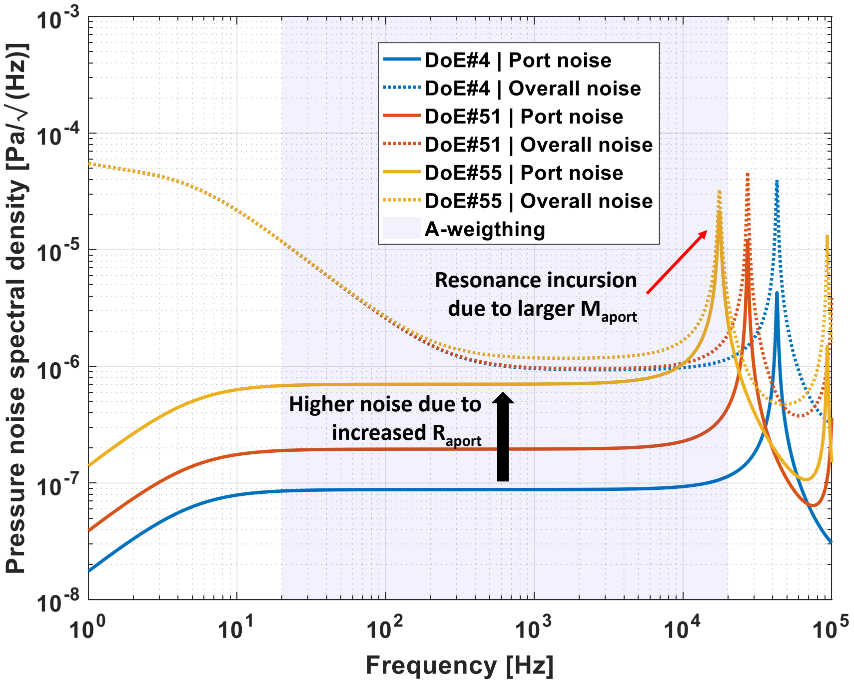

Figure 5.17: Comparison of Port-induced noise and overall noise spectra for DoE#4, #51 to #55.

Due to the increased R_{aport}, the system noise spectral density at 1 kHz in DoE#55 is 1.217× higher (or 1.70 dB) than that of DoE#51. However, the resultant system noise change is much more significant, i.e., 11.25-dB. The noise penalty is induced by the incursion of the system resonance into the 20-Hz-to-20-kHz range due to the increased m_{aport}. This illustrates the importance of the electronics housing design to utilize the full potential of a high-performance MEMS microphone. This study shows that a final SNR can be reduced significantly (11.98 dB for DoE#55) depending on the design of additional sound inlet port, even if the same MEMS microphone is used.

5.7 Design of Experiments - Effect of Limited Electrical Power Budget and Packaging Size

In the design of a MEMS microphone, electrical power consumption is one of the key specifications. Majority of consumer electronics use a battery and therefore a lower power consumption would be beneficial. Some commercial MEMS microphones utilize high/low-performance modes to reduce power consumption. A high-performance analog capacitive MEMS microphone can consume up to 500 μW. On top of the electrical power constraint, mobile consumer electronics also demand a smaller microphone packaging. In this section, optical microphone performance with a small package size is studied while the MDD is limited by the power budget. The back-cavity volume is gradually changed from 31.52 mm^3 to 0.318 mm^3.

To understand how the optical microphone performs under the power consumption level comparable to that of capacitive MEMS microphones, this DoE assumes the available electrical power is 400 μW for optics. From Table 5.4 , the given electrical power budget with 100% ME can achieve 8.56-fm/$\sqrt{\text{Hz}}$ MDD, rather than 2.71 fm/$\sqrt{\text{Hz}}$ when allowing 4-mW electrical power. Table 5.10 shows the DoE results with the two constraints.

Table 5.10: Component-wise noises from DoE#4, #32, #38 to #44.

DoE #	V_{bc} (mm^3)	$C_{mp,int}$ (nm/Pa)	R_{avent} (Pa·s/m^3)	Vent noise (dBA)	Port noise (dBA)	Optics noise (dBA)	Spoke noise (dBA)	Grating noise (dBA)	Total noise (dBA)	AOP (dBSPL)
4	31.52	9.84	$1.40\times10^{+11}$	-4.40	-5.81	3.75	9.63	12.32	14.66	110.86
31	31.52	9.84	$1.40\times10^{+11}$	-4.40	-5.81	13.75	9.63	12.32	17.04	110.86
38	15.52	9.67	$2.85\times10^{+11}$	-1.23	-5.81	13.90	9.62	12.31	17.14	111.01
39	7.518	9.33	$5.87\times10^{+11}$	1.98	-5.83	14.21	9.61	12.30	17.35	111.32
40	3.518	8.66	$1.26\times10^{+12}$	5.31	-5.85	14.85	9.59	12.29	17.80	111.97
41	1.518	7.36	$2.91\times10^{+12}$	8.97	-5.90	16.26	9.56	12.25	18.82	113.38
42	0.518	4.88	$8.52\times10^{+12}$	13.64	-5.99	19.84	9.53	12.22	21.63	116.96
43	0.407	4.28	$1.09\times10^{+13}$	14.69	-6.01	20.98	9.53	12.23	22.57	118.10
44	0.318	3.69	$1.39\times10^{+13}$	15.76	-6.04	22.27	9.55	12.24	23.66	119.39

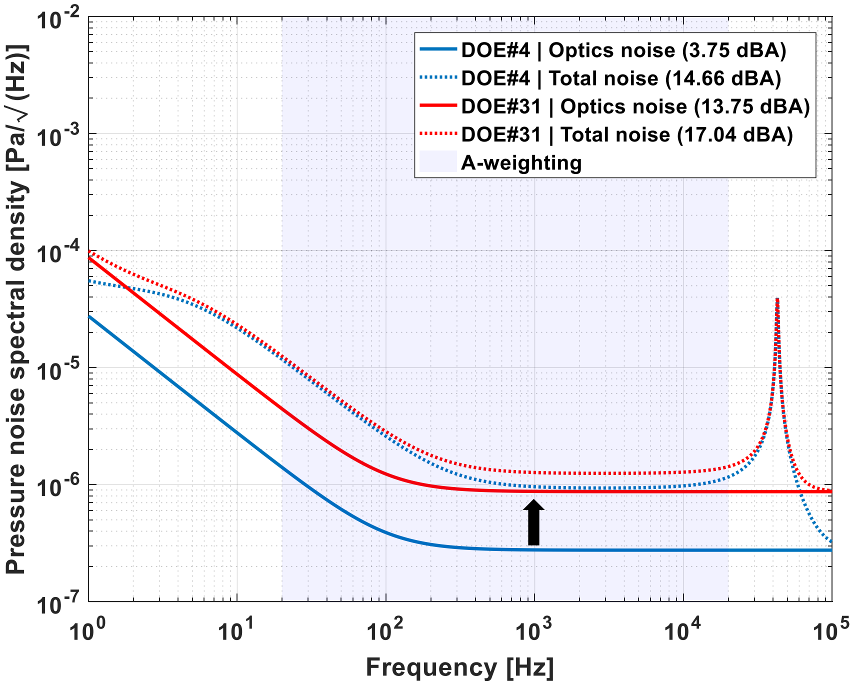

Figure 5.18: A comparison of noise spectra between DoE#4 and DoE#31. The noise penalty due to the higher MDD 8.56 fm/$\sqrt{\text{Hz}}$ in DoE#31 from 2.71 fm/$\sqrt{\text{Hz}}$ in DoE#4 is observable.

Figure 5.18 shows the optics and total noise spectra for DoE#4 and

DoE#31. In the figure, the comparison between DoE#4 and #31 illustrates the noise penalty due to the higher MDD caused by the electrical power limitation with the same large back-cavity volume. The optics noise directly shows the 10-dB penalty originated from the higher MDD (from 2.7075 fm/$\sqrt{\text{Hz}}$ to 8.5618 fm/$\sqrt{\text{Hz}}$), which results 2.38-dB higher total noise in DoE#32, compared to DoE#4.

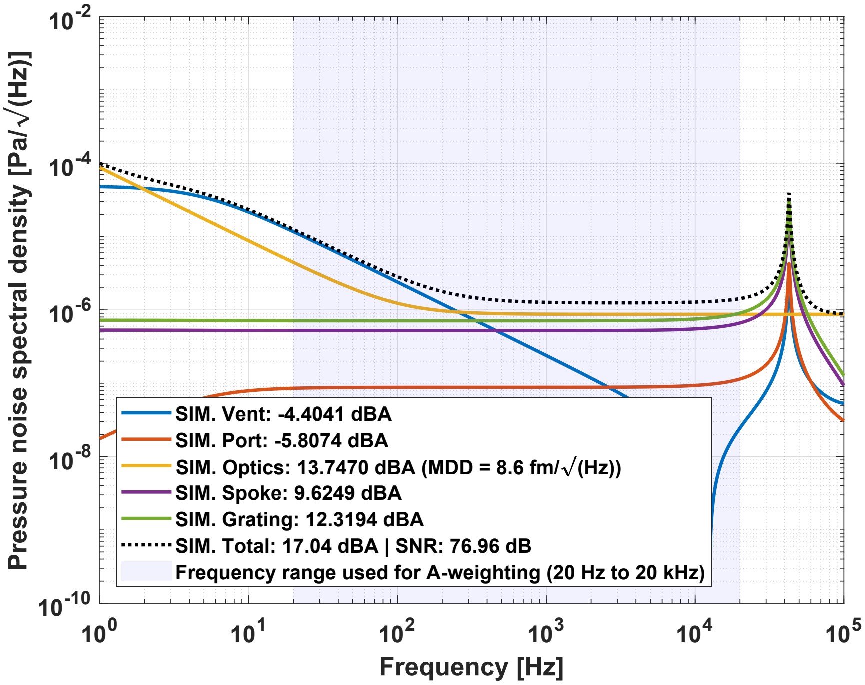

Figure 5.19: Component-wise noise spectra from DoE#31. The optics noise becomes higher than the backplate induced noises, i.e., grating and spoke noises.

Figure 5.19 shows the component-wise noise spectra with DoE#31. The higher MDD also makes the microphone is no-longer thermal-mechanical noise limited. In other words, the optics noise exceeds the back-plate induced noise, in which the advantage of having a minimalistic backplate for a low-noise microphone starts vanishing.

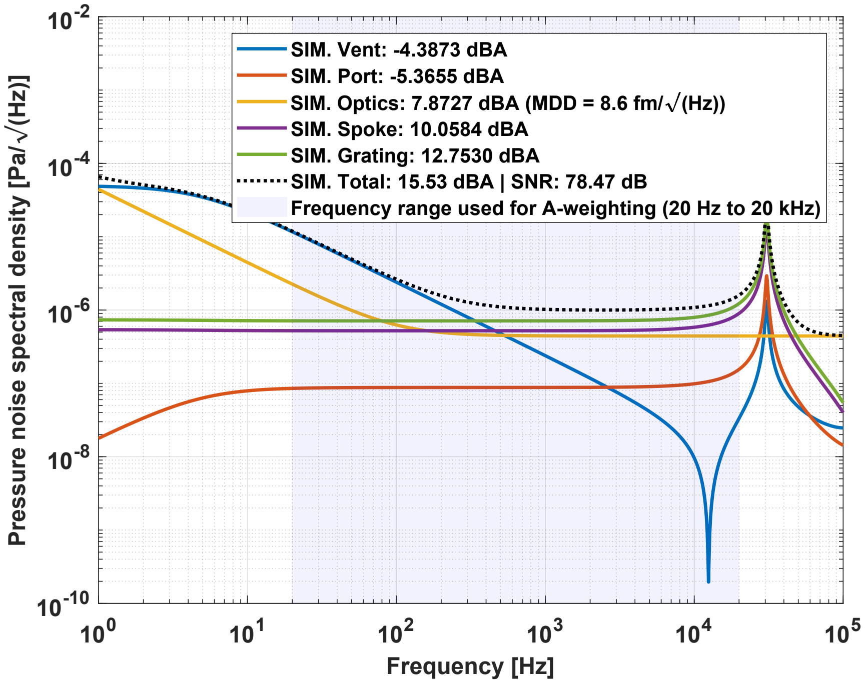

Figure 5.20: Component-wise noise spectra with a 20-nm/Pa diaphragm compliance. The rest of the system parameters are the same as DoE#31.

Figure 5.20 shows the component-wise noise spectra with DoE#31 except using a 20-nm/Pa diaphragm instead 10-nm/Pa diaphragm compliance. In order to achieve a thermal-mechanical noise limited microphone with the same MDD, a more compliant diaphragm is a solution without having a smaller grating, i.e., a lower back-plate flow resistance. In Figure 5.20, the SNR is improved owing to the lowered optics noise with the 20-nm/Pa diaphragm.

However, the 6-dB higher diaphragm compliance lowers the AOP performance as much as 6 dB, from 111-dB SPL to 105-dB SPL. The design compromise must be made to achieve a high SNR, which in-turn results in a low AOP with the given backplate design. In order to overcome the design a force-feedback optical microphone concept is explored in the following chapter.

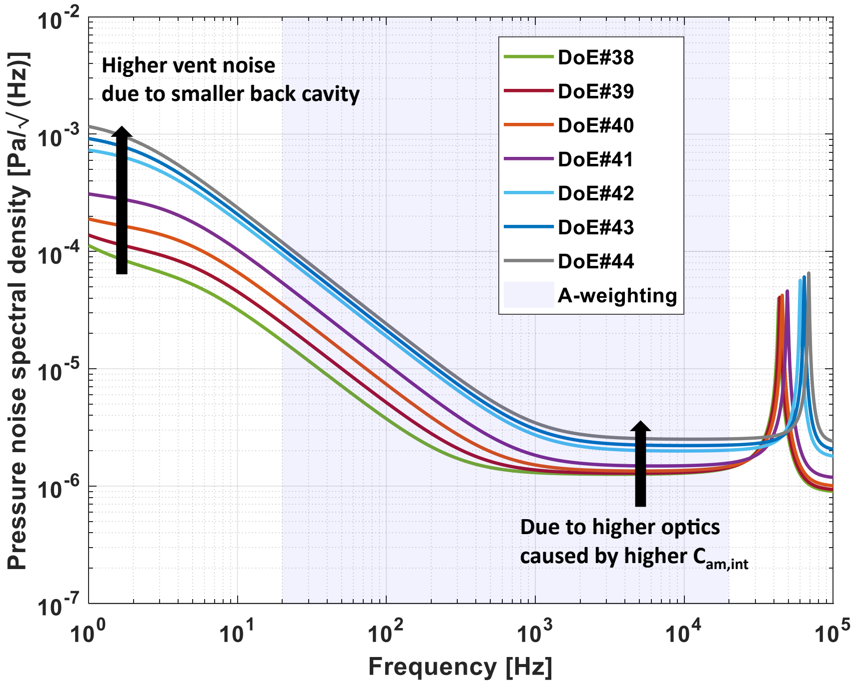

Figure 5.21: System noise spectra comparison from DoE#4, #32, #38 to #44.

Figure 5.21 shows the total noise comparison among DoE#38 to #44, in which the back-cavity volume V_{bc} is decreased from changed from 15.5 mm^3 to 0.318 mm^3 as listed in Table 5.10. The smaller back-cavity volume with the fixed low cut-off frequency leads to a higher vent resistance, and therefore the vent noise contribution to the overall noise increased, also shown in Table 5.10. The smaller back-cavity volume also leads to a smaller back-cavity compliance. Since the acoustic back-cavity compliance and the diaphragm compliance are connected in series, and therefore the system compliance starts being reduced by the back-cavity compliance.

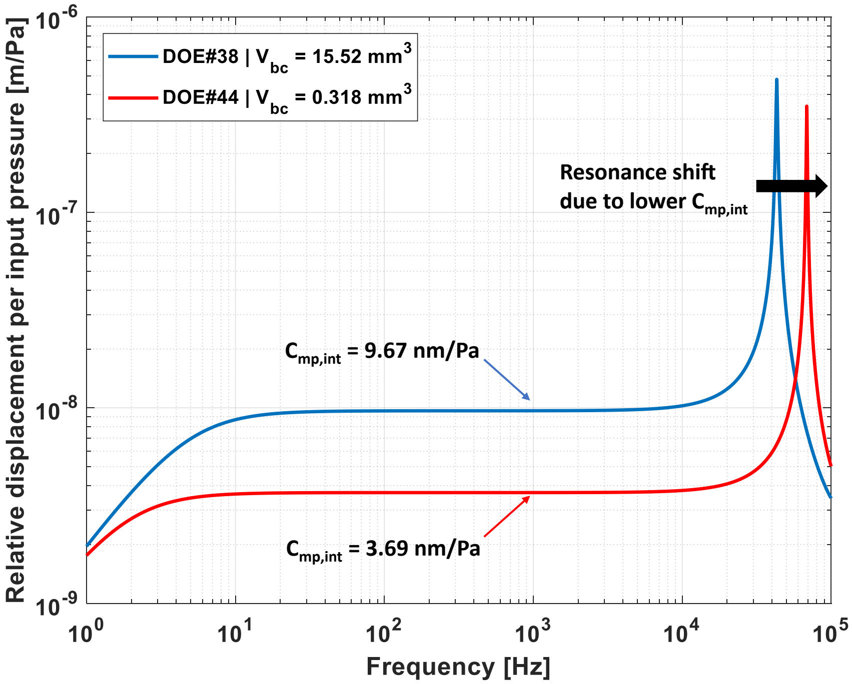

Figure 5.22: Diaphragm deflection due to unit pressure input for DoE#38 and #44. The small back-cavity volume in DoE#44 leads to a smaller diaphragm deflection compared to DoE#38. At 1 kHz, the membrane in DoE#38 and #44 deflects 9.67 and 3.69 nm/Pa respectively.

Figure 5.22 shows the diaphragm deflection under unit-pressure input for DoE#38 and DoE#44. The diaphragm still deflects 9.67 nm/Pa in

DoE#38, which suggest the large-enough back-cavity volume does not increase the microphone stiffness. Whereas the system compliance becomes 3.69 nm/Pa in DoE#44 even if the same diaphragm compliance (10 nm/Pa) is used. The lowered integrated system compliance in DoE#44 can be estimated using (5.6). The acoustic compliance of the diaphragm C_{ad} is 3.9270×10^{-15} m^3/Pa, and, the back-cavity compliance C_{abc} of DoE#44 is 3.9270×10^{-17} m^3/Pa. Equation (5.6) predicts $C_{am,int}$ as 1.4474×10^{-15} m^3/Pa, and $C_{mp,int} = C_{am,int}A_{deff}$, which predicts 3.686 nm/Pa as simulated. This emphasizes the significance of the packaging effect as the microphone is miniaturized further.

5.8 Summary

In this chapter, design of a microphone toward sub 15-dBA noise floor via design of experiments. Whereas various parameters define the microphone total noise (or SNR) and AOP, several key parameters focused in this chapter, such as diaphragm compliance, packaging effect including the inlet port and back-cavity volume, and electrical power budget. For a smaller optical microphone with a limited electrical power budget, a compliant diaphragm is necessary to realize a thermal-mechanical noise limited optical microphone without using a smaller grating, which is limited by the beam divergence on the used VCSEL. On the other side, the use of a more compliant diaphragm deteriorates AOP.

In the next chapter, a force-feedback optical microphone concept to overcome the illustrated AOP limitation via closed-loop operation. The proposed force-feedback optical microphone utilizes piezoelectric actuators to counterbalance the acoustic pressure, and by doing so a higher AOP than the intrinsic DR provided by the optics is achievable.

Chapter 6

Feasibility Study - Piezoelectric Optical Microphone

6.1 Motivation of the Piezoelectric Optical Microphone

The rigorous DoE presented in Chapter 5 shows the design path toward an optical microphone with sub 15-dBA noise floor. The DoE#4 design achieved 79.34-dB SNR or 14.66-dBA noise. The simulated SNR is 10-dB higher than state-of-the-art capacitive MEMS microphones, owing to the minimalistic backplate and interferometric displacement detection scheme. However, the AOP of the same design is 110.86-dB SPL, which is 10-dB lower than capacitive MEMS microphones, distorting typically at 120-dB SPL higher. If the capacitive MEMS microphone has 32-dBA noise, the DR is 88 dB. Interestingly, the DR of the DoE#4 design is 96.21 dB, which implies the DoE#4 design has an 8.2-dB wider DR . However, the 17.3-dB lower A-weighted noise in the DoE#4 design makes the optical microphone design distort at a 9.1-dB lower sound pressure, compared to the capacitive MEMS microphone.

To offer a higher AOP without compromising the SNR, it is necessary to extend the intrinsic DR of an optical microphone using force-feedback (i.e., closed-loop). Figure 6.1 presents a block diagram of the proposed force feedback optical microphone. In the figure, the reference signal $R(s)$ is 0 V, in which the diaphragm is stationary so the differential TIA output of 0th and ±1st order PDs is zero. When a disturbance signal $D(s)$, i.e., input sound pressure, presents, the TIA output generates non-zero output, which becomes error signal, V_{error}. The error signal V_{error} is in-turn fed into the PID controller to generate a control signal (voltage to the diaphragm actuator) to compensate the diaphragm motion. The error signal also serves the output signal of the force-feedback optical microphone.

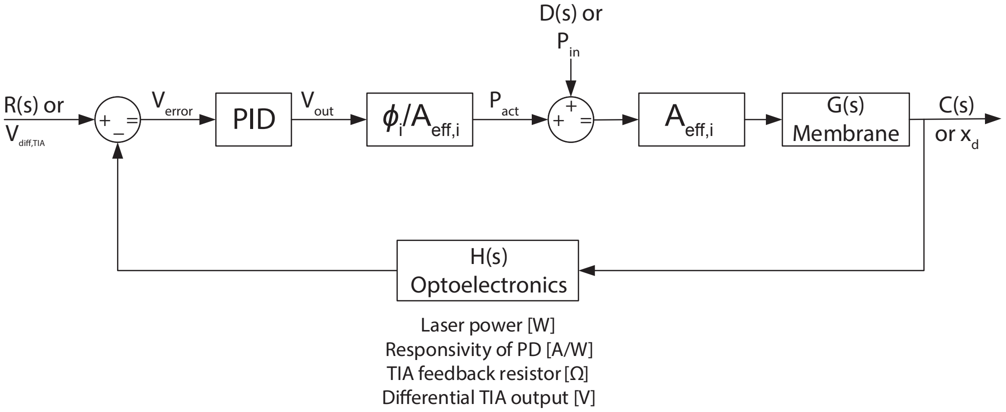

Figure 6.1: A block diagram illustrating the force-feedback operation of piezoelectric optical microphone.

In closed loop, the AOP is limited by the pressure that the internal actuator can generate. For MEMS transducers, electrostatic, piezoelectric, and magnetic actuators are common solutions for actuation. Electrostatic actuation is a common choice for sensing and actuation applications since it can be easily fabricated, using conductive films. However, it requires a relatively high voltage level to generate a large actuation force. Especially even higher actuation voltage is required for an optical microphone to achieve the same displacement with a capacitive MEMS microphone due to the smaller active area of the minimalistic backplate. In addition, the electrostatic actuation cannot perform a bi-directional actuation unless the diaphragm is pre-biased. Finally, since the electrostatic force is proportional to V^2, the closed-loop operation in conjunction with the non-linear electrostatic actuation force becomes more challenging. In case of magnetic actuator, a large force can be generated, but the necessity of placing relatively bulky magnets near the diaphragm makes this solution less viable on small microphone package. A piezoelectric-film-based, e.g., lead zirconate titanate or aluminum nitride, actuator can be the most suitable solution for force-feedback application over electrostatic or magnetic actuation. A piezoelectric-based actuator offers several advantages; linear-actuation behavior, small actuation voltage for a large displacement, and bi-directional actuation capability. In addition, the piezoelectric film actuators reside directly on top of the diaphragm, so no significant system change is required to implement the force-feedback function. Finally, the fabrication process for the piezoelectric actuator can be easily integrated into the existing MEMS microphone fabrication process.

6.2 A Silicon Membrane with Piezoelectric Actuators

6.2.1 Overview

The key change of the piezoelectric optical microphone from the electrostatic embodiment is illustrated in Figure 6.2. Figure 6.2(a) illustrates an optical microphone with electrostatic actuation. The doped p-Si membrane for electrostatic actuation is replaced with a Si diaphragm with piezoelectric actuators for force-feedback operation as illustrated in Figure 6.2(b).

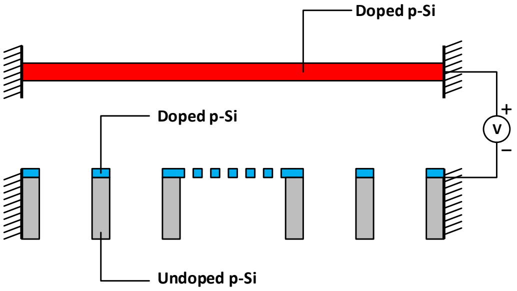

(a)

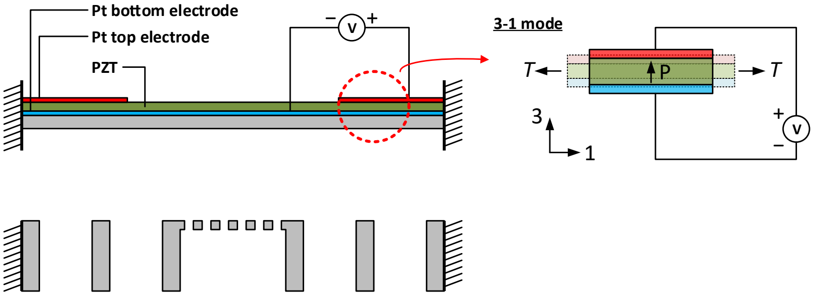

(b)

Figure 6.2: Micrographs of the topside of the backplate module after PECVD SiNx deposition.

Piezoelectric-based MEMS devices have been studied in numerous literatures [27] [28] [29] [30] [31]. A piezoelectric material forms internal dipole moment along a certain direction, known as poling direction, and therefore the piezoelectric material can induce mechanical stress or strain by applying electric field across its polarization direction, which is known as indirect effect. The opposite process is also used for sensing applications. The following set of equations represents the constitutive relationship of a piezoelectric material.

$$\begin{aligned} T &= c^E S - e^{tr} E, \\ D &= eS + \varepsilon^S E, \end{aligned} \tag{6.1}$$

where, T, S, E, and D are stress, strain, E-field, and surface charge density, respectively.

The membrane in Figure 6.2(b) can be modeled using the lumped-parameter network model as shown in Figure 6.3. In Figure 6.3, the transformer ratio ϕ couples the electrical domain and mechanical domain as shown in (6.2).

$$\phi = \left.\frac{F}{V}\right|_{blocked} = \left.\frac{q}{\delta}\right|_{sc} \tag{6.2}$$

where, F is the force acting on the diaphragm, V is the open-circuited voltage across the piezoelectric film, q is the short-circuited charges induced by the piezoelectric film, and δ is the diaphragm center displacement.

Commonly used piezoelectric materials are: aluminum nitride (AlN), zinc oxide (ZnO), lead zirconate titanate (PZT), and polyvinylidene fluoride (PVDF) [31] [32]. For sensing applications, AlN is typically preferred due to its lower dielectric loss, which is commonly the dominant thermal noise source for piezoelectric-based sensors. For actuating applications, PZT is a common

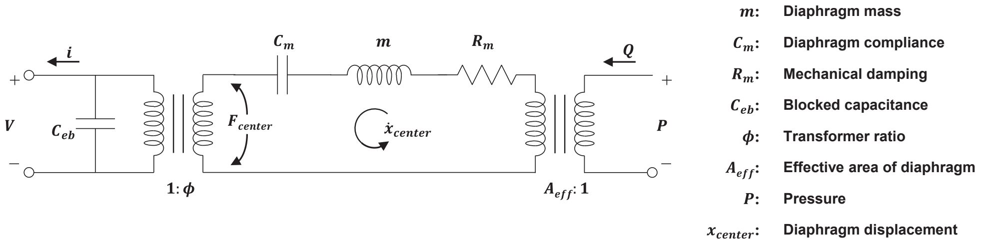

Figure 6.3: A simplified equivalent-circuit model of the piezoelectric Si membrane for force feedback operation.

choice due to its high coupling coefficient or transformer ratio [27]. A piezoelectric coefficient $e_{31,f}$ can be used to compare different piezoelectric materials in terms of actuation capability [32]. Compared to AlN, PZT produces 12× higher actuation pressure. PZT is chosen for this reason.

6.2.2 Verification of the Concept of a Pizeoelectric Si Membrane

In Figure 6.2(b), the configuration of the piezoelectric actuator is known as 3-1 mode. The inset of Figure 6.2(b) illustrates the 3-1-mode operation, in which the poling direction P, i.e., internal dipole, is aligned to the 3-direction (i.e., normal to the electrodes) and the actuation axis is the 1-direction [29]. Figure 6.4 shows the Si membrane with ring-shaped piezoelectric actuators. The Si membrane has a second annular-shaped actuator placed inside of the outer PZT actuator, to the purpose for two actuators to maintain a flat surface at the center of the diaphragm, so that the membrane behaves more like a flat mirror. In this configuration, an opposite polarity signal compared to the counterbalancing signal to the outer actuator is fed into the inner actuator to induce opposite deflection curvatures so that the center of the diaphragm flat as possible.

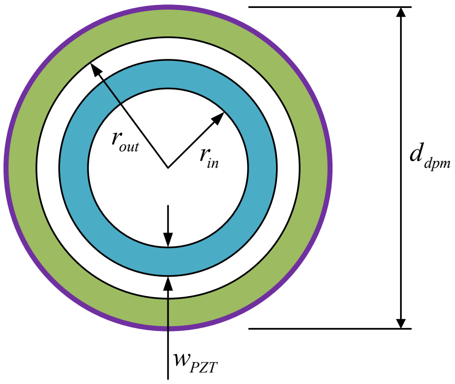

Figure 6.4: Schematic of the Si membrane with dual-ring piezoelectric actuators.

Table 6.1: Dimensions of the Si membrane with piezoelectric actuators presented in Figure 6.4

Description	Value [μm]
d_{dpm}	1500
t_{si}	2
t_{PTZ}	0.400
w_{PZT}	100
r_{in}	525
r_{out}	650

Table 6.1 shows the dimensions for geometries used in the FEA. The simulated diaphragm consists of a 400-nm-thick PZT layer residing on top of a 2-μm-thick (100) Si layer. The large deformation option in ANSYS was enabled to simulate stress-stiffening effects from large strains. PZT-5H properties in

Table 6.2 are used for FEA. Figure 6.5 shows a diaphragm deflection per unit pressure for the diaphragm described in Table 6.1, using ANSYS APDL. In Figure 6.5, the simulated diaphragm compliance at the center C_{mp} is 33.2 nm/Pa.

Table 6.2: PZT-5H properties used for FEA.

Description	Value	Description	Value
C_{11}^E	$127\times10^{+9}$ N/m^2	e_{31}	-6.62 C/m^2
C_{12}^E	$80.2\times10^{+9}$ N/m^2	e_{33}	23.2 C/m^2
C_{13}^E	$84.7\times10^{+9}$ N/m^2	e_{15}	17.0 C/m^2
C_{33}^E	$117\times10^{+9}$ N/m^2		
C_{44}^E	$23.0\times10^{+9}$ N/m^2	$\varepsilon_{11}^S = \varepsilon_{22}^S$	1710
C_{66}^E	$23.5\times10^{+9}$ N/m^2	ε_{33}^S	1430

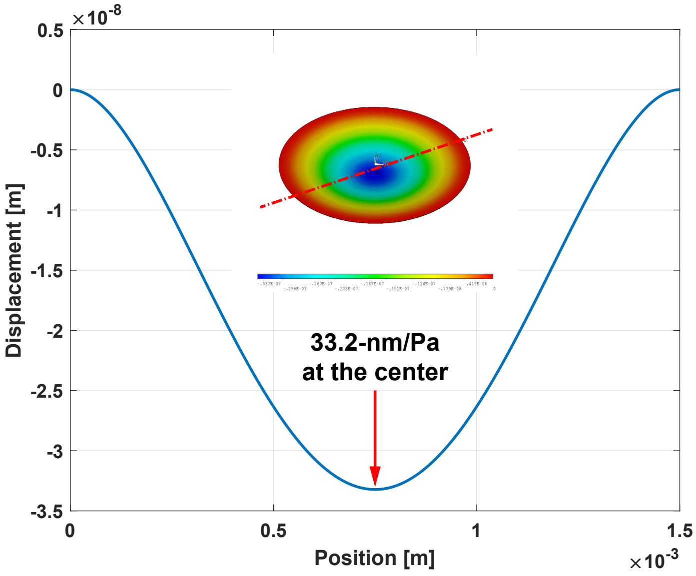

Figure 6.5: Diaphragm deflection profile under 1-Pa input pressure (downward).

Figure 6.6 shows the actuated diaphragm profile applying +1 V to the inner top and outer bottom electrode while the inner bottom and outer top electrode is set to 0 V. In Figure 6.6, the center displacement is simulated as 1.63 μm/V, and the simulated membrane therefore can generate 49.1 Pa/V (= 1.63 μm/V/ 33.2 nm/Pa). In other words, a pressure equivalent to 127.8-dB SPL can be generated with the diaphragm by applying 1-V actuation voltage.

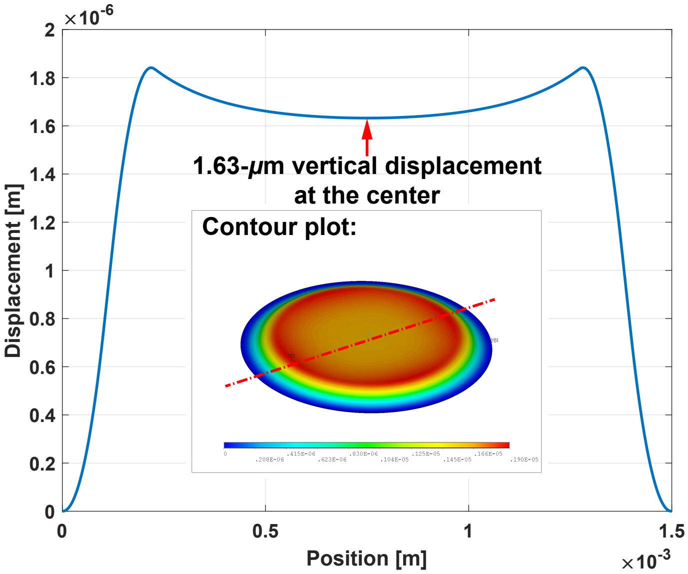

Figure 6.6: Diaphragm deflection profile of the Si diaphragm with piezoelectric actuators with applying 1-V input voltage.

6.3 Design of a Backplate for a Low Flow-Resistance and High Vertical Stiffness

The lowest thermal-mechanical displacement noise can be achieved by minimizing the flow resistance and maximizing the backplate mechanical stiffness. Additional displacement by the compliant backplate results in a higher MDD, and therefore a lower SNR is expected. In this section, a feasibility study of a backplate design is performed. The backplate design utilizes multiple high-aspect ratio spokes to achieve high vertical stiffness via a fabrication technique, known as HEXSIL.

6.3.1 Design of a Minimalistic Backplate with High Mechanical Stiffness

The first prototype backplate described in Chapter 3 and 4, was fabricated using a SOI wafer with a 2-μm-thick device Si layer. Whereas the high-perforation density honeycomb-shaped backplate reduced the squeeze-film damping significantly, the measurement and model revealed a 3-dB noise penalty due to backplate motion. To increase the vertical mechanical stiffness, a backplate design utilizing high-aspect ratio spokes is studied.

The backplate design is illustrated in Figure 6.7. The high aspect ratio spokes support the stationary grating at the center of the backplate in position. Each spoke is 3-μm wide and 16-μm tall and can be modeled as a cantilever beam with a clamped-guided boundary. The stiffness of the clamped-guided beam is computed by,

$$k_m = \frac{12EI}{L^3}, \tag{6.3}$$

where, E is the elastic modulus and I is the area moment of inertia ($= bh^3/12$). From (6.3), the beam stiffness is proportional to h^3, where h is the height

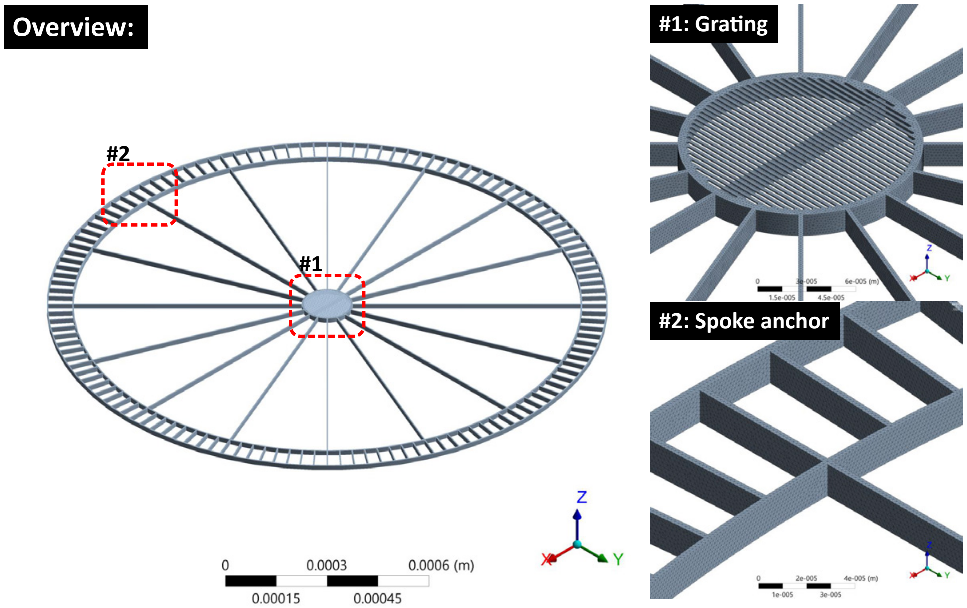

Figure 6.7: 3-D rendering of a minimalistic backplate with high-aspect ratio spokes for FEA.

of each spoke with the fixed beam width b. Thus, if h is increased from 4 μm to 16 μm (i.e., 4×), the stiffness of the spoke in the vertical direction would be increased as much as 64 times. The fundamental resonance and static deflection under 1-Pa input pressure are simulated with two backplate designs incorporating 4-μm and 16-μm height spokes using ANSYS Workbench Mechanical using mechanical properties of p-Si. The rest of the backplate dimensions are the same.

Figure 6.8 presents the simulated first mode shapes of the backplates with 4-μm and 16-μm-tall spokes, respectively. The resonance frequencies are simulated as 14.07 kHz and 61.27 kHz for 4-μm and 16-μm height spoke designs respectively. The 4× higher resonance frequency is expected. The mass of the backplate is increased four times as the backplate thickness is increased from 4 μm to 16 μm, and the stiffness is increased 64×. Therefore 4× higher resonance frequency is anticipated by $f_n = (1/2\pi)\sqrt{k_m/m_{eq}}$.

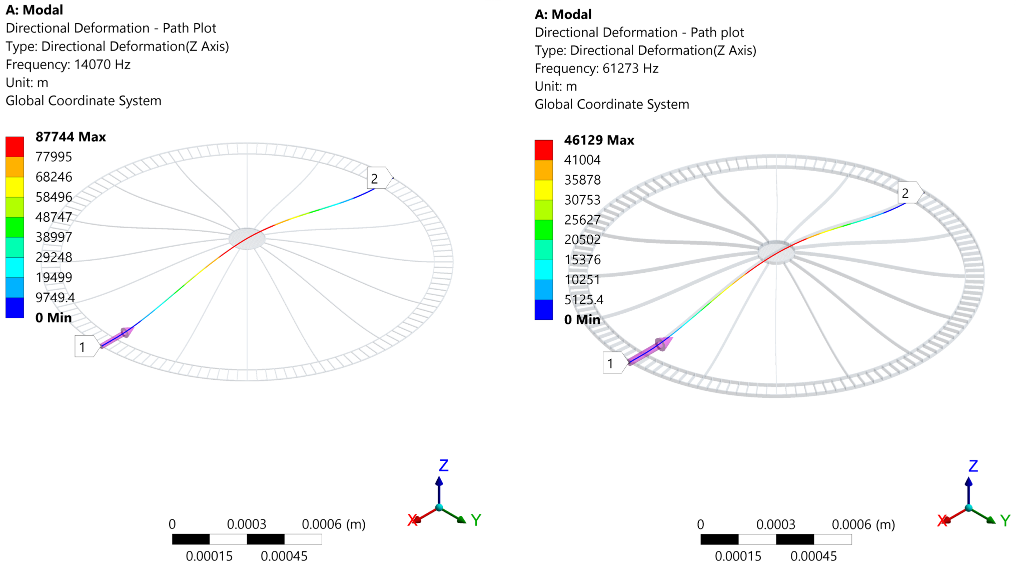

(a) (b)

Figure 6.8: Comparison of the first modal frequency from two different spoke heights, 4 μm vs. 16 μm Resonance simulated as 14.1 kHz and 61.3 kHz respectively.

Figure 6.9 shows the static deflection simulation results under 1-Pa pressure applied normal to the top surface. 24.3-nm and 0.359-nm vertical displacement at the center is simulated from the 4-μm- and 16-μm-thick backplate designs respectively, in which the stiffness increase is 67.7×, again close to the expected stiffness improvement (64×).

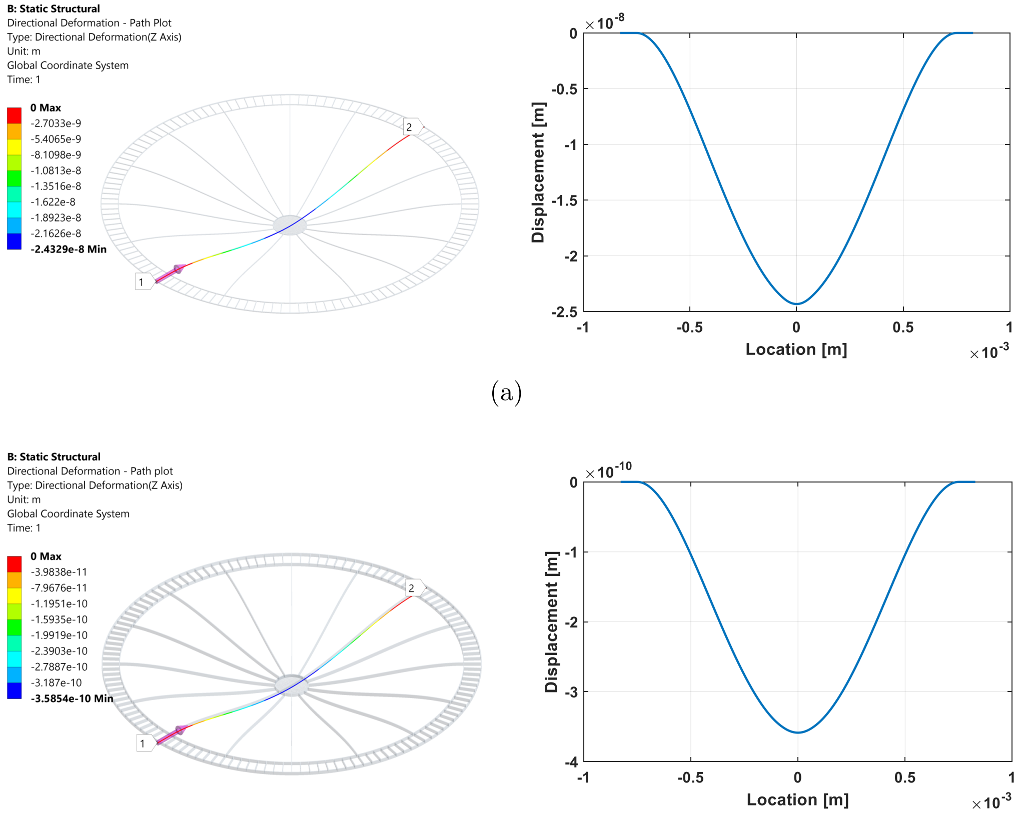

(a)

(b)

Figure 6.9: Comparison of the static deflection profile under 1-Pa static pressure applied to the top surface of the backplate with (a) 4-μm-tall spokes and (b) 16-μm-tall spokes.

To illustrate the additional thermal-mechanical displacement with the simulated backplates, a case with the same 10-nm/Pa diaphragm compliance and backplate-induced noise pressure P_n for both backplates are assumed. Under the conditions, the thermal-displacement noise increase Δd_{tm} can be calculated by,

$$\Delta d_{tm} = \frac{P_n(C_{mp,d} + C_{mp,bp})}{P_n(C_{mp,d})} = \frac{C_{mp,d} + C_{mp,bp}}{C_{mp,d}} \tag{6.4}$$

where, P_n is the input-pressure referred flow resistance in units of Pa/$\sqrt{\text{Hz}}$, and $C_{mp,d}$ and $C_{mp,bp}$ are diaphragm and backplate compliance in units of m/Pa. Using (6.4), Δd_{tm} with the 4-μm and 16-μm-tall backplate increases 3.430× and 1.036× respectively compared to the rigid backplate case.

6.3.2 Fabrication of the Backplate with High Aspect-Ratio Spokes

To achieve a flat surface upon the completion of the backplate and higher vertical stiffness, a fabrication technique used for hexagonal rigid geometries made of silicon thin-film (HEXSIL) is utilized [33] [34]. Figure 6.10 illustrates the HEXSIL process. The key difference of the HEXSIL process, compared to the fabrication using a SOI wafer, is that the high-aspect ratio structures are fabricated not by etching most of the Si, in which the remaining Si becomes the backplate structure, but filling deep, narrow trenches etched by DRIE process via a p-Si low-pressure chemical vapor deposition (LPCVD).

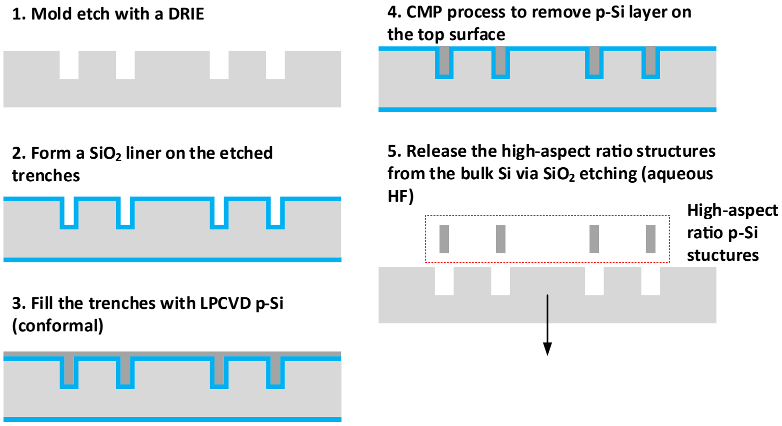

Figure 6.10: Illustration of the HEXSIL fabrication flow.

LPCVD can deposit a highly conformal layer even inside of a deep trench. With the HEXSIL process, a 3-μm-wide spoke is realizable with a deposition of 1.5-μm-thick p-Si layer since the 3-μm-wide trench is filled up from both sides of each trench. Since a uniform layer is formed across the top of the wafer, the HEXSIL process provides a flat surface once the trenches are filled up.

The fabrication of the backplate with high-aspect ratio spokes alone is rather straightforward with a SOI wafer with a 16-μm-thick device Si layer. However, this approach would induce excessive topography on the subsequent features, e.g., optical grating, diaphragm and PZT layer on the diaphragm. For example, the 4-μm-pitch, 800-nm-thick Michelson-type grating can be properly realized when the grating lithography is performed on a flat surface. A highly flattened surface is necessary to avoid undesirable diffraction effect during the photolithography step. The diffraction of the UV light due to uneven contact can lead to a loss of critical dimensions of the grating, which affects the diffracted beam patterns. The diaphragm also must be flat to provide a proper surface to reflect the light back to the photodiodes. Therefore, the fabrication approach with a SOI wafer is therefore not feasible.

6.4 Feasibility Study: Fabrication of a Piezoelectric-Optical MEMS Microphone

6.4.1 Overview

To achieve a force-feedback piezoelectric optical microphone, two essential components are required; the minimalistic backplate and a diaphragm with PZT actuators. To achieve the mechanically rigid but highly perforated backplate, the HEXSIL process is implemented. PZT actuators atop a Si diaphragm are realizable via chemical solution deposition (CSD) process, also known as PZT sol-gel process, with Pt top and bottom electrodes. Table 6.3 shows the list of masks for the fabrication, and Figure 6.11 shows the fabrication flow of a piezoelectric optical microphone. This feasibility study can be separated into two parts; a realization of the backplate and the Si diaphragm with PZT actuators. The high-aspect ratio backplate can be realized by following Step 1 to 7B in Figure 6.11.

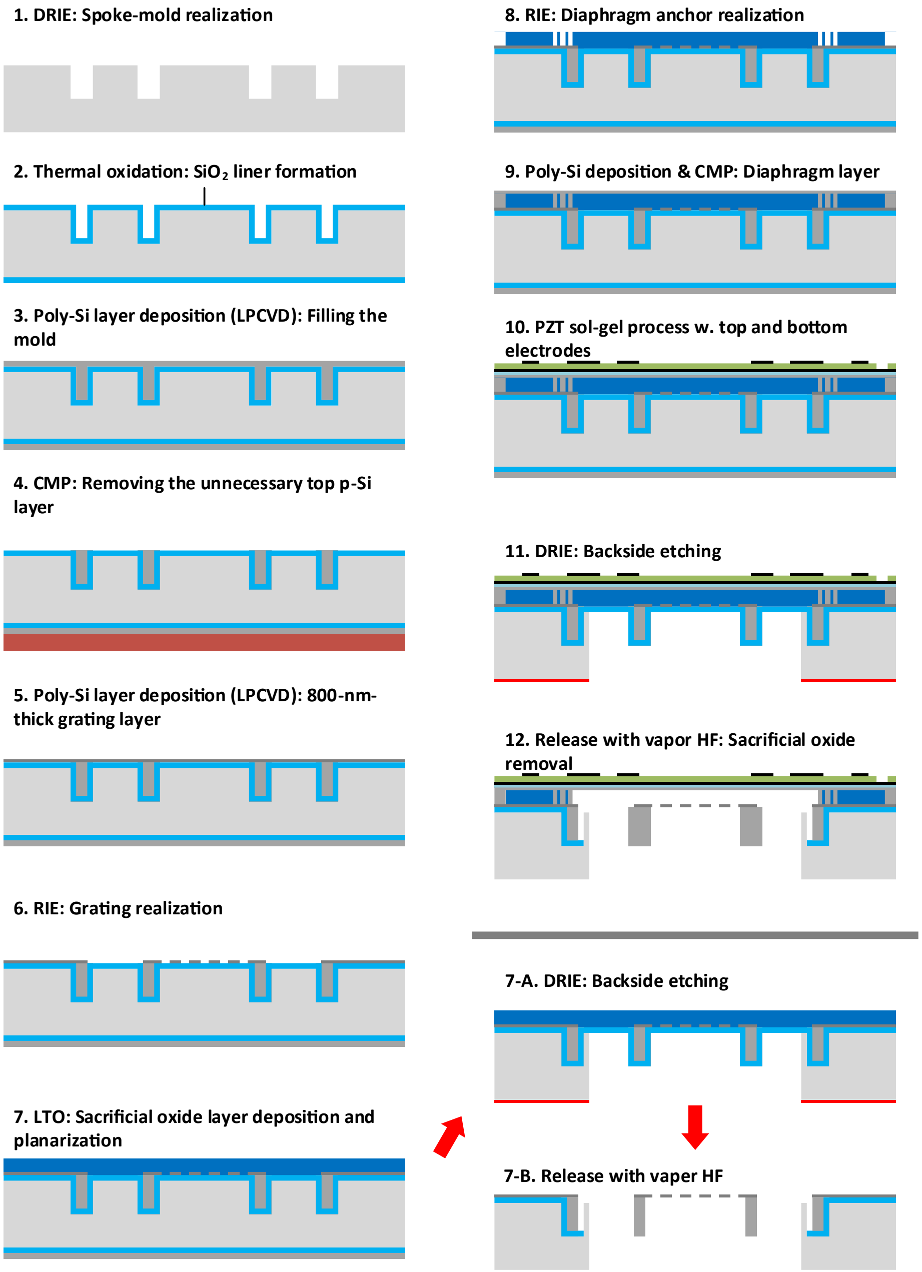

Figure 6.11: A block diagram illustrating the force-feedback operation of piezoelectric optical microphone.

Table 6.3: Masks for a fabrication of piezoelectric optical microphone.

Mask #	Description
1	Spoke etch
2	Grating-layer etch
3	Diaphragm-anchor etch
4	Bottom-electrode lift-off
5	Top-electrode lift-off
6	PZT wet-etch

6.4.2 Fabrication of a Backplate with High Aspect-Ratio Spokes

A fabrication of the minimalistic backplate starts with a piranha clean of a double-side polished (DSP) Si wafer. Piranha solution is a chemical mixture of HCl and H_2O_2, a volume ratio of 2:1, which is effective to remove organic contamination on the wafer. After the piranha clean, the wafer is processed in atomic layer deposition (ALD) tool (Cambridge Nano-tech Savannah) to deposit a 25-nm-thick Al_2O_3 layer. The deposited Al_2O_3 layer is served as a hard mask for the subsequent deep reactive ion etching (DRIE) process, in which narrow and deep HEXSIL molds are realized. A standardized AZ5214-E photoresist (PR) lithography is used to pattern the Al_2O_3 hard mask. Details of the standardized lithography with AZ5214E-IR PR is described in Table 6.4.

After the lithography, the Al_2O_3 layer is etched using an inductively-coupled plasma (ICP) reactive ion etching (RIE) tool (Oxford PlasmaLab 100) with 14-sccm BCl_3 and 6-sccm Ar. Upon the Al_2O_3 layer is successfully etched,

Table 6.4: Masks for a fabrication of piezoelectric optical microphone.

Step	Description	Process condition
1	HMDS priming	2-min priming in 150 °C oven
2	AZ5214E-IR	3000 PRM / 30 sec for 1.46 μm-thick PR followed by a prebake at 110 °C for 50 sec
3	Exposure	Karl Süss MA6 mask aligner with 7.5 mW/cm^2 for 13 sec
4	Development	35 sec in AZ400K:DI water = 1:4 solution

the remaining PR layer is removed using solvents (acetone, methanol, and isopropyl alcohol - IPA), followed by O_2 plasma ashing, using MARCH asher at 300 W. After the remaining PR layer is removed, the patterned features are etched in a DRIE tool (PlasmaTherm DSE) to form 16-μm-deep and 5-μm-wide trenches as shown in Figure 6.12. After the DRIE process, the etched wafer is cleaned again using piranha solution. The remaining Al_2O_3 hard-mask layer is also removed in the cleaning process. The remaining Al_2O_3 hard-mask layer must be removed to guarantee a formation of a conformal 2-μm-thick SiO_2 liner on the entire surface of the wafer in the subsequent thermal-oxidation process.

The 2-μm-thick SiO_2 layer is served as a mold liner to separate the p-Si high-aspect ratio spokes from the bulk Si substrate. The 2-μm-thick SiO_2 layer is formed by a thermal wet-oxidation process at 1050 °C. Since a thermal oxidation is associated with a volume change when Si is oxidized to SiO_2, the original 5-μm-wide trench becomes 3-μm-wide after the oxidation

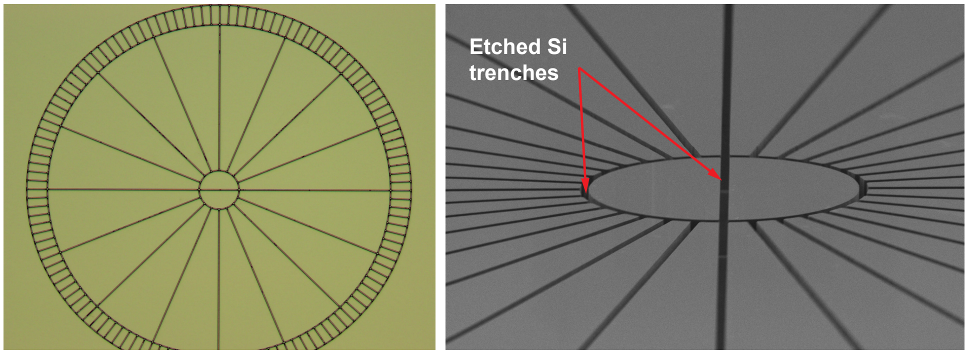

(a) (b)

Figure 6.12: (a) Micrograph and (b) SEM image of the spoke trenches prior to a SiO_2 liner formation.

process. Whereas the original HEXSIL process utilizes the liner as a sacrificial layer to release the high-aspect ratio structure from its mold, the SiO_2 liner in this fabrication serves as an etch stop for a backside DRIE process. Since a selectivity of SiO_2 over Si in a DRIE process is found as 100:1, the 2-μm-thick SiO_2 should be able to protect the backplate structures while etching 200-μm-deep Si. To fill the 3-μm-wide trenches, a 1.5-μm-thick conformal p-Si layer was deposited using LPCVD (Thermotec furnace). The successful filling of the trench is verified as in Figure 6.13.

After the trenches are filled with p-Si layer, the top surface of the wafer is polished via chemical-mechanical polishing (CMP, Westech/IPEC 372M) until the top p-Si layer is completely polished out so that the thermal SiO_2 layer underneath p-Si layer is exposed as shown in Figure 6.14.

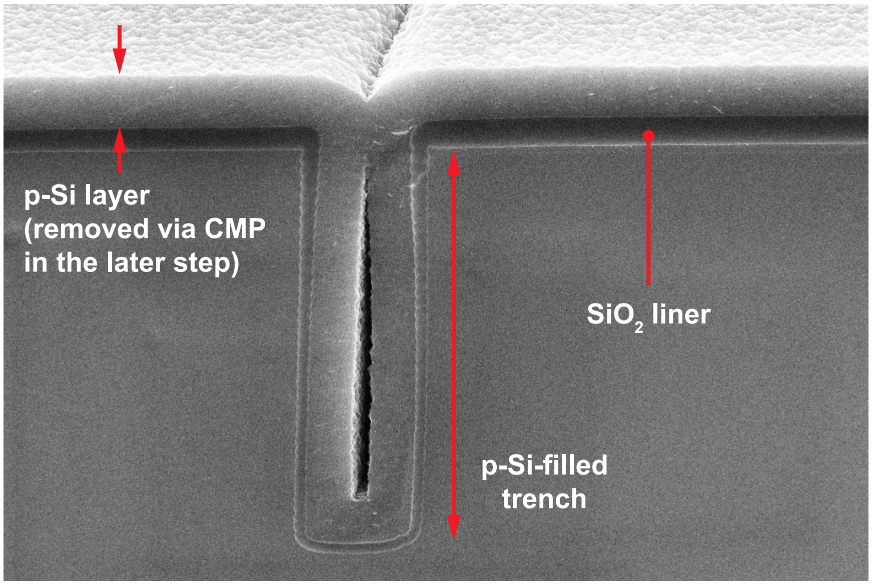

Figure 6.13: Cross-sectional SEM image of a p-Si-filled trench. A void is formed after p-Si layer on each wall close the trench entrance.

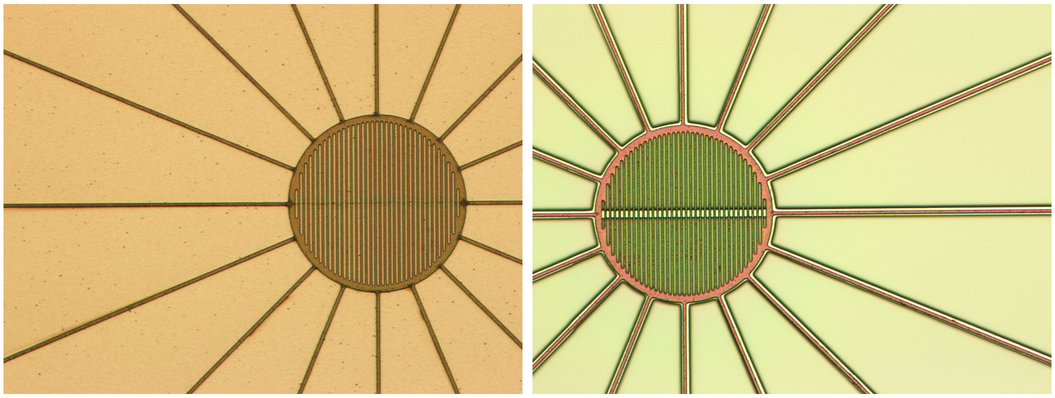
(a) (b)

Figure 6.15: Micrographs of (a) patterned optical grating on the 700-nm p-Si layer with AZ5124E-IR PR and (b) the optical grating after etching the PR patterned p-Si grating layer.

After the p-Si CMP process, an 800-nm-thick p-Si layer is deposited

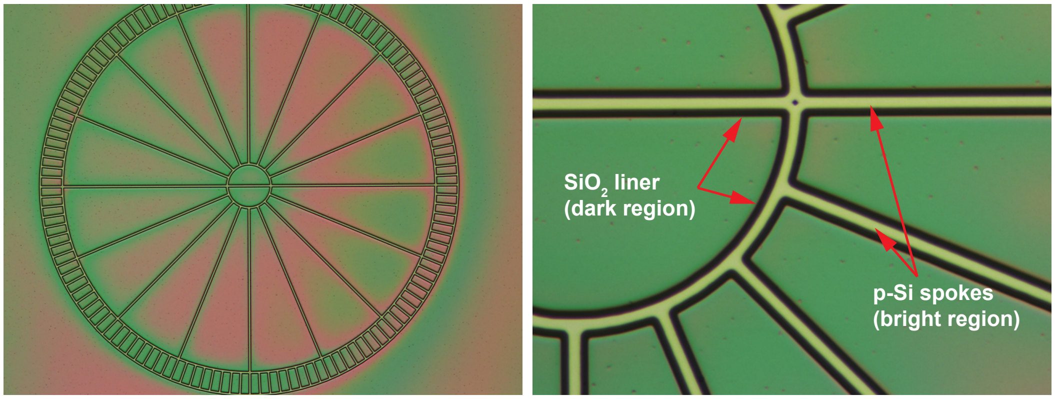

(a) (b)

Figure 6.14: Micrograph and SEM image of the spoke trenches prior to a SiO_2 liner formation.

using LPCVD to pattern a Michelson-type grating. 2-μm-wide grating fingers (4-μm pitch) were patterned using AZ5214E-IR and Karl Süss MA6 aligner by exposing the PR layer for 13 seconds (7.5 mW/cm^2 UV light intensity), followed by a development using a diluted AZ400K developer (1:4 = AZ400K : deionized water). The grating patterned wafer is etched in Oxford PlasmaLab 80+ RIE with a 40-sccm SF_6 gas, and the realized grating is shown in Figure 6.15.

After a grating was realized, a back-cavity is realized via a DRIE process. For this process, a 228-nm-thick Al_2O_3 layer was deposited on the backside of the wafer via ALD to form a hard-mask layer, followed by the hard-mask lithography and etch process used for the earlier trench realization. The successfully realized backplate structure is shown in Figure 6.16.

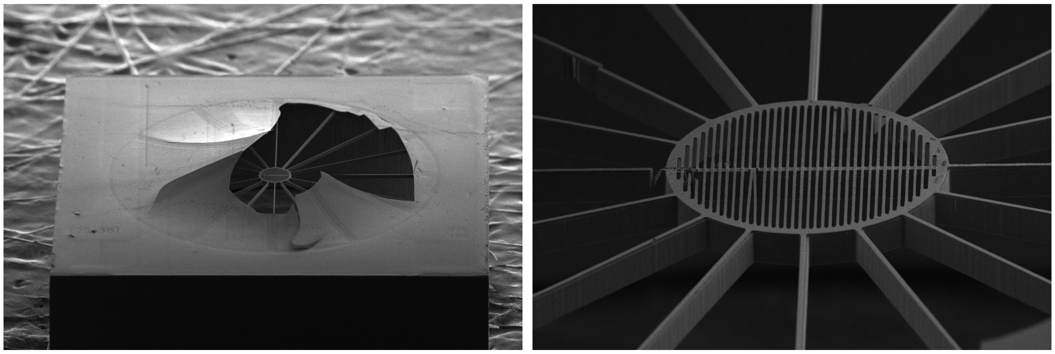

(a)

(b)

Figure 6.16: Micrographs of (a) patterned optical grating on the 700-nm p-Si layer with AZ5124E-IR PR and (b) the optical grating after etching the PR patterned p-Si grating layer.

6.4.3 Fabrication of a Membrane with Piezoelectric Actuators

To explore a feasibility of the force-feedback optical microphone, a Si membrane with a piezoelectric actuator is designed as shown in Figure 6.17 and fabricated using a SOI wafer.

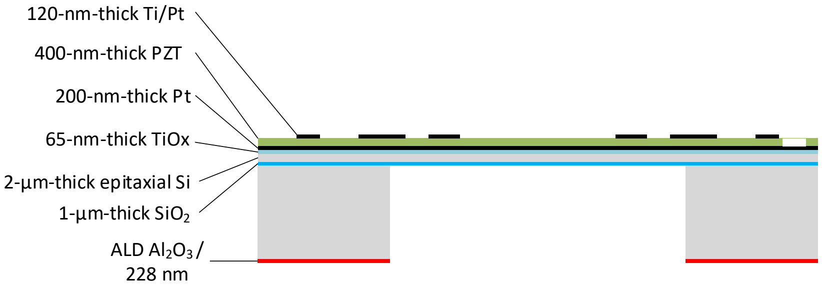

Figure 6.17: A layer stack of a Si membrane structure with piezoelectric actuators.

A SOI wafer with a 2-μm-thick epitaxial Si device layer is used to fabricate a piezoelectric Si diaphragm. A high quality PZT layer can be fabricated when a high-quality seed layer is provided first. On the top side of a SOI wafer, a 50-nm-thick Ti layer is deposited using a KJL sputtering tool at MRC. The deposition condition is listed in Table 6.5.

Table 6.5: Sputtering condition for Ti and Pt layer deposited using a KJL sputtering tool at MRC.

Material	Pressure	Gun type	Power	Temperature	Gas
Ti	7.5 mTorr	DC	300 W	Room temp.	50-sccm Ar
Pt	7.5 mTorr	RF	300 W	500 °C	50-sccm Ar

The deposited Ti layer is thermally oxidized in a kiln at 700 °C under atmospheric pressure for 3 hours to form a TiO_2 film. The TiO_2 layer serves as both an adhesion layer interfacing Si and Pt surface and a diffusion barrier, which prevents Pb diffusion from the PZT layer to Si surface. Ti is also commonly used for a Pt adhesion layer, but a Ti adhesion layer shows instability during a high-temperature annealing process in a PZT sol-gel process, TiO_2 is more suitable for a stable Pt layer during a PZT sol-gel process [35]. After the 3-hour oxidation process, the wafer was kept in the kiln until the wafer is cooled down to a room temperature to avoid any thermal shock on the TiO_2 layer, which may lead to premature cracks on TiO_2 layer. After the Ti-to-TiO_2 conversion process, the SOI wafer is thoroughly cleaned using solvents (acetone, methanol, and isopropyl alcohol), followed by a 5-min O_2 plasma ashing.

After the substrate cleaning, the 200-nm-thick Pt layer is sputtered on the 65-nm-thick TiO_2 layer at 500 °C. High quality (111) Pt is preferred for a PZT sol-gel process to promote desired PZT crystalline direction (100) PZT, which shows a higher than (111) PZT layer [27]. To achieve (111) Pt layer, a RF sputtering was performed at 500 °C as shown in Table 6.5. The crystallinity of the sputtered Pt layer is examined using x-ray diffraction (XRD) tool, Phillips Xpert, prior to a PZT sol-gel process. The 2θ-ω measurement result shows high-intensity (111) and (222) Pt peaks as shown in Figure 6.18. Compared to a Pt layer deposited at a room temperature, followed by a subsequent annealing at 300 °C for 3 hours, a Pt layer deposited at 500 °C shows higher peak without having spurious non-desirable Pt crystalline orientations observed in the former case.

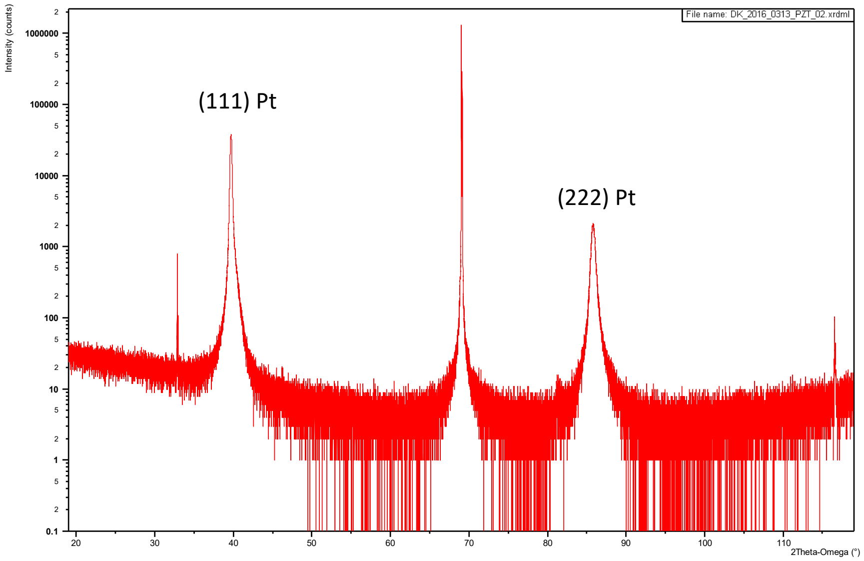

Figure 6.18: XRD 2θ-ω measurement on the 200-nm-thick Pt/65-nm-thick TiO_2/2-μm thick Si substrate. (111) and (222) Pt peaks are showing a high crystallinity of Pt layer sputtered at 500 °C

The SOI wafer with a highly (111)-oriented bottom Pt layer is cleaned again with solvents and O_2 plasma followed by a PZT sol-gel process. A commercial PZT sol-gel solution (Mitsubishi Materials, PZT-N) is used for the PZT sol-gel process. About 2-mL PZT-N solution is dispensed onto the Pt deposited wafer, using a syringe with a 0.25-μm PTFE filter. Then the wafer is spun at 4500 RPM for 100 sec to evenly coat the dispensed PZT sol-gel solution onto the platinized wafer. The solvent in the spin-coated PZT sol-gel solution is removed on a 70 °C hotplate for 2 minutes. After solvent is removed, the first pyrolysis step is performed at 300 °C for 5 min and the second pyrolysis step is performed at 450 °C subsequently for 5 min on hotplates. After the second pyrolysis step, another PZT sol-gel solution is spun on the wafer to achieve a total of a 418-nm-thick PZT layer. After the pyrolysis steps, a high-temperature annealing at 700 °C is performed for 30 mins. During the high-temperature annealing step, the amorphous phase PZT layer changes into pyrochlore firstly and then is finally converted to perovskite phase [36]. Finally, a 400-nm-thick PZT layer was obtained by repeating the PZT layering procedure.

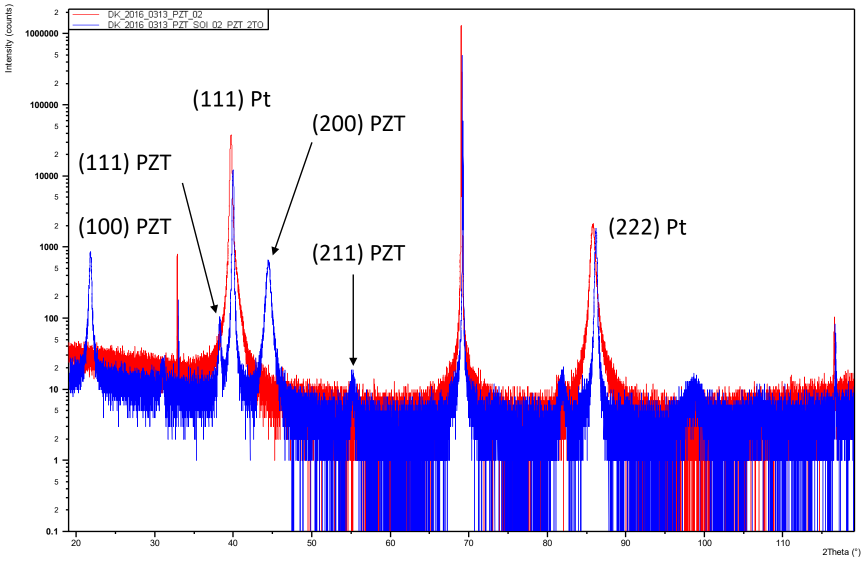

Figure 6.19: A compared XRD result before and after a PZT sol-gel process on the (111) Pt layer. The XRD result clearly shows that (100) and (200) PZT peaks while a smaller (111) PZT peak is also shown near (111) Pt peak.

After achieving a 400-nm-thick PZT layer, another XRD is performed on the PZT layer to confirm that the desired (100) PZT is formed on the bottom Pt layer. The XRD result shown in Figure 6.19 indicates that the PZT sol-gel process achieved the desired PZT crystalline orientation. It is also observed that the full width at a half maximum (FWHM) of the bottom-electrode

Pt layer is reduced after the PZT sol-gel process. The reduced FWHM indicates that the crystallinity of the bottom Pt layer is increased through the PZT sol-gel process (mainly due to the high-temperature PZT annealing process at 700 °C). This indicates that the crystallinity of the bottom Pt layer can be improved further prior to a PZT sol-gel process by performing additional annealing at a temperature higher than 500 °C.

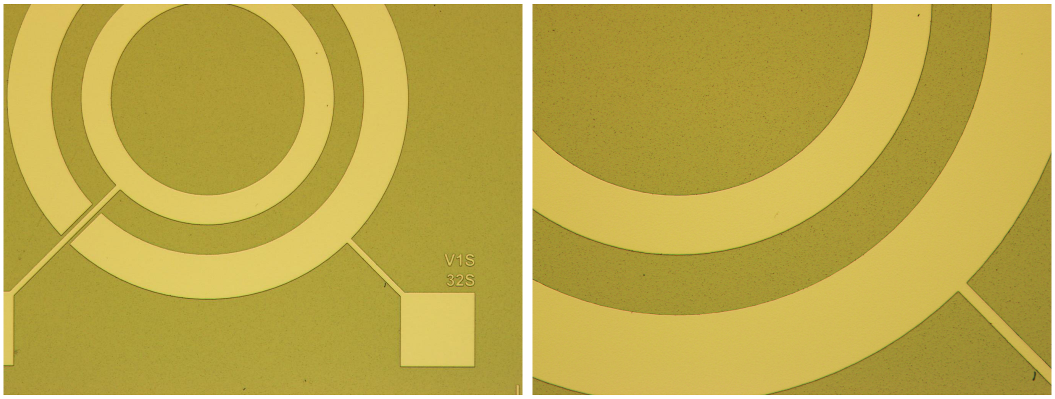

(a) (b)

Figure 6.20: Micrographs of a 2-μm Si diaphragm with 400-nm-thick PZT-film ring-shaped actuators.

After the XRD measurement, top electrodes are patterned on the PZT film using AZ5214E-IR photoresist, which is spin-coated at 3000 RPM for 30 seconds to achieve a 1.46-μm-thick layer. Once the electrodes are patterned onto the PR layer using Karl Süss MA6 mask aligner, a 40-nm-thick Ti layer is sputtered as an adhesion layer and 120-nm-thick Pt layer is sputtered subsequently without breaking the vacuum in the KJL sputtering tool. A lift-off process is performed with the Ti/Pt covered wafer. The result is shown in

Figure 6.20.

After the lift-off process, a PZT wet-etching process is performed to open a bottom bondpad by etching the existing PZT layer. AZ9260 PR is used to form a masking layer against PZT etchant. Details of a lithography with AZ9260 PR is described in Table 6.6. After the lithography process, the patterned AZ9260 PR is hard-baked at 145 °C to achieve maximum chemical resistance in the subsequent PZT wet-etch process. The reflow temperature of AZ9260 is approximately 110 °C, and thus the AZ9260 PR is heavily reflowed after a 5-min hard-bake step. The hard-baked PR is prone to cracking due to thermal shock after the hard bake. Thus, the wafer is naturally cooled down on the hotplate for 20 minutes.

Table 6.6: Standardized recipe or AZ9260 PR.

Step	Description	Process condition
1	HMDS priming	2-min priming in 150 °C oven
2	AZ5214E-IR	2000 PRM / 30 sec for 9.6 μm-thick PR followed by a prebake at 110 °C for 240 sec
3	Rehydration	Submerging into DI wafer for 15 min
4	Exposure	Karl Süss MA6 mask aligner with 7.5 mW/cm^2 for 125 sec
5	Development	300 sec in AZ400K:DI water = 1:4 solution

The PR-patterned wafer was subsequently submerged into a PTFE beaker with a PZT etchant for 1 minute 30 seconds. A PZT etchant is prepared with 200 mL of deionized water, 20 mL of hydrochloric acid, and 2 mL of hydrofluoric acid. After a successful PZT wet-etch process, the back cavity was etched using a DRIE process, which is the same process described in the backplate fabrication. The embedded oxide layer (1-μm-thick SiO_2) was used for an etch stop during the DRIE process, and it was subsequently removed with vapor HF at a room temperature.

6.4.4 Electrical Admittance Spectroscopy of the PZT Actuators

After the completion of the piezoelectric Si membrane, each membrane is singulated using ADT 7100 dicing machine. Then a singulated die is mounted on a PCB, and, electrical admittance spectroscopy was performed to measure the capacitance value of the PZT elements on the membrane, which provides a preliminary evidence of a successful fabrication of piezoelectric actuators [37].

Table 6.7: Results from the electrical admittance spectroscopy with the fabricated Si membrane with dual-ring-shaped PZT actuators.

Sample	Measured capacitance (nF)	Electrode area (m^2)	PZT thickness (nm)	Calculated $\epsilon_{33,f}$
1	4.58	6.27×10^{-7}	418	702
1	9.41	3.08×10^{-7}	418	709

Table 6.7 summarizes the electrical admittance spectroscopy results. In Table 6.7, the fabricated PZT film thickness and electrode area are determined using a surface profiler and computer-aided design (CAD) software respectively. The relative dielectric constant $\epsilon_{33,f}$ of the PZT film is back-calculated from

the measured capacitance and device dimensions, in which the measured $\epsilon_{33,f}$ values are within the typical range reported in [27].

6.4.5 Remnant Polarization Measurement with Sawyer-Tower Circuit

The remnant polarization of a fabricated PZT film can be measured using a Sawyer-Tower circuit shown in Figure 6.21. A higher remnant polarization indicates a high-quality piezoelectric film.

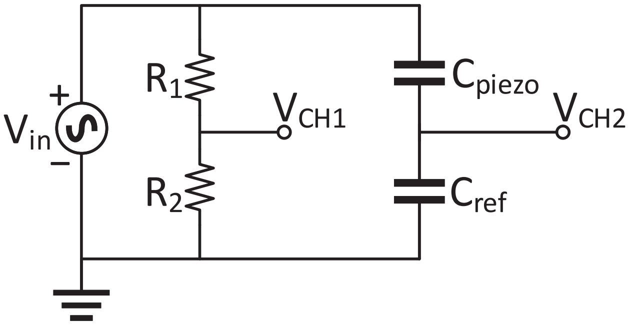

Figure 6.21: Sawyer-Tower circuit diagram used for a remnant polarization measurement.

For the polarization measurement, zero-biased triangular signal V_{in} is used for the input signal. The input voltage V_{in} is applied across the two capacitors, C_{piezo} and C_{ref}. V_{in} is measured using the voltage divider formed by R_1 and R_2, i.e., V_{CH1}. The charges generated from the piezoelectric film due to V_{in} the input voltage flow through C_{ref}. Measuring the voltage across C_{ref}, the amount of total charges can be easily computed using $Q_{meas} = C_{ref}V_{CH2}$. It is important to select the reference capacitor following $C_{ref} \gg C_{piezo}$ so that

V_{in} is approximately the same as V_{piezp} as shown in (6.5).

$$V_{piezo} = \frac{C_{ref}}{C_{ref} + C_{piezo}} V_{in} = \frac{C_{ref}}{C_{ref} + C_{piezo}} (2V_{CH2}) \tag{6.5}$$

With a known electrode area, the polarization in units of μC/cm^2 can be obtained by $P_r = Q_{meas}/A$. Note that a breakdown on the PZT films in Figure 6.22 was occurred when the applied e-field across the PZT film exceeds 250 kV/cm. The measured remnant polarization, $2P_r$ is approx. 15 μC/cm^2, which is slightly lower than the values reported in [38] [39].

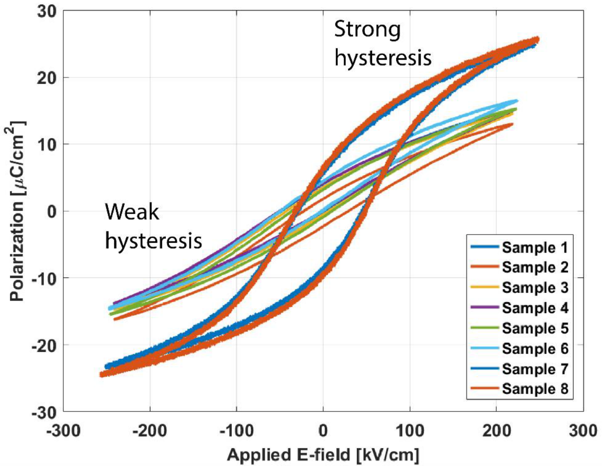

Figure 6.22: Remnant polarization measurements from different samples. The stronger hysteresis is a good indication of a properly formed ferroelectric material and also good piezoelectric properties.

6.4.6 Diaphragm Actuation using the Built-in Piezoelectric Actuators

Figure 6.23 shows a frequency response plot of a prototype piezoelectric optical microphone. The membrane was actuated with the piezoelectric actuator while the diaphragm motion was measured using the built-in grating and discrete optoelectronics similar to Figure 4.3.

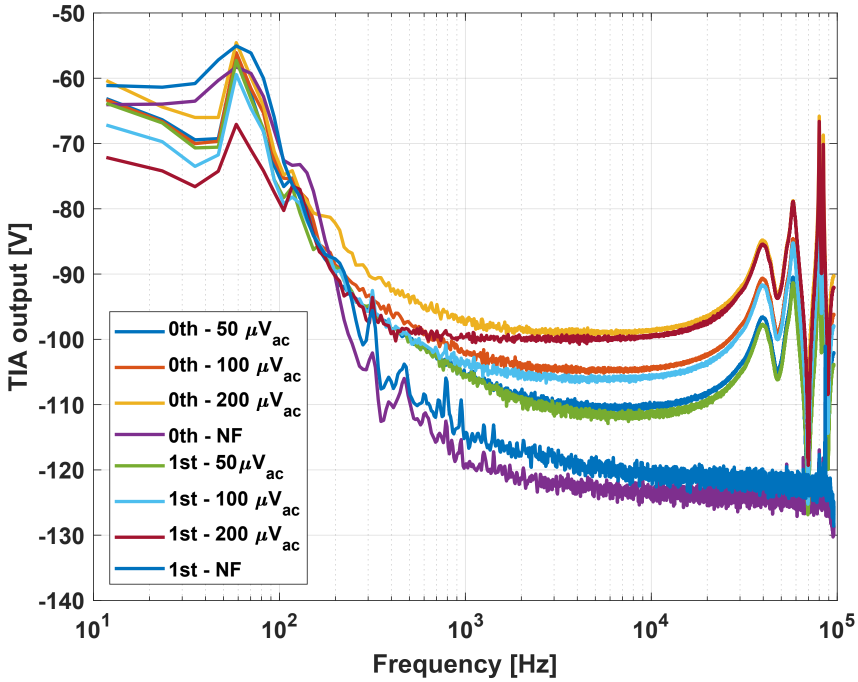

Figure 6.23: A frequency response plot of the piezoelectric optical microphone by actuating the outer PZT actuator on the diaphragm. The diaphragm displacement was measured via interferometric readout.

The TIA output was measured using a PrismSound dScope Series III FFT analyzer, while the diaphragm is being actuated using the bin-centers function, which is a noise-like multi-tone stimulus at equal amplitudes. For the amplitude for bin-centers stimulus, 50, 100, and 200 μVrms are used. The diaphragm resonance is observed at 40 kHz in Figure 6.23.

Although Figure 6.23 verified the piezoelectric actuators on the prototype membrane is functional, a single-tone input voltage at 5 kHz and 10 kHz measurement with Polytec MSA-050 surface laser Doppler vibrometer (sLDV) revealed that the displacement per voltage is 16.7 nm/V, which is significantly lower (100×) than the simulated center displacement at the center, 1.63 μm/V. The lower actuation can be explained by two reasons. The first reason is explained by the measured diaphragm resonance is 76.5 kHz as shown in Figure 6.24. The measured resonance is 6.27× higher than the simulated membrane resonance, 12.2 kHz.

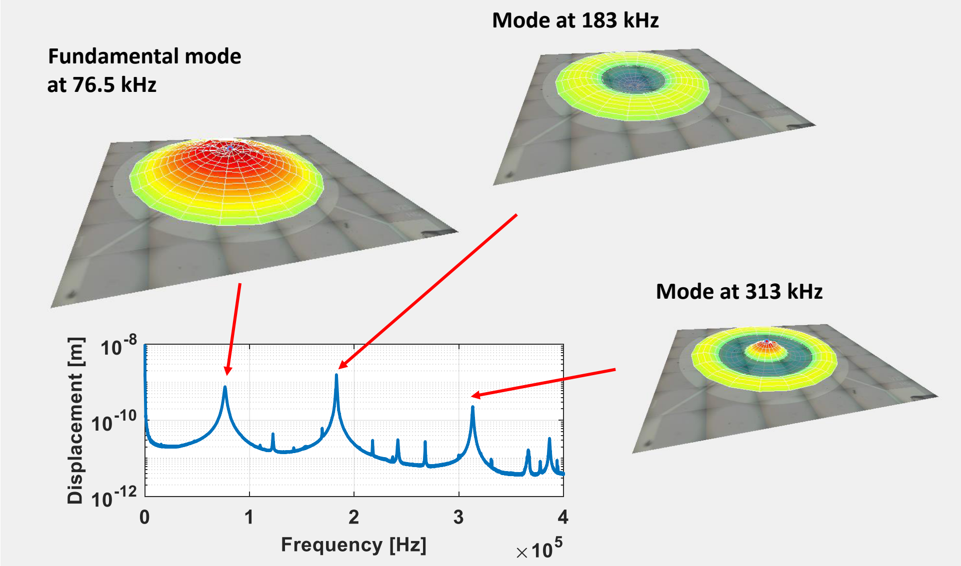

Figure 6.24: Measured diaphragm mode shapes including the fundamental mode at 76.5 kHz using Polytec MSA-050 surface-scanning LDV.

The 6.27× higher resonance indicates the prototype membrane has a 39.2× higher stiffness than the simulated diaphragm when assuming the same effective diaphragm mass for both cases. The stiffer diaphragm is caused by the residual stress on the diaphragm. The PZT sol-gel process is performed up to 700 °C, which induces significant thermal stress on the diaphragm. The second reason is possibly due to the lower actuation constant by the piezoelectric actuators. The actuation performance expects to be improved with a further optimized PZT sol-gel process, i.e., improving the remnant polarization $2P_r$.

6.5 Summary

In this chapter, the feasibility of a piezoelectric optical microphone is studied. The feasibility study focuses on two key components: a Si membrane with piezoelectric actuator and a minimalistic backplate with high aspect-ratio spokes. A Si membrane with a piezoelectric actuator is studied in order to increase the microphone DR beyond the intrinsic DR governed by the optical readout system. The closed-loop operation of a piezoelectric optical microphone is simulated based on FEA and lumped parameter model. The study demonstrated the possibility of a closed-loop optical microphone with a wider DR using a piezoelectric actuator on top of the pressure-sensitive membrane.

It is critical to realize a minimalistic backplate with a high mechanical stiffness in the vertical direction. Both conditions are important to achieve a low-noise optical microphone by reducing the flow resistance induced by the presence of the backplate and relative displacement between the fixed grating and diaphragm. A high vertical stiffness is achieved using high aspect-ratio spokes.

Finally, the minimalistic backplate and Si membrane with piezoelectric actuators and were fabricated as a part of the feasibility study. The minimalistic backplate was successfully realized using HEXSIL technique. In case of the Si membrane with piezoelectric actuators, the fabricated membrane was able to deform as input voltage changes, but the high tensile stress induced by the PZT sol-gel process stiffened the diaphragm significantly. A further study and process optimization would be required to avoid the high tensile stress so that a higher displacement throw can be achieved by the piezoelectric actuators.

Finally, the single-chip piezoelectric optical microphone was fabricated, and the prototype was tested using a discrete optical readout module. The single-chip device also showed a displacement much less than anticipated due to the residual stress and lower-quality PZT film due to the improper seed layer formation on the rough p-Si membrane. However, the feasibility study demonstrated the possibility of the force-feedback optical microphone using a piezoelectric actuator.

Chapter 7

Conclusion and Future Work

7.1 Conclusion

In this research work, the design path to achieve a MEMS microphone with sub 15-dBA noise floor or 79-dB SNR is presented. The optical microphone utilizes a phase-sensitive grating to form an interferometer to detect the diaphragm deflection caused by input sound pressure. Since active capacitance is no longer a limiting design parameter for optical microphone, the perforation density on the backplate can be maximized to reduce the squeeze-film air damping.

In the preliminary work, a prototype high perforation density backplate with an optical grating was successfully fabricated using a SOI wafer, and the flow resistance of the fabricated backplate was simulated with a commercial FEA package and verified experimentally. The fully-packaged prototype optical microphone was tested against five commercial capacitive MEMS microphones and measured as 72-dB SNR, which is approximately 6-dB better than state-of-the-arts. The lumped-parameter network model was successfully verified with the measured prototype noise spectrum.

The verified optical microphone model is used to perform design of experiments. In the DoEs, various system parameters, including diaphragm compliance, back-cavity volume, and electrical power budge, were perturbed to show design implications, which must be understood to achieve sub 15-dBA noise floor.

Finally, a feasibility study was performed to explore the concept of a force-feedback optical microphone to improve AOP. The first part of the feasibility study was focused on a Si membrane with piezoelectric film actuators. To extend the intrinsic DR of an optical microphone which is defined by the diaphragm compliance and the wavelength of VCSEL, the diaphragm must be able to counter-balance the input sound pressure, which in-turn extends the intrinsic DR. A piezoelectric-based Si membrane is investigated rather than electrostatic actuation. Piezoelectric actuator directly implemented on a diaphragm provides a linear, strong, bi-directional actuation compared to electrostatic actuation, in which the force is non-linearly varied as the distance and voltage change. A clamped Si diaphragm with a 400-nm-thick PZT film was successfully fabricated. The second part of the feasibility study is focused on a minimalistic backplate with a high vertical stiffness. Instead of a SOI wafer used for the backplate fabrication in the preliminary work, a backplate was successfully fabricated with a technique, known as HEXSIL. In the feasibility study, a backplate with 15.8-μm-tall, high-aspect ratio spokes (approximately 5) was successfully realized.

7.2 Contribution

7.2.1 Flow-Resistance Simulation using CFD

One of the key successes is that the flow resistance of a complicated backplate structure is simulated successfully using a commercial CFD software, ANSYS Fluent. Evaluating a flow resistance induced by squeeze-film air damping between a membrane and backplate is critical to assess a noise floor of a MEMS microphone as the flow resistance is one of the major noise contributors. The simulated flow resistance with a prototype backplate design was verified with a fabricated prototype backplate, which was paired with a rigid mirror to observe the backplate behavior without concerning about the diaphragm dynamics. The successful verification of the flow-resistance modeled using a CFD package plays a key role to design a minimalistic design of a backplate that leads to an optical microphone with sub 15-dBA noise floor.

7.2.2 Full System Model of an Optical Microphone via Lumped-parameter Network Model

A full system model of an optical microphone is necessary to simulate not only a frequency response function, but also a noise floor taking into account acoustical effects of microphone packaging. The dynamics of the entire optical microphone including acoustical effect due to its packaging is simulated using a lumped-parameter network model. To reflect accurate system behavior, critical parameters are simulated using FEA, such as compliance and resonance frequency of the diaphragm and backplate. The resultant lumped-parameter model successfully predicted a system response and noise floor of a prototype.

7.2.3 Design Path for Optical Microphones with a Sub 15-dBA Noise Floor through Design of Experiments

To understand the system behavior, the verified lumped parameter model was used to perform a series of design of experiments. In the DoEs, effects of the diaphragm compliance, back-cavity volume, electrical power budget to SNR and AOP were studied. For a smaller microphone package, a more compliant diaphragm and better MDD are must to achieve a high SNR. However, the compliant diaphragm reduces the AOP inevitably.

7.2.4 Successful Fabrication of a Backplate with an Optical Grating and High-Aspect Ratio Spokes and a Si Membrane with a PZT Actuator for a Higher AOP Performance

The backplate design used in the DoE utilizes even higher perforation density to achieve 15-dBA noise performance whereas a high vertical stiffness is required to suppress the relative motion. Compared to the first prototype backplate fabricated during the preliminary study, the backplate proposed in the DoE requires high-aspect ratio spokes to fulfill high perforation density and vertical stiffness. The designed minimalistic backplate with high-aspect ratio ribs are successfully fabricated using a fabrication technique developed for a HEXSIL structure.

The other success of the feasibility study, is a realization of a Si membrane with piezoelectric actuators. Actuation of the fabricated membrane is verified, but the amount of displacement was less than anticipated. A high tensile residual stress from the PZT sol-gel process is the primary reason for the low membrane displacement. Instead of a clamped diaphragm, a spring-mounted membrane design would be one of the possible solutions. A further optimization of the PZT sol-gel process is required, including a formation of a high-quality seed layer to produce a higher remnant polarization.

7.3 Future Work

In this research work, the full system model of an optical microphone was explored to achieve a noise floor below 15 dBA, and two key components were fabricated at MRC at The University of Texas at Austin A backplate with high-aspect ratio spokes using HEXSIL process for an extremely low flow resistance and high vertical stiffness and Si membrane with PZT actuators for higher actuation force to accomplish a higher AOP separately. The PZT membrane fabricated in this work revealed that the PZT film induced high tensile stress results in a much stiffer diaphragm, which affects the displacement sensitivity adversely and therefore the noise performance is also degraded. Therefore, a further study will be required to achieve a compliant membrane with piezoelectric actuators that can achieve both a low noise floor and strong actuation to achieve a high AOP.

Finally, a simulation for the force-feedback optical microphone should be developed to model the force-feedback operation and its noise floor. Due to the nature of a closed-loop system, the apparent system compliance over the target frequency bandwidth will be lowered, while the stiffening effect inturn achieves a higher AOP level. Therefore, it is important to begin with a sufficiently high diaphragm compliance with high actuation force so that the force-feedback does not adversely affect the noise level.

Appendices

Appendix A

Lumped Parameter Model

The equivalent circuit model shown in Figure A.1 can be analyzed using the mesh current analysis, commonly used for electric circuit analysis.

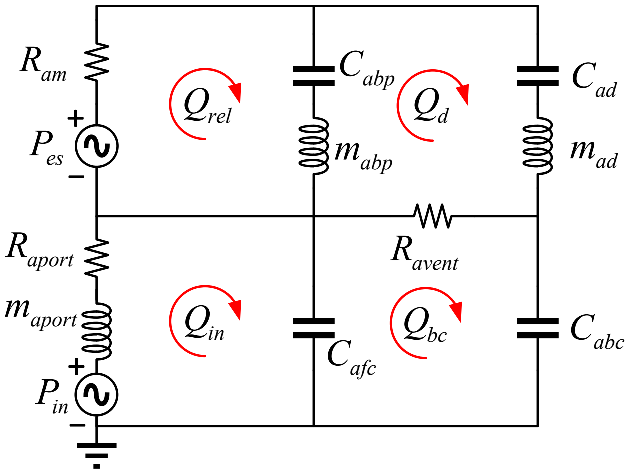

Figure A.1: Network model of the optical microphone for frequency response analysis in acoustical domain.

All the impedances of the MEMS structure in the mechanical domain in units of N·s/m are converted to values in the acoustical domain in units of N·s/m^5 or Pa·s/m^3 by the following relationship.

$$Z_{am} = \frac{Z_m}{A_{eff}^2} = \frac{Z_m}{(\beta A)^2} \tag{A.1}$$

As a result, m_d, C_d, m_{bp}, C_{bp}, and R_m are converted to m_{ad}, C_{ad}, m_{abp}, C_{abp}, and R_{am} respectively.

For noise floor analysis, all the external inputs, such as input sound pressure P_{in} and electrostatic actuation P_{es} are set to zero in Figure A.1, and the thermal-mechanical noise sources are added to the network model as shown in Figure A.2. The equivalent circuit model in the acoustical domain with noise sources is shown in Figure A.2.

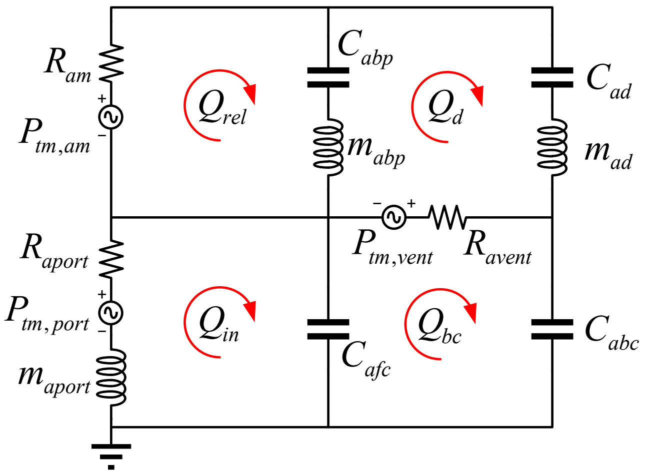

Figure A.2: Network model of the optical microphone for noise analysis in acoustical domain.

Three damping components exist in the network model shown in Figure A.2, which are the inlet port acoustic resistance, R_{aport}, the flow resistance due to the squeeze-film damping effect, R_{am}, and the vent acoustic resistance, R_{avent}. The corresponding pressure noises are computed by,

$$P_{tm,port} = \sqrt{4k_b T R_{aport}} \tag{A.2}$$

$$P_{tm,am} = \sqrt{4k_b T R_{am}} \tag{A.3}$$

$$P_{tm,vent} = \sqrt{4k_b T R_{avent}} \tag{A.4}$$

where, k_b is the Boltzmann constant, and T is room temperature with units of Kelvin. A pressure noise source (equivalent input-referred noise) would be used individually in a noise analysis while other sources are set to zero to evaluate the output-referred noise (thermal-mechanical displacement) due to each pressure noise sources. The displacement noise d_{tm} of the overall MEMS microphone package can be determined by evaluating Q_{rel} in Figure A.2. From the network model in Figure A.2, four loop current equations are obtainable for the mesh current analysis as shown in below.

$$\left(Z_{aport} + \frac{1}{j\omega C_{afc}}\right) Q_{in} - \frac{1}{j\omega C_{afc}} Q_{bc} = P_{tm,port} \tag{A.5}$$

$$\left(Z_{abp} + R_{am}\right) Q_{rel} - Z_{abp} Q_d = P_{tm,am} \tag{A.6}$$

$$- Z_{abp}Q_{rel} + \left(Z_{ad} + Z_{abp} + R_{avent}\right) Q_d - R_{avent}Q_{bc} = -P_{tm,am} \tag{A.7}$$

$$- \frac{1}{j\omega C_{afc}}Q_{in} - R_{avent}Q_d + \left(\frac{1}{j\omega C_{afc}} + R_{avent} + \frac{1}{j\omega C_{abc}}\right) Q_{bc} = P_{tm,vent} \tag{A.8}$$

Note that the acoustic inlet-port impedance Z_{aport} is given by,

$$Z_{aport} = R_{aport} + j\omega m_{aport} \tag{A.9}$$

where, R_{aport} is the acoustic port resistance, and m_{aport} is the acoustic mass. The acoustic impedances of the diaphragm and backplate, Z_{ad} and Z_{abp} are defined as follows.

$$Z_{ad} = j\omega m_{ad} + \frac{1}{j\omega C_{ad}} \tag{A.10}$$

$$Z_{abp} = j\omega m_{abp} + \frac{1}{j\omega C_{abp}} \tag{A.11}$$

Finally, the set of linear equations forms a matrix to solve the equations for volume flow rates as shown in (A.12), and the matrix can be solved using MATLAB.

$$\begin{bmatrix} Z_{aport} + \frac{1}{j\omega C_{afc}} & 0 & 0 & -\frac{1}{j\omega C_{afc}} \\ 0 & Z_{abp} + R_{am} & -Z_{abp} & 0 \\ 0 & -Z_{abp} & Z_{ad} + Z_{abp} + R_{avent} & -R_{avent} \\ -\frac{1}{j\omega C_{afc}} & 0 & -R_{avent} & \frac{1}{j\omega C_{afc}} + R_{avent} + \frac{1}{j\omega C_{abc}} \end{bmatrix} \begin{bmatrix} Q_{in} \\ Q_{rel} \\ Q_d \\ Q_{bc} \end{bmatrix} = \begin{bmatrix} P_{tm,port} \\ P_{tm,am} \\ -P_{tm,am} \\ P_{tm,vent} \end{bmatrix} \tag{A.12}$$

First, the thermal-mechanical noise induced by the inlet-port acoustic resistance can be selectively obtainable by setting the noise source vector $\begin{bmatrix} P_{tm,port} & P_{tm,am} & -P_{tm,am} & P_{tm,vent} \end{bmatrix}^T$ to $\begin{bmatrix} P_{tm,port} & 0 & 0 & 0 \end{bmatrix}^T$. Next, the thermal-mechanical noise due to the flow resistance induced by the backplate geometry and the viscous air flow at the gap between the diaphragm and the grating area is computed by setting the source vector to $\begin{bmatrix} 0 & P_{tm,am} & -P_{tm,am} & 0 \end{bmatrix}^T$. Finally, the acoustic vent resistance is the last component that induces displacement thermal-mechanical noise. The source noise vector is $\begin{bmatrix} 0 & 0 & 0 & P_{tm,vent} \end{bmatrix}^T$. From each set of equations with a different noise source vector, a resultant relative volume flow rate Q_{rel} is obtainable. The relative volume flow rate Q_{rel} is used to compute the thermal-mechanical displacement noise at the center of the diaphragm.

$$d_{rel} = \frac{Q_{rel}}{A_{eff,d}} \tag{A.13}$$

where, $A_{eff,d}$is the effective area of the diaphragm, which is computed by βA_d, and A_d is the actual diaphragm area. Finally, each thermal-mechanical displacement noise d_{rel} due to $P_{tm,port}$, $P_{tm,am}$, and $P_{tm,vent}$ is summed to evaluate the overall thermal-mechanical displacement noise spectral density of the MEMS microphone package.

$$d_{tm} = \sqrt{d_{rel,port}^2 + d_{rel,am}^2 + d_{rel,vent}^2} \tag{A.14}$$

The relative displacement between the diaphragm and grating is the actual displacement detected by the optoelectronics, not the absolute diaphragm motion. Thus, the thermal-mechanical displacement can be improved further if the backplate is stiffer. Finally, the optoelectronics and TIA noise spectral densities (MDD and $d_{tm,TIA}$) can be added to d_{tm} to evaluate the overall noise spectral density of the entire optical microphone.

$$d_{tm,total} = \sqrt{d_{tm}^2 + \mathrm{MDD}^2 + d_{tm,TIA}^2} \tag{A.15}$$

where, $d_{tm,TIA}$ is the equivalent thermal-mechanical displacement due to the TIA noise which is computed by $V_{no,total}/S_{PD}$. The total input-pressure-referred noise P_{tm} may be computed by,

$$P_{tm} = \frac{d_{tm,total}}{C_{mp}} \tag{A.16}$$

where, C_{mp} is the system compliance which is the sum of the diaphragm and backplate compliances in units of m/Pa. Frequency response due to the input pressure P_{in} or electrostatic actuation P_{es} from Figure A.1 can be also simulated using a similar procedure. The set of linear equations is shown in (A.17).

$$\begin{bmatrix} Z_{aport} + \frac{1}{j\omega C_{afc}} & 0 & 0 & -\frac{1}{j\omega C_{afc}} \\ 0 & Z_{abp} + R_{am} & -Z_{abp} & 0 \\ 0 & -Z_{abp} & Z_{ad} + Z_{abp} + R_{avent} & -R_{avent} \\ -\frac{1}{j\omega C_{afc}} & 0 & -R_{avent} & \frac{1}{j\omega C_{afc}} + R_{avent} + \frac{1}{j\omega C_{abc}} \end{bmatrix} \begin{bmatrix} Q_{in} \\ Q_{rel} \\ Q_d \\ Q_{bc} \end{bmatrix} = \begin{bmatrix} P_{in} \\ P_{es} \\ -P_{es} \\ 0 \end{bmatrix} \tag{A.17}$$

Appendix B

Design of Experiments

The Design of Experiment tables are presented in the next two pages.

DOE #	f_{cut} [Hz]	C_{mp} [m/Pa]	$C_{mp,int}$ [m/Pa]	MDD [m/√Hz]	V_{MEMS} [m³]	V_{ASIC} [m³]	V_{LID} [m³]	V_{fc} [m³]	V_{bc} [m³]	R_{aport} [Pa·s/m³]	M_{aport} [kg/m⁴]	R_{avent} [Pa·s/m³]	C_{afc} [m³/Pa]	C_{abc} [m³/Pa]	Vent noise [dBA]	Port noise [dBA]	Optics noise [dBA]	Spoke noise [dBA]	Grating noise [dBA]	Total noise [dBA]	SNR [dB]	AOP [dB SPL]
1	5	6.00E-08	5.45E-08	2.71E-15	4.32E-10	5.00E-11	3.20E-08	2.26E-10	3.15E-08	4.70E+05	7.12E+02	1.40E+11	1.63E-15	2.27E-13	-3.88	2.64	-11.11	17.92	20.62	22.54	71.46	95.99
2	5	4.00E-08	3.75E-08	2.71E-15	4.32E-10	5.00E-11	3.20E-08	2.26E-10	3.15E-08	4.70E+05	7.12E+02	1.40E+11	1.63E-15	2.27E-13	-4.32	-3.57	-7.86	11.81	14.50	16.47	77.53	99.24
3	5	2.00E-08	1.94E-08	2.71E-15	4.32E-10	5.00E-11	3.20E-08	2.26E-10	3.15E-08	4.70E+05	7.12E+02	1.40E+11	1.63E-15	2.27E-13	-4.39	-5.37	-2.13	10.06	12.75	14.81	79.19	104.99
4	5	1.00E-08	9.84E-09	2.71E-15	4.32E-10	5.00E-11	3.20E-08	2.26E-10	3.15E-08	4.70E+05	7.12E+02	1.40E+11	1.63E-15	2.27E-13	-4.40	-5.81	3.75	9.62	12.32	14.66	79.34	110.86
5	5	5.00E-09	4.96E-09	2.71E-15	4.32E-10	5.00E-11	3.20E-08	2.26E-10	3.15E-08	4.70E+05	7.12E+02	1.40E+11	1.63E-15	2.27E-13	-4.41	-5.99	9.69	9.44	12.14	15.45	78.55	116.81
6	5	2.50E-09	2.49E-09	2.71E-15	4.32E-10	5.00E-11	3.20E-08	2.26E-10	3.15E-08	4.70E+05	7.12E+02	1.40E+11	1.63E-15	2.27E-13	-4.42	-6.08	15.68	9.36	12.06	17.94	76.06	122.80
7	5	1.00E-09	9.98E-10	2.71E-15	4.32E-10	5.00E-11	3.20E-08	2.26E-10	3.15E-08	4.70E+05	7.12E+02	1.40E+11	1.63E-15	2.27E-13	-4.42	-6.12	23.61	9.31	12.01	24.06	69.94	130.73
8	10	1.00E-08	9.84E-09	2.71E-15	4.32E-10	5.00E-11	3.20E-08	2.26E-10	3.15E-08	4.70E+05	7.12E+02	7.00E+10	1.63E-15	2.27E-13	-1.40	-5.81	3.75	9.62	12.32	14.71	79.29	110.86
9	20	1.00E-08	9.83E-09	2.71E-15	4.32E-10	5.00E-11	3.20E-08	2.26E-10	3.15E-08	4.70E+05	7.12E+02	3.50E+10	1.63E-15	2.27E-13	1.60	-5.81	3.75	9.62	12.32	14.82	79.18	110.87
10	40	1.00E-08	9.83E-09	2.71E-15	4.32E-10	5.00E-11	3.20E-08	2.26E-10	3.15E-08	4.70E+05	7.12E+02	1.75E+10	1.63E-15	2.27E-13	4.57	-5.81	3.75	9.62	12.32	15.01	78.99	110.87
11	60	1.00E-08	9.82E-09	2.71E-15	4.32E-10	5.00E-11	3.20E-08	2.26E-10	3.15E-08	4.70E+05	7.12E+02	1.17E+10	1.63E-15	2.27E-13	6.27	-5.81	3.75	9.62	12.32	15.20	78.80	110.88
12	80	1.00E-08	9.81E-09	2.71E-15	4.32E-10	5.00E-11	3.20E-08	2.26E-10	3.15E-08	4.70E+05	7.12E+02	8.76E+09	1.63E-15	2.27E-13	7.44	-5.81	3.75	9.63	12.32	15.37	78.63	110.89
13	100	1.00E-08	9.79E-09	2.71E-15	4.32E-10	5.00E-11	3.20E-08	2.26E-10	3.15E-08	4.70E+05	7.12E+02	7.00E+09	1.63E-15	2.27E-13	8.33	-5.82	3.75	9.63	12.32	15.52	78.48	110.91
14	5	1.00E-08	9.84E-09	2.71E-15	4.32E-10	5.00E-11	3.20E-08	2.26E-10	3.15E-08	2.35E+05	6.11E+02	1.40E+11	1.63E-15	2.27E-13	-4.38	-8.83	3.75	9.61	12.31	14.63	79.37	110.86
15	5	1.00E-08	9.84E-09	2.71E-15	4.32E-10	5.00E-11	3.20E-08	2.26E-10	3.15E-08	7.05E+05	8.12E+02	1.40E+11	1.63E-15	2.27E-13	-4.42	-4.03	3.75	9.64	12.33	14.69	79.31	110.86
16	5	1.00E-08	9.84E-09	2.71E-15	4.32E-10	5.00E-11	3.20E-08	2.26E-10	3.15E-08	1.17E+06	1.01E+03	1.40E+11	1.63E-15	2.27E-13	-4.45	-1.78	3.75	9.66	12.35	14.75	79.25	110.86
17	5	1.00E-08	9.84E-09	2.71E-15	4.32E-10	5.00E-11	3.20E-08	2.26E-10	3.15E-08	1.64E+06	1.21E+03	1.40E+11	1.63E-15	2.27E-13	-4.47	-0.29	3.75	9.68	12.38	14.81	79.19	110.86
18	5	1.00E-08	9.84E-09	2.71E-15	4.32E-10	5.00E-11	3.20E-08	2.26E-10	3.15E-08	2.11E+06	1.41E+03	1.40E+11	1.63E-15	2.27E-13	-4.47	0.84	3.75	9.71	12.40	14.87	79.13	110.86
19	5	1.00E-08	9.84E-09	2.71E-15	4.32E-10	5.00E-11	3.20E-08	2.26E-10	3.15E-08	2.58E+06	1.61E+03	1.40E+11	1.63E-15	2.27E-13	-4.46	1.74	3.75	9.73	12.42	14.93	79.07	110.86
20	5	1.00E-08	9.85E-09	2.71E-15	4.32E-10	5.00E-11	3.20E-08	2.26E-10	3.15E-08	1.17E+07	5.52E+03	1.40E+11	1.63E-15	2.27E-13	-0.89	9.24	3.75	10.38	13.08	16.32	77.68	110.86
21	5	1.00E-08	9.86E-09	2.71E-15	4.32E-10	5.00E-11	3.20E-08	2.26E-10	3.15E-08	2.35E+07	1.05E+04	1.40E+11	1.63E-15	2.27E-13	17.07	20.84	3.75	17.09	19.79	25.07	68.93	110.85
22	5	1.00E-08	9.67E-09	2.71E-15	4.32E-10	5.00E-11	1.60E-08	2.26E-10	1.55E-08	4.70E+05	7.12E+02	2.85E+11	1.63E-15	1.12E-13	-1.23	-5.81	3.90	9.62	12.31	14.72	79.28	111.01
23	5	1.00E-08	9.33E-09	2.71E-15	4.32E-10	5.00E-11	8.00E-09	2.26E-10	7.52E-09	4.70E+05	7.12E+02	5.87E+11	1.63E-15	5.42E-14	1.98	-5.83	4.21	9.61	12.30	14.86	79.14	111.32
24	5	1.00E-08	8.66E-09	2.71E-15	4.32E-10	5.00E-11	4.00E-09	2.26E-10	3.52E-09	4.70E+05	7.12E+02	1.26E+12	1.63E-15	2.54E-14	5.31	-5.85	4.85	9.59	12.29	15.15	78.85	111.97
25	5	1.00E-08	7.36E-09	2.71E-15	4.32E-10	5.00E-11	2.00E-09	2.26E-10	1.52E-09	4.70E+05	7.12E+02	2.91E+12	1.63E-15	1.09E-14	8.97	-5.90	6.26	9.56	12.25	15.82	78.18	113.38
26	5	1.00E-08	6.73E-09	2.71E-15	4.32E-10	5.00E-11	1.60E-09	2.26E-10	1.12E-09	4.70E+05	7.12E+02	3.95E+12	1.63E-15	8.06E-15	10.30	-5.93	7.05	9.55	12.24	16.21	77.79	114.16
27	5	1.00E-08	4.88E-09	2.71E-15	4.32E-10	5.00E-11	1.00E-09	2.26E-10	5.18E-10	4.70E+05	7.12E+02	8.52E+12	1.63E-15	3.73E-15	13.64	-5.99	9.84	9.53	12.22	17.69	76.31	116.96
28	5	1.00E-08	4.28E-09	2.71E-15	4.32E-10	5.00E-11	8.89E-10	2.26E-10	4.07E-10	4.70E+05	7.12E+02	1.09E+13	1.63E-15	2.93E-15	14.69	-6.01	10.98	9.53	12.23	18.32	75.68	118.10
29	5	1.00E-08	3.69E-09	2.71E-15	4.32E-10	5.00E-11	8.00E-10	2.26E-10	3.18E-10	4.70E+05	7.12E+02	1.39E+13	1.63E-15	2.29E-15	15.76	-6.03	12.27	9.54	12.24	19.06	74.94	119.39

DOE #	f_{cut} [Hz]	C_{mp} [m/Pa]	$C_{mp,int}$ [m/Pa]	MDD [m/√Hz]	V_{MEMS} [m³]	V_{ASIC} [m³]	V_{LID} [m³]	V_{fc} [m³]	V_{bc} [m³]	R_{aport} [Pa·s/m³]	M_{aport} [kg/m⁴]	R_{avent} [Pa·s/m³]	C_{afc} [m³/Pa]	C_{abc} [m³/Pa]	Vent noise [dBA]	Port noise [dBA]	Optics noise [dBA]	Spoke noise [dBA]	Grating noise [dBA]	Total noise [dBA]	SNR [dB]	AOP [dB SPL]
30	5	1.00E-08	9.84E-09	4.94E-15	4.32E-10	5.00E-11	3.20E-08	2.26E-10	3.15E-08	4.70E+05	7.12E+02	1.40E+11	1.63E-15	2.27E-13	-4.40	-5.81	8.98	9.62	12.32	15.41	78.59	110.86
31	5	1.00E-08	9.84E-09	8.56E-15	4.32E-10	5.00E-11	3.20E-08	2.26E-10	3.15E-08	4.70E+05	7.12E+02	1.40E+11	1.63E-15	2.27E-13	-4.40	-5.81	13.75	9.62	12.32	17.04	76.96	110.86
32	5	1.00E-08	9.84E-09	2.71E-14	4.32E-10	5.00E-11	3.20E-08	2.26E-10	3.15E-08	4.70E+05	7.12E+02	1.40E+11	1.63E-15	2.27E-13	-4.40	-5.81	23.75	9.62	12.32	24.21	69.79	110.86
33	5	6.00E-08	5.45E-08	8.56E-15	4.32E-10	5.00E-11	3.20E-08	2.26E-10	3.15E-08	4.70E+05	7.12E+02	1.40E+11	1.63E-15	2.27E-13	-3.88	2.64	-1.11	17.92	20.62	22.56	71.44	95.99
34	5	2.00E-08	1.94E-08	8.56E-15	4.32E-10	5.00E-11	3.20E-08	2.26E-10	3.15E-08	4.70E+05	7.12E+02	1.40E+11	1.63E-15	2.27E-13	-4.39	-5.37	7.87	10.06	12.75	15.53	78.47	104.99
35	5	5.00E-09	4.96E-09	8.56E-15	4.32E-10	5.00E-11	3.20E-08	2.26E-10	3.15E-08	4.70E+05	7.12E+02	1.40E+11	1.63E-15	2.27E-13	-4.41	-5.99	19.69	9.44	12.14	20.75	73.25	116.81
36	5	2.50E-09	2.49E-09	8.56E-15	4.32E-10	5.00E-11	3.20E-08	2.26E-10	3.15E-08	4.70E+05	7.12E+02	1.40E+11	1.63E-15	2.27E-13	-4.42	-6.08	25.68	9.36	12.06	25.96	68.04	122.80
37	5	1.00E-09	9.98E-10	8.56E-15	4.32E-10	5.00E-11	3.20E-08	2.26E-10	3.15E-08	4.70E+05	7.12E+02	1.40E+11	1.63E-15	2.27E-13	-4.42	-6.12	33.61	9.31	12.01	33.66	60.34	130.73
38	5	1.00E-08	9.67E-09	8.56E-15	4.32E-10	5.00E-11	1.60E-08	2.26E-10	1.55E-08	4.70E+05	7.12E+02	2.85E+11	1.63E-15	1.12E-13	-1.23	-5.81	13.90	9.62	12.31	17.14	76.86	111.01
39	5	1.00E-08	9.33E-09	8.56E-15	4.32E-10	5.00E-11	8.00E-09	2.26E-10	7.52E-09	4.70E+05	7.12E+02	5.87E+11	1.63E-15	5.42E-14	1.98	-5.83	14.21	9.61	12.30	17.35	76.65	111.32
40	5	1.00E-08	8.66E-09	8.56E-15	4.32E-10	5.00E-11	4.00E-09	2.26E-10	3.52E-09	4.70E+05	7.12E+02	1.26E+12	1.63E-15	2.54E-14	5.31	-5.85	14.85	9.59	12.29	17.80	76.20	111.97
41	5	1.00E-08	7.36E-09	8.56E-15	4.32E-10	5.00E-11	2.00E-09	2.26E-10	1.52E-09	4.70E+05	7.12E+02	2.91E+12	1.63E-15	1.09E-14	8.97	-5.90	16.26	9.56	12.25	18.82	75.18	113.38
42	5	1.00E-08	4.88E-09	8.56E-15	4.32E-10	5.00E-11	1.00E-09	2.26E-10	5.18E-10	4.70E+05	7.12E+02	8.52E+12	1.63E-15	3.73E-15	13.64	-5.99	19.84	9.53	12.22	21.63	72.37	116.96
43	5	1.00E-08	4.28E-09	8.56E-15	4.32E-10	5.00E-11	8.89E-10	2.26E-10	4.07E-10	4.70E+05	7.12E+02	1.09E+13	1.63E-15	2.93E-15	14.69	-6.01	20.98	9.53	12.23	22.57	71.43	118.10
44	5	1.00E-08	3.69E-09	8.56E-15	4.32E-10	5.00E-11	8.00E-10	2.26E-10	3.18E-10	4.70E+05	7.12E+02	1.39E+13	1.63E-15	2.29E-15	15.76	-6.03	22.27	9.54	12.24	23.66	70.34	119.39
45	10	1.00E-08	7.36E-09	2.71E-15	4.32E-10	5.00E-11	2.00E-09	2.26E-10	1.52E-09	4.70E+05	7.12E+02	1.45E+12	1.63E-15	1.09E-14	11.98	-5.90	6.26	9.56	12.25	16.64	77.36	113.38
46	20	1.00E-08	7.36E-09	2.71E-15	4.32E-10	5.00E-11	2.00E-09	2.26E-10	1.52E-09	4.70E+05	7.12E+02	7.27E+11	1.63E-15	1.09E-14	14.98	-5.90	6.26	9.56	12.25	17.91	76.09	113.38
47	40	1.00E-08	7.36E-09	2.71E-15	4.32E-10	5.00E-11	2.00E-09	2.26E-10	1.52E-09	4.70E+05	7.12E+02	3.64E+11	1.63E-15	1.09E-14	17.97	-5.90	6.26	9.56	12.25	19.68	74.32	113.38
48	60	1.00E-08	7.36E-09	2.71E-15	4.32E-10	5.00E-11	2.00E-09	2.26E-10	1.52E-09	4.70E+05	7.12E+02	2.42E+11	1.63E-15	1.09E-14	19.69	-5.90	6.26	9.56	12.26	20.92	73.08	113.39
49	80	1.00E-08	7.35E-09	2.71E-15	4.32E-10	5.00E-11	2.00E-09	2.26E-10	1.52E-09	4.70E+05	7.12E+02	1.82E+11	1.63E-15	1.09E-14	20.90	-5.91	6.26	9.56	12.26	21.85	72.15	113.39
50	100	1.00E-08	7.34E-09	2.71E-15	4.32E-10	5.00E-11	2.00E-09	2.26E-10	1.52E-09	4.70E+05	7.12E+02	1.45E+11	1.63E-15	1.09E-14	21.81	-5.91	6.26	9.56	12.26	22.61	71.39	113.40
51	5	1.00E-08	9.84E-09	2.71E-15	4.32E-10	5.00E-11	3.20E-08	2.26E-10	3.15E-08	2.32E+06	4.72E+03	1.40E+11	1.63E-15	2.27E-13	-2.10	1.95	3.75	10.21	12.90	15.39	78.61	110.86
52	5	1.00E-08	9.85E-09	2.71E-15	4.32E-10	5.00E-11	3.20E-08	2.26E-10	3.15E-08	3.63E+06	5.68E+03	1.40E+11	1.63E-15	2.27E-13	-0.62	4.19	3.75	10.42	13.12	15.73	78.27	110.85
53	5	1.00E-08	9.85E-09	2.71E-15	4.32E-10	5.00E-11	3.20E-08	2.26E-10	3.15E-08	6.32E+06	7.12E+03	1.40E+11	1.63E-15	2.27E-13	2.14	7.24	3.75	10.87	13.56	16.46	77.54	110.85
54	5	1.00E-08	9.85E-09	2.71E-15	4.32E-10	5.00E-11	3.20E-08	2.26E-10	3.15E-08	1.26E+07	9.42E+03	1.40E+11	1.63E-15	2.27E-13	9.83	13.24	3.75	13.06	15.75	19.58	74.42	110.85
55	5	1.00E-08	9.86E-09	2.71E-15	4.32E-10	5.00E-11	3.20E-08	2.26E-10	3.15E-08	3.01E+07	1.35E+04	1.40E+11	1.63E-15	2.27E-13	19.47	22.89	3.75	17.87	20.57	26.63	67.37	110.84

Bibliography

[1] P. R. Scheeper, W. Olthuis, and P. Bergveld, "A silicon condenser microphone with a silicon nitride diaphragm and backplate," *Journal of Micromechanics and Microengineering*, vol. 2, no. 3, p. 187, 1992. [Online]. Available: http://stacks.iop.org/0960-1317/2/i=3/a=016

[2] J. Bergqvist, F. Rudolf, J. Maisano, F. Parodi, and M. Ross, "A silicon condenser microphone with a highly perforated backplate," in *1991 International Conference on Solid-State Sensors and Actuators, 1991. Digest of Technical Papers, TRANSDUCERS '91.*, June 1991, pp. 266–269.

[3] A. Torkkeli, O. Rusanen, J. Saarilahti, H. Sepp, H. Sipola, and J. Hietanen, "Capacitive microphone with low-stress polysilicon membrane and high-stress polysilicon backplate," *Sensors and Actuators A: Physical*, vol. 85, no. 1, pp. 116 – 123, 2000. [Online]. Available: http://www.sciencedirect.com/science/article/pii/S0924424700003368

[4] J. W. Weigold, T. J. Brosnihan, J. Bergeron, and X. Zhang, "A MEMS condenser microphone for consumer applications," in *19th IEEE International Conference on Micro Electro Mechanical Systems*, 2006, pp. 86–89.

[5] T. Kasai, Y. Tsurukame, T. Takahashi, F. Sato, and S. Horiike, "Small silicon condenser microphone improved with a backchamber with concave

lateral sides," in *TRANSDUCERS 2007 - 2007 International Solid-State Sensors, Actuators and Microsystems Conference*, June 2007, pp. 2613–2616.

[6] A. Dehé, M. Wurzer, M. Füldner, and U. Krumbein, "Design of a poly silicon MEMS microphone for high signal-to-noise ratio," in *2013 Proceedings of the European Solid-State Device Research Conference (ESSDERC)*, Sept 2013, pp. 292–295.

[7] P. V. Loeppert and S. B. Lee, "Sisonictm–the first commercialized mems microphone," in *Proceedings of the Solid-State Sensors, Actuators, and Microsystems Workshop*, 2006, pp. 27–30.

[8] A. Dehé, M. Wurzer, M. Füldner, and U. Krumbein, "The infineon silicon MEMS microphone," 2013.

[9] M. Bao and H. Yang, "Squeeze film air damping in mems," *Sensors and Actuators A: Physical*, vol. 136, no. 1, pp. 3 – 27, 2007, 25th Anniversary of Sensors and Actuators A: Physical.

[10] N. A. Hall, M. Okandan, R. Littrell, B. Bicen, and F. L. Degertekin, "Simulation of thin-film damping and thermal mechanical noise spectra for advanced micromachined microphone structures," *Journal of Microelectromechanical Systems*, vol. 17, no. 3, pp. 688–697, June 2008.

[11] 2013. [Online]. Available: http://www.analog.com/static/imported-files/data_sheets/ADMP801.pdf

[12] M. L. Kuntzman, C. T. Garcia, A. G. Onaran, B. Avenson, K. D. Kirk, and N. A. Hall, "Performance and modeling of a fully packaged micromachined optical microphone," *Journal of Microelectromechanical Systems*, vol. 20, no. 4, pp. 828–833, Aug 2011.

[13] T. B. Gabrielson, "Mechanical-thermal noise in micromachined acoustic and vibration sensors," *IEEE Transactions on Electron Devices*, vol. 40, no. 5, pp. 903–909, May 1993.

[14] T. B. Gabrielson, "Fundamental noise limits for miniature acoustic and vibration sensors," *Journal of Vibration and Acoustics*, vol. 117, no. 4, pp. 405–410, 1995.

[15] M. Füldner and A. Dehé, "Challenges of high SNR (signal-to-noise) silicon micro machined microphones," in *Proceedings of 19th International Congress on Acoustics, Madrid, Spain*, 2007, pp. 1–6.

[16] S. C. Thompson, J. L. LoPresti, E. M. Ring, H. G. Nepomuceno, J. J. Beard, W. J. Ballad, and E. V. Carlson, "Noise in miniature microphones," *The Journal of the Acoustical Society of America*, vol. 111, no. 2, pp. 861–866, 2002.

[17] P. C. Hobbs, "Reaching the shot noise limit for $10," *Optics and Photonics News*, vol. 2, no. 4, pp. 17–23, 1991.

[18] R. Littrell, N. A. Hall, M. Okandan, R. Olsson, and D. Serkland, "Impact of relative intensity noise of vertical-cavity surface-emitting lasers on

optics-based micromachined audio and seismic sensors," *Applied Optics*, vol. 46, no. 28, pp. 6907–6911, Oct 2007.

[19] G. W. Elko, F. Pardo, D. Lpez, D. Bishop, and P. Gammel, "Capacitive mems microphones," *Bell Labs Technical Journal*, vol. 10, no. 3, pp. 187–198, Fall 2005.

[20] H. Schröder, E. Obermeier, and A. Steckenborn, "Effects of the etchmask properties on the anisotropy ratio in anisotropic etching of {100} silicon in aqueous KOH," *Journal of Micromechanics and Microengineering*, vol. 8, no. 2, p. 99, 1998. [Online]. Available: http://stacks.iop.org/0960-1317/8/i=2/a=014

[21] E. D. Palik, O. J. Glembocki, I. H. Jr., P. S. Burno, and L. Tenerz, "Etching roughness for (100) silicon surfaces in aqueous KOH," *Journal of Applied Physics*, vol. 70, no. 6, pp. 3291–3300, 1991. [Online]. Available: https://doi.org/10.1063/1.349263

[22] A. Tarraf, J. Daleiden, S. Irmer, D. Prasai, and H. Hillmer, "Stress investigation of PECVD dielectric layers for advanced optical MEMS," *Journal of Micromechanics and Microengineering*, vol. 14, no. 3, p. 317, 2004. [Online]. Available: http://stacks.iop.org/0960-1317/14/i=3/a=001

[23] M. P. Hughey and R. F. Cook, "Massive stress changes in plasma-enhanced chemical vapor deposited silicon nitride films on thermal

cycling," *Thin Solid Films*, vol. 460, no. 1, pp. 7 – 16, 2004. [Online]. Available: http://www.sciencedirect.com/science/article/pii/S0040609004000689

[24] M. P. Hughey and R. F. Cook, "Stress development kinetics in plasma-enhanced chemical-vapor-deposited silicon nitride films," *Journal of Applied Physics*, vol. 97, no. 11, p. 114914, 2005. [Online]. Available: https://doi.org/10.1063/1.1927708

[25] W. Lee, N. A. Hall, Z. Zhou, and F. L. Degertekin, "Fabrication and characterization of a micromachined acoustic sensor with integrated optical readout," *IEEE Journal of Selected Topics in Quantum Electronics*, vol. 10, no. 3, pp. 643–651, May 2004.

[26] N. Hall and F. L. Degertekin, "An integrated optical detection method for capacitive micromachined ultrasonic transducers," in *2000 IEEE Ultrasonics Symposium. Proceedings. An International Symposium (Cat. No.00CH37121)*, vol. 1, Oct 2000, pp. 951–954 vol.1.

[27] S. Trolier-McKinstry and P. Muralt, "Thin film piezoelectrics for MEMS," *Journal of Electroceramics*, vol. 12, no. 1, pp. 7–17, Jan 2004. [Online]. Available: https://doi.org/10.1023/B:JECR.0000033998.72845.51

[28] D. Kim, N. N. Hewa-Kasakarage, M. L. Kuntzman, K. D. Kirk, S. H. Yoon, and N. A. Hall, "Piezoelectric micromachined microphones with out-of-plane directivity," *Applied Physics Letters*, vol. 103, no. 1, p. 013502, 2013. [Online]. Available: https://doi.org/10.1063/1.4812298

[29] D. Kim, N. N. Hewa-Kasakarage, M. L. Kuntzman, and N. A. Hall, "Experimental comparison of 3-3 and 3-1 mode piezoelectric microelectromechanical systems," *The Journal of the Acoustical Society of America*, vol. 134, no. 5, pp. 4123–4123, 2013. [Online]. Available: https://doi.org/10.1121/1.4831147

[30] M. D. Williams, B. A. Griffin, T. N. Reagan, J. R. Underbrink, and M. Sheplak, "An AlN MEMS piezoelectric microphone for aeroacoustic applications," *Journal of Microelectromechanical Systems*, vol. 21, no. 2, pp. 270–283, April 2012.

[31] P. Muralt, "PZT thin films for microsensors and actuators: Where do we stand?" *IEEE Transactions on Ultrasonics, Ferroelectrics, and Frequency Control*, vol. 47, no. 4, pp. 903–915, July 2000.

[32] P. Muralt, "Ferroelectric thin films for micro-sensors and actuators: a review," *Journal of Micromechanics and Microengineering*, vol. 10, no. 2, p. 136, 2000. [Online]. Available: http://stacks.iop.org/0960-1317/10/i=2/a=307

[33] C. G. Keller and R. T. Howe, "Hexsil bimorphs for vertical actuation," in *The 8th International Conference on Solid-State Sensors and Actuators, 1995 and Eurosensors IX.. Transducers '95.*, vol. 1, Jun 1995, pp. 99–102.

[34] C. G. Keller and R. T. Howe, "Hexsil tweezers for teleoperated micro-assembly," in *Proceedings IEEE The Tenth Annual International Work-*

shop on Micro Electro Mechanical Systems. An Investigation of Micro Structures, Sensors, Actuators, Machines and Robots, Jan 1997, pp. 72–77.

[35] F. Duval, R. Dorey, R. Haigh, and R. Whatmore, "Stable TiO_2/Pt electrode structure for lead containing ferroelectric thick films on silicon MEMS structures," *Thin Solid Films*, vol. 444, no. 1, pp. 235 – 240, 2003. [Online]. Available: http://www.sciencedirect.com/science/article/pii/S0040609003011295

[36] S. Corkovic, Q. Zhang, and R. W. Whatmore, "The investigation of key processing parameters in fabrication of $Pb(Zr_xTi_{1-x})O_3$ thick films for MEMS applications," *Journal of Electroceramics*, vol. 19, no. 4, pp. 295–301, Dec 2007. [Online]. Available: https://doi.org/10.1007/s10832-007-9038-1

[37] D. Kim, N. N. Hewa-Kasakarage, S. H. Yoon, K. D. Kirk, M. Kuntzman, and N. A. Hall, "Electrical admittance spectroscopy for piezoelectric MEMS," *Journal of Microelectromechanical Systems*, vol. 22, no. 2, pp. 295–302, April 2013.

[38] L. Lian and N. R. Sottos, "Effects of thickness on the piezoelectric and dielectric properties of lead zirconate titanate thin films," *Journal of Applied Physics*, vol. 87, no. 8, pp. 3941–3949, 2000. [Online]. Available: https://doi.org/10.1063/1.372439

[39] W. J. Choi, Y. Jeon, J.-H. Jeong, R. Sood, and S. G. Kim, "Energy harvesting mems device based on thin film piezoelectric cantilevers," *Journal of Electroceramics*, vol. 17, no. 2, pp. 543–548, Dec 2006. [Online]. Available: https://doi.org/10.1007/s10832-006-6287-3

[40] N. A. Hall, M. Okandan, R. Littrell, B. Bicen, and F. L. Degertekin, "Micromachined optical microphone structures with low thermal-mechanical noise levels," *The Journal of the Acoustical Society of America*, vol. 122, no. 4, pp. 2031–2037, 2007.

Vita

Donghwan Kim was born in Seoul, South Korea on September 11, 1981, the son of Bangsi Kim and Sookhee Kim. At the age of 25, he came to the United States and received a degree of Bachelor of Science in Mechanical Engineering with an Aerospace Engineering Minor from Illinois Institute of Technology in 2008. He also received the degree of Bachelor of Science in Mechanical Engineering from INHA University, South Korea in 2008. In August of the same year, he entered the Graduate School at The University of Texas at Austin and earned a degree of Master of Science in Engineering in 2010. Since August 2011, he has been pursuing the Mechanical Engineering Doctor of Philosophy Program at The University of Texas at Austin.

Permanent address: donghwan.kim@utexas.edu

This dissertation was typeset with LaTeX[†] by the author.

[†] LaTeX is a document preparation system developed by Leslie Lamport as a special version of Donald Knuth's TeX Program.